Multiple Interaction Models of Photoproduction at HERA

High Energy Group

Department of Physics and Astronomy

Mark J. Burton

January 1996

Contents

List of Figures

List of Tables

Abstract

The energy flow of hard photoproduction events exhibiting jets has been studied using data collected by H1 during the 1993 run period. Increased energy flow is seen in the proton direction centred about $\eta \sim 2$, compared to predictions made using the PYTHIA SI generator incorporating only initial and final state radiation. Predictions from the PHOJET and PYTHIA MI generators, which both include beam remnant interactions, are found to describe the data much more satisfactorily, providing strong evidence in favour of the multiple interaction scenario. For the first time H1's forward tracking detector has been used to measure the charged particle energy flow in the forward direction, providing a vital cross check for calorimetric measurements. Energy flow measurements are found to be in agreement with those of the calorimeter.

Declaration

No portion of the work referred to in this thesis has been submitted in support of an application for another degree or qualification of this or any other university or other institute of learning.

1. Copyright in text of this thesis rests with the Author. Copies (by any process) either in full, or of extracts, may be made only in accordance with instructions given by the Author and lodged in the John Rylands University Library of Manchester. Details may be obtained from the Librarian. This page must form part of any such copies made. Further copies (by any process) of copies made in accordance with such instructions may not be made without the permission (in writing) of the Author.

2. The ownership of any intellectual property rights which may be described in this thesis is vested in the University of Manchester, subject to any prior agreement to the contrary, and may not be made available for use by third parties without the written permission of the University, which will prescribe the terms and conditions of any such agreement.

Further information on the conditions under which disclosures and exploitation may take place is available from the Head of Department of Physics and Astronomy.

The author was educated at Gillott's School, Henley-on-Thames $(1982-1987)$ and The Henley College $(1987-1989)$. He obtained a 1st class BSc (Hons) degree in Computer Science and Physics from the University of Manchester in 1992. The work presented in this thesis was conducted at the Deutsches Elektronen-Synchrotron (DESY), Hamburg and the University of Manchester $(1992-1995)$.

Chapter 1

Introduction

The electron-proton collider HERA provides unique conditions under which to study the photon. Almost real photons are produced by electrons scattered through small angles, making HERA an effective photon-proton collider with luminosity approximately one tenth that of the electron-proton luminosity, and centre of mass energies up to 300 GeV. This is an order of magnitude greater than have previously been achieved in other experiments and opens up a new kinematic domain in which to study the photon, providing a new arena in which to test QCD predictions.

It has been known since the days of low energy fixed target experiments that the photon may interact in a non-trivial way with matter. The first experimental observation of this behaviour originated the Vector Meson Dominance model which describes with great success low energy photoproduction data. At higher energies however, this phenomenological model breaks down and must replaced by a QCD inspired model.

At HERA energies the photon exhibits hard hadronic like interactions (see figure 1.1) with the proton, similar to those previously observed in $p\bar{p}$ colliders. In these types of events, each of the incoming beam particles is a composite object, consisting of many partons. Therefore, the finite probability for a single interaction

necessitates a finite probability for additional interactions, in a way somewhat analogous to the 'pile up' situation experienced by colliding beams. These additional interactions are known as the underlying event, whose effect is to increase the energy flow in the event, particularly in the forward direction.

Without a good understanding of the underlying events it becomes difficult to make precise measurements of cross sections and structure functions. This thesis is primarily concerned with the measurement of the underlying event for hard photoproduction processes and comparison of the predictions of several generator models with data. Energy flow measurements are the subject of chapter 7. In addition to making calorimetric measurements of the energy flow, the H1 Forward Tracking Detector is used for the first time to provide an independent measurement of the charged particle energy flow. A detailed analysis of the performance of the Forward Tracking Detector can be found in chapter 6. Other topics included in this thesis are: an overview of photoproduction at HERA in chapter 2; a description of the H1 detector in chapter 3; details of hard photoproduction event selection in chapter 4 and the reconstruction of parton dynamics from jets in chapter 5.
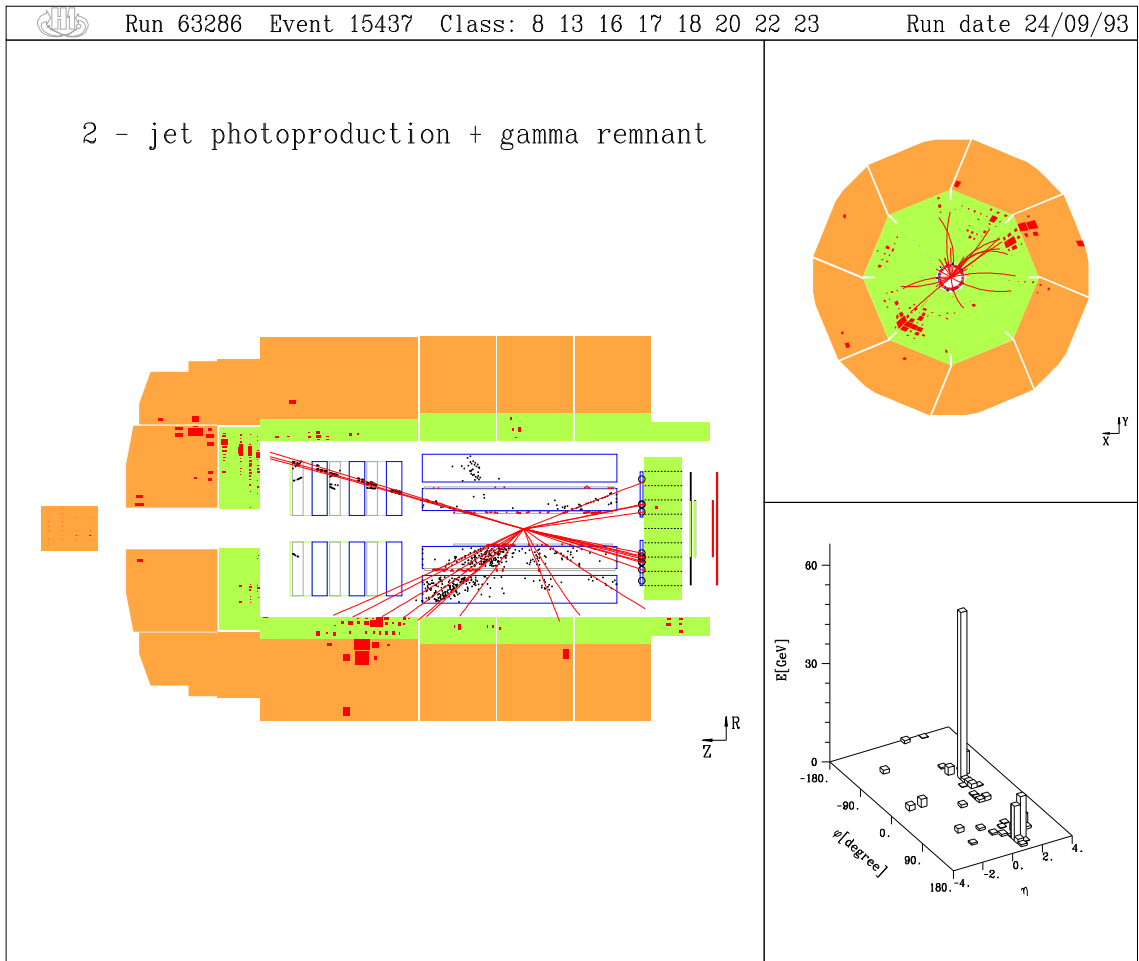
Figure 1.1: A 2-jet resolved photoproduction event demonstrating the 'hadronic' nature of the photon. Note the tracks in the backward direction originating from the photon remnant.

Chapter 2

Photon-proton Scattering at HERA

The photon is the gauge boson of QED, the simplest of all bosons. In QED the photon is a massless point-like particle and predictions for γe interactions can be made with very impressive accuracy (1 part in 10^8). It is then perhaps surprising that many reactions involving quasi-real photons are much less well understood both experimentally and theoretically. This can be attributed to the uncertainty principle which predicts that the photon can fluctuate into pairs of charged particles for short periods of time. Fluctuation into lepton pairs is understood from QED, but fluctuation into quark-antiquark pairs is a much more challenging problem. If the lifetime of the virtual photon exceeds $\sim 10^{-25}$ s (momentum scale $\lesssim 1\,\text{GeV}$) then the $q\bar{q}$ pair has the possibility to evolve into a complicated hadronic state. Even for shorter lived states, QCD radiation processes complicate the situation.

The interactions of the photon may be divided into two categories, soft interactions and hard interactions. The term 'soft' implies that the process lies in the non-perturbative kinematic region and usually a phenomenological model is used to describe these processes. Hard processes on the other hand are modelled
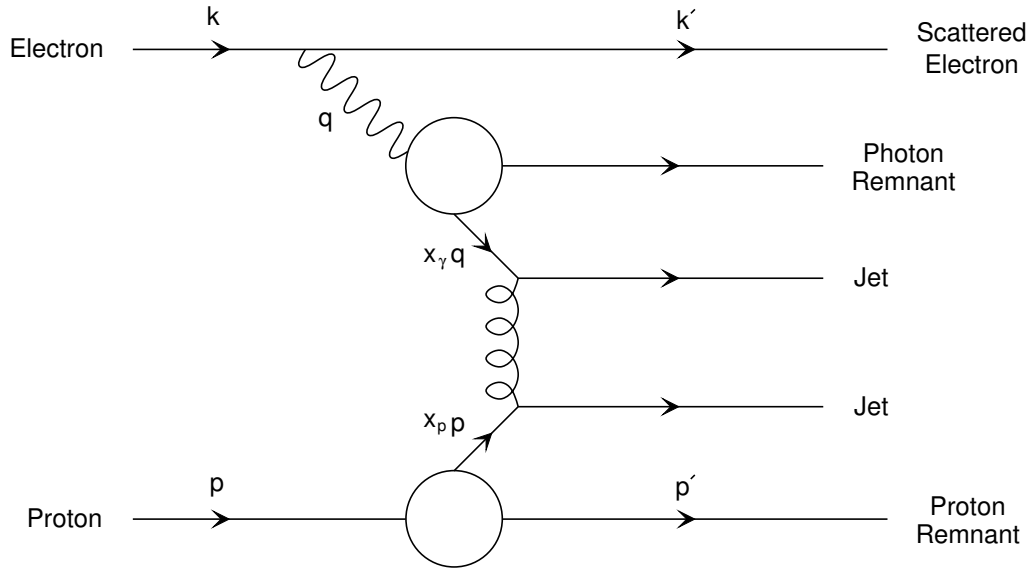
Figure 2.1: The kinematics of a typical resolved photoproduction event.

within the frame work of perturbative QCD. This distinction between hard and soft is somewhat artificial because there is a smooth transition between these two cases.

2.1 Kinematic Framework

A schematic diagram of a typical photoproduction event is shown in figure 2.1. The kinematics of the event are described by the variables y, Q^2 and x_γ. The variable y measures the fraction of the incident electron energy carried by the photon, defined as

$$y = \frac{p \cdot q}{p \cdot k} = 1 - \frac{E'_e}{E_e} \cos^2 \frac{\theta^*_e}{2} \approx 1 - \frac{E'_e}{E_e} \tag{2.1}$$

where $\theta^*_e = \pi - \theta_e \sim 0$ for photoproduction. The negative 4-momentum transfer squared Q^2 is defined as

$$Q^2 = -q^2 \approx 4 E_e E'_e \sin^2 \frac{\theta^*_e}{2} \tag{2.2}$$

and for this photoproduction analysis is limited to $Q^2 < 10^{-2} \, \mathrm{GeV}^2$ by geometric

constraints imposed by the tagging detector. Thus the photons produced are almost real and are called quasi-real.

The interaction of the resolved photon is described in terms of x_γ, the fraction of the photon's momentum carried by its interacting parton. For direct photoproduction events x_γ has a value of 1.0 because the whole photon interacts. At leading order this variable may be calculated from the scattering parton's dynamics as follows

$$x_\gamma = \frac{E_t^{par1} e^{-\eta^{par1}} + E_t^{par2} e^{-\eta^{par2}}}{2E_\gamma} \qquad (2.3)$$

or alternatively

$$x_\gamma = \frac{\left(E_t^{par1} + E_t^{par2}\right) \times \left(e^{-\eta^{par1}} + e^{-\eta^{par2}}\right)}{4E_\gamma} \qquad (2.4)$$

where $E_t^{par\,1,2}$ are the transverse energies of each parton, $\eta^{par\,1,2}$ are the pseudo-rapidities of each parton and E_γ is the photon energy.

Two other useful quantities are $W_{\gamma p}$ the centre of mass energy of the γp system

$$W_{\gamma p} = \sqrt{y}\, W_{ep} \qquad (2.5)$$

where W_{ep} is the ep centre of mass energy. The tagging of the scattered electron limits the available energies to $150 < W_{\gamma p} < 250\,\mathrm{GeV}$, an order of magnitude greater that previously obtained at fixed target experiments. The boost β of the γp centre of mass system relative to the laboratory system is given by

$$\beta = \frac{1}{2}\ln\left(\frac{E_p}{E_\gamma}\right) = \eta^* - \eta \qquad (2.6)$$

where β is measured in pseudo-rapidity[1].

---

[1]Pseudo-rapidity is defined as $\eta = -\ln(\tan(\theta/2))$

2.2 Photoproduction

In ep collisions, the incident electron may be considered as a source of real photons of flux $f_{\gamma/e}$, given by the Weizsäcker-Williams approximation [1, 2]

$$\frac{d^2 f_{\gamma/e}(y, Q^2)}{dy dQ^2} = \frac{\alpha_{em}}{2\pi Q^2} \left(\frac{1 + (1-y)^2}{y} - \frac{2(1-y)}{y} \frac{Q^2_{min}}{Q^2} \right) \tag{2.7}$$

Using the Equivalent Photon approximation [3] the total differential cross section for ep scattering may be expressed as the product of the photon flux and total γp cross section as follows

$$\frac{d^2 \sigma_{ep}(s)}{dy dQ^2} = \frac{\alpha_{em}}{2\pi Q^2} \left(\frac{1 + (1-y)^2}{y} - \frac{2(1-y)}{y} \frac{Q^2_{min}}{Q^2} \right) \sigma^{tot}_{\gamma p}(ys) \tag{2.8}$$

where Q^2 is the negative square of the photon 4-momentum transfer and s is the squared centre of mass energy of the ep interaction. The minimum detected photon virtuality is defined as $Q^2_{min} = (m_e y)^2/(1-y)$, and is governed by detector acceptance. This expression enables the measured photoproduction cross section to be related to the total γp cross section.

At HERA energies, a number of different mechanisms contribute to the total photoproduction cross section (see [4, 5] for a comprehensive review of photoproduction processes and models). Although the photon is a fundamental point-like particle, through its direct coupling to quarks it has the possibility to split into a quark-antiquark pair. The virtuality of this quark-antiquark pair is characterised by the p_t^2 of the q and $\bar{q}$ with respect to the photon direction. At low virtuality this $q\bar{q}$ state may be described by a vector meson wave function, and this is the basis of the Vector Meson Dominance model (VDM) [6, 7, 8]. In this model the non-interacting photon can couple to a hadronic vector meson with the same quantum numbers ($J^{PC} = 1^{--}$, Q=B=S=0), which can then interact strongly.

In the VDM model, it is postulated that the photon's wave function is composed of a superposition of the bare photon $\mid \gamma_b >$ and a hadronic component $\mid h >$

$$\mid \gamma >= \sqrt{Z_3} \mid \gamma_b > + c\sqrt{\alpha_{em}} \mid h > \tag{2.9}$$

where $Z_3 = 1 - c^2 \alpha_{em}$ assures correct normalisation. In this restricted model, the hadronic component consists entirely of ρ°, ω and ϕ mesons, and their coupling to the photon is determined experimentally. The VDM model has been successful in describing low energy photoproduction at fixed target experiments, and remarkable similarity has been found between photoproduction and hadron-hadron interactions, suggesting that interactions of the bare photon account for only a small fraction of the total photoproduction cross section. As the transverse energy of the $q\bar{q}$ pair at the γ vertex is increased, the VDM model starts to break down because it fails to describe highly virtual short lived states. Extensions to the VDM model exist in which heavier vector mesons are included, known as Generalised Vector Dominance (GVD) [9] models. These improved models still do not describe highly virtual states.

In hadron-hadron physics, processes are divided into elastic, single diffractive, double diffractive, and non-diffractive classes and this classification can be naturally extended to the VDM model. The total γp cross section has a substantial contribution from diffractive processes. Since diffractive reactions involve no exchange of quantum numbers, the final state is characterised by large rapidity gaps, with no hadrons. The elastic process $V + p \rightarrow V + p$ is generalised to the VDM elastic process

$$\gamma + p \rightarrow V + p \tag{2.10}$$

and single and double diffractive processes are correspondingly defined as

$$\gamma + p \quad \rightarrow \quad V + X_2 \tag{2.11}$$

$$\gamma + p \quad \rightarrow \quad X_1 + p \tag{2.12}$$

$$\gamma + p \quad \rightarrow \quad X_1 + X_2 \tag{2.13}$$

The remaining events

$$\gamma + p \rightarrow X \tag{2.14}$$

which predominantly involve the exchange of quantum numbers between the photon and proton are known as non-diffractive processes.

The non-diffractive cross section is dominated by peripheral interactions in the non-perturbative QCD regime, typically leading to isotropic low p_t final states which are modelled phenomenologically using a longitudinal phase space model. However, observation of high p_t final states and jets [10] has demonstrated that there is also a hard component to the non-diffractive cross section.

2.3 Hard Interactions

The hard component of the non-diffractive cross section can be divided into two contributions by virtue of the nature of the photon's interaction. The first contribution is known as 'direct photoproduction' because the photon interacts electromagnetically with a quark from the proton. The second is known as 'resolved photoproduction', and occurs when the photon resolves into a hadronic system from which a parton subsequently interacts with a parton from the proton. There is however, an additional component which arises when the photon couples to a highly virtual quark-antiquark pair without forming a bound state. This mechanism is known as the 'anomalous' contribution. The distinction between direct and resolved processes is only valid for leading order processes, because, for higher order processes, both scattering mechanisms can be present in the same event.

Cross sections for direct processes can be calculated from QCD. Direct processes involve the photon interacting directly in the hard scattering process via the exchange of a virtual quark with a quark ($\gamma q \rightarrow qg$), or gluon ($\gamma g \rightarrow q\bar{q}$) from the proton. These processes are respectively known as QCD Compton and Boson Gluon Fusion (see figure 2.2).
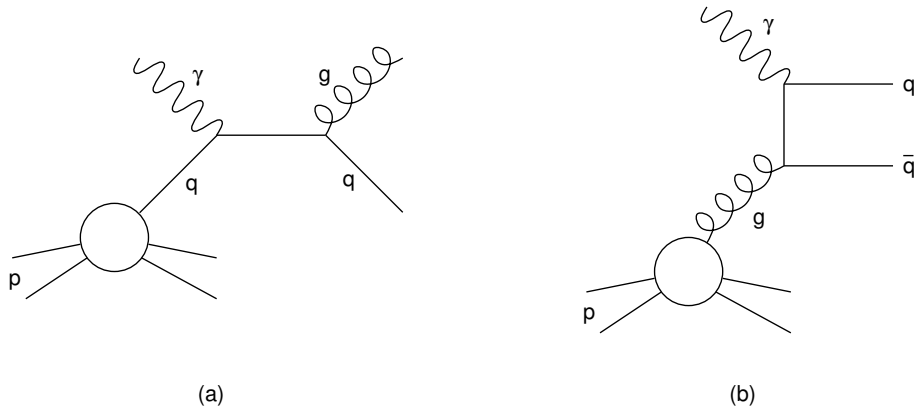
Figure 2.2: Feynman diagrams of direct photoproduction processes. (a) QCD Compton scattering ($\gamma q \to gq$) and (b) Boson Gluon Fusion ($\gamma g \to q\bar{q}$).

The resolved and anomalous components are characterised by the presence of a photon remnant which is composed of the spectator partons to the hard scattering from the resolved photon. Figure 2.3 shows some examples of resolved processes. These processes can be calculated using QCD by assigning a structure function $F^\gamma(x,\,Q^2)$ to the photon to describe the parton distributions present in the resolved photon. A number of such parameterisations exist, but the current experimentally favoured from measurements recently made by H1 [11] is the LO-GRV [12] parameterisation.

At HERA centre of mass energies, resolved processes dominate over direct processes in this hard component of photoproduction, providing an excellent environment for the study of the 'hadronic' photon. The study of direct photoproduction reveals information about the structure of the proton, whereas study of resolved photoproduction may be used to extract information about the photon structure function.
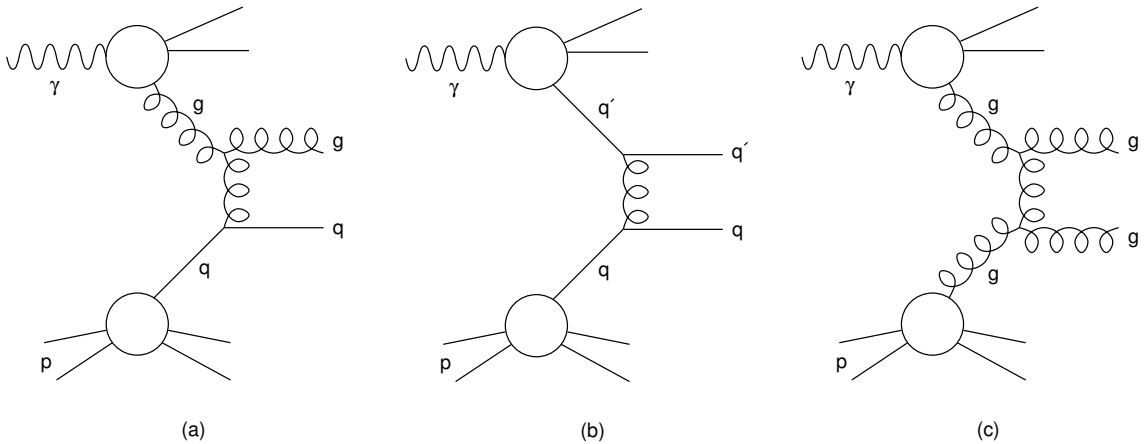
Figure 2.3: Examples of feynman diagrams of processes contributing to resolved photoproduction. (a) $gq \rightarrow gq$ (b) $qq \rightarrow qq$ (c) $gg \rightarrow gg$.

2.4 Multiple Interactions

A comparison of data and standard QCD Monte Carlo calculations including LO matrix elements and QCD radiation effects has been found to provide an inadequate description of the energy flow of these events in the forward direction [13, 14, 11]. The energy flow outside of jets, the so called 'jet pedestal' or 'underlying event', is underestimated by these calculations. One possible answer to this problem is to include an additional energy component from the interaction of the beam remnants. This approach may be justified by the following simple argument. If a pair of partons from proton and the resolved photon undergo a hard scattering, QCD confinement ensures that the remaining unscattered partons are in close enough proximity to also interact. This scenario is known as 'Multiple Interaction'. The probability of additional beam remnant interaction is proportional to the remaining fraction of the photons momentum carried by the photon remnant, after the primary hard scatter. The greater the momentum of the photon remnant, the more probable additional interaction. The nature of the additional interaction is dependent upon the available momentum. This approach has been successfully

used to describe high energy $p\bar{p}$ interactions, where standard QCD calculations underestimated the event energy [15].

2.5   Event Generators

For comparison with data, two different event generators were used, each based on leading order QCD matrix elements for perturbative parton-parton scattering. Generator models are divided into those with and those without beam remnant interactions. One of the generators has the option to include additional interactions of beam remnants, whilst the other includes these processes as an intrinsic part of the model. All calculations with these generators were performed using the same structure functions, namely, the GRV-LO [12] photon structure function and the GRV-LO [16] proton structure function.

2.5.1   PYTHIA

The PYTHIA 5.6 [17] generator is used in combination with the IJRAY [18] photon flux generator to calculate the non-diffractive direct and resolved contributions to the total photoproduction cross section using LO QCD matrix elements. For processes with small transverse momenta p_t, these calculations become divergent, so a cut off value p_t^{cut} is introduced below which hard scatters are not generated. The value of p_t^{cut} is one of the main parameters of this model, and has been adjusted from fits to data. The LUND fragmentation scheme as implemented in JETSET [17] is used, including colour connection from the current system to the remnant system. Any underlying energy is therefore generated only by initial and final state radiation and fragmentation effects. This model, which does not include any beam remnant interactions, is referred to as the PYTHIA Single Interaction model (SI). For the PYTHIA SI Monte Carlo used in this analysis, the p_t^{cut} was set to 2.0 GeV.

The PYTHIA generator has an option to switch on beam remnant interactions, and this gives rise to the PYTHIA Multiple Interaction model (MI). Since each of the interacting beam particles acts essentially as a source of partons, the probability of one pair of partons from the beam particles interacting implies that there must also be a finite probability that additional pairs of partons will interact. It is not unreasonable to assume that these multiple interactions take place independently, so the probability of additional interactions taking place is described by Poisson statistics.

The PYTHIA generator implements both a simple multiple interaction model and a more complex version in which the two interacting beam particles are considered to be extended objects with densities. Only the former is considered in the following analysis.

In this simple model, QCD interactions are extended into the semi-hard regime by lowering the p_t^{cut} to $1.2\,\mathrm{GeV}$. This however has the effect of causing the calculated partonic cross section to be larger than the non-diffractive cross section at low p_t, and so $\sigma_{hard}(p_t)$ partonic scatters must be distributed between $\sigma_{nd}(s)$ events, thus giving the mean number of interactions per event $\bar{n}$ as

$$\bar{n} = \frac{\sigma_{hard}(p_t)}{\sigma_{nd}(s)} \tag{2.15}$$

This regularization scheme effectively dampens the jet cross section at low p_t. The scattering process for the highest p_t parton pair is described by LO matrix elements, which as before includes the possibility of initial and final state radiation processes. For subsequent pairs of partons, semi-hard interactions are described by a perturbative gluon-gluon calculation. The gluons initial momentum is related to the total momentum of the remaining beam remnants, from which the fractional momenta are used to determine the parton densities of the remnants. The inclusion of these additional interactions significantly alters the energy flow in an event. The p_t^{cut} is the main parameter governing the number of multiple interactions per event.

2.5.2   PHOJET

The PHOJET [19] generator is an attempt to describe all components of photoproduction which contribute to the total cross section. This model is based on the two component Dual Parton Model [20] (DPM). The unified treatment of both soft and hard processes allows a continuous transition between, instead of the somewhat artificial separation employed by the PYTHIA generator. Furthermore, multiple parton-parton interactions are in fact an implicit feature of this model, instead of an *ad hoc* addition. Soft hadronic processes are mainly described by colour strings stretched between valence and di-quark and quark and di-quark of the colliding proton and the resolved hadronic photon. Hard processes are described by LO matrix elements, but initial state radiation is not yet included. The fragmentation model used is JETSET. Details of the calculation of different final state configurations are given in [21].

The p_t^{cut} parameter of this model is set to $3\,\mathrm{GeV}$ and, due to the unitarization scheme, small variations in this parameter do not significantly influence calculations. The soft part of this model is tuned from $p\bar{p}$ collisions and low energy photoproduction cross section measurements.

Chapter 3

The H1 Detector

3.1 The HERA Machine

The HERA (Hadron Electron Ring Accelerator) machine [22] is the only colliding accelerator of its type ever built, and will deliver a luminosity of $1.6 \times 10^{31}\,\mathrm{cm}^{-2}\mathrm{s}^{-1}$ when final optimum performance is achieved. HERA consists of two concentric independent accelerators which are designed to store 30 GeV electrons and 820 GeV protons respectively and collide the two counter rotating beams at four interaction points spaced evenly around its 6.5 km circumference. The two beams possess a 'bunched' structure, each beam with a maximum of 210 bunches. In practice, not all bunches have a colliding partner (these are known as 'pilot' bunches) and they are used for background estimation. During the 1993 run period, HERA operated using 26.7 GeV electrons and 820 GeV protons with 84 colliding bunches accompanied by 6 proton and 10 electron 'pilot' bunches and delivered a maximum luminosity of $1 \times 10^{29}\,\mathrm{cm}^{-2}\mathrm{s}^{-1}$.

3.2   The H1 Detector

The H1 detector is located at the north interaction point of the HERA ring. It is designed to measure the kinematics of particles produced by the interactions of the electron and proton beams with near 4π solid angle coverage. The coordinate system chosen to describe the detector is a right handed Cartesian system (x, y, z), with the $+x$ axis pointing to the centre of the HERA ring. The kinematics of particle interactions are most easily described in spherical polar coordinates (θ, ϕ, r) centred on the interaction point. In this system the proton direction corresponds to $0°$ $(+z)$ and the electron direction to $180°$ $(-z)$. These are referred to as the 'forward' and 'backward' directions respectively.

A cut away view of the H1 detector is shown in figure 3.1 in which the major components can be seen, with the exception of the luminosity system. The design is polarly asymmetric due to the nature of the colliding beam kinematics. Moving outwards from the interaction point there are tracking chambers, followed by the liquid argon calorimeter, the electromagnetic layer and the hadronic layer. Surrounding these components is the $1.2\,\mathrm{T}$ superconducting coil. The outer casing, the instrumented iron, serves the dual purpose of muon detector and tail catcher calorimeter as well as the return yoke for the coil. In the forward direction lies the muon spectrometer consisting of a set of drift chambers sandwiching a toroidal bending magnet.

The tracking detectors accurately measure the momentum of charged particles by measuring the curvature of their paths induced by the enclosing superconducting magnet. At high momentum however the curvature of a track is small and the quality of the momentum measurement poor. Particle identification is also possible using $\frac{dE}{dx}$ energy loss measurements of the tracking detectors.

The calorimeters absorb incident energy and convert it to a measurable signal. This allows the energy of both charged and neutral particles to be measured. Although finely segmented, the calorimeters will not generally allow the resolution of

HERA Experiment H1
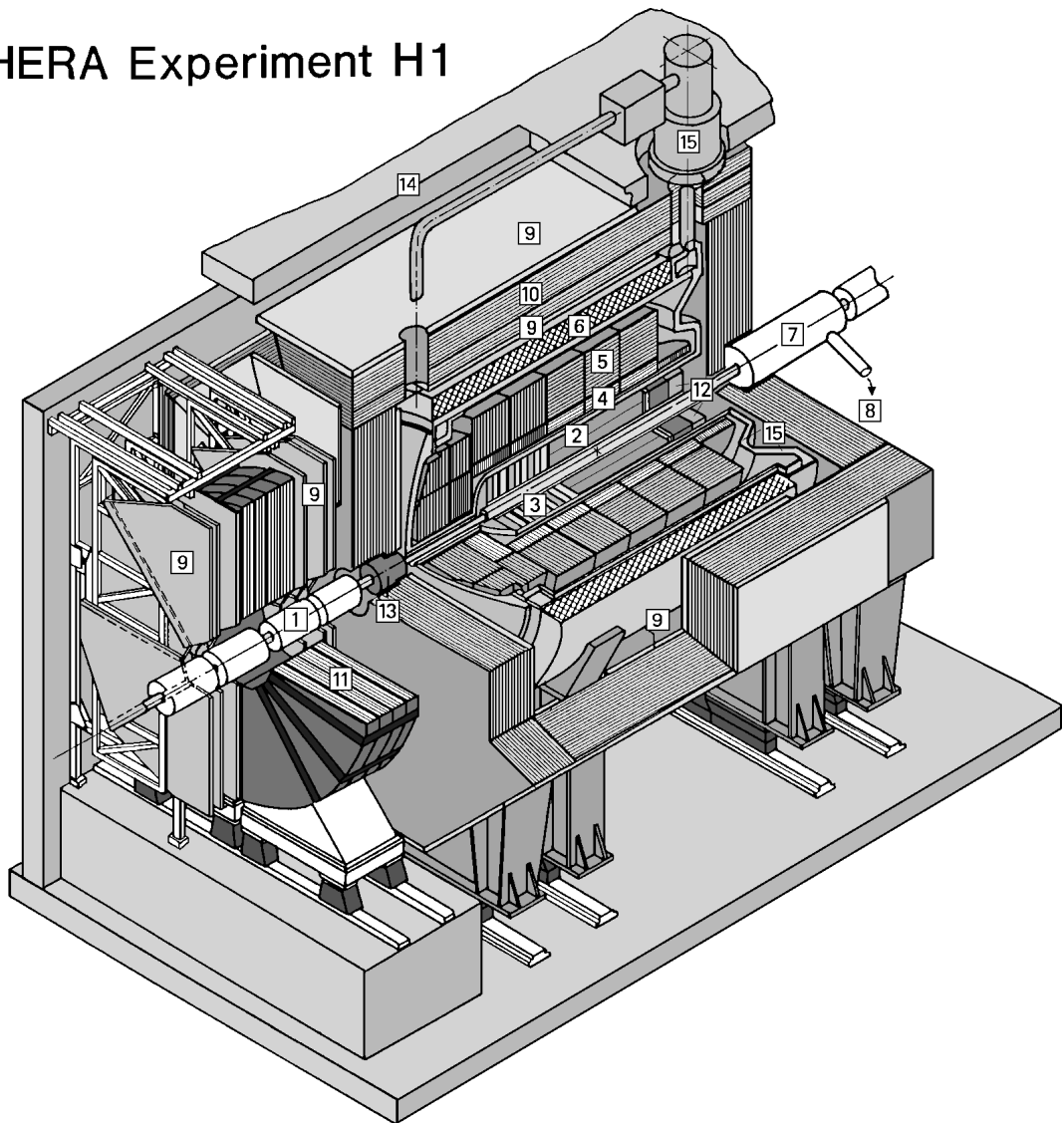
1 Beam pipe and beam magnets	9 Muon chambers
2 Central jet chambers	10 Instrumented iron
3 Forward tracking chambers	11 Forward muon toroid magnet
4 Electromagnetic calorimeter	12 Backward electromagnetic calorimeter
5 Hadronic calorimeter	13 Plug calorimeter
6 Superconducting coil (1.2 T)	14 Concrete shielding
7 Compensating magnet	15 Liquid argon cryostat
8 Helium cryogenics	

Figure 3.1: Cut away view of the H1 detector showing main components, but excluding the Luminosity System. Approximate size $12 \times 10 \times 15$ m.

energy deposits (clusters) into individual particles contributions, except in the case of isolated particles such as the scattered electron in DIS. Identification between electrons or photons and hadrons is also possible. Calorimetric energy resolution is good, particularly for high energy deposits which complements tracking measurements.

3.3   Calorimetry

All the calorimeters in H1 work on the same principle. Calorimeters are constructed from alternate layers of passive dense material and instrumented active sampling material. Energetic particles incident on the calorimeter lose energy by interaction with the absorber layers, producing showers of secondary particles which subsequently lose energy by further showering or interaction with the sampling material. By measuring the signals produced in the active sampling regions, the shower development can be periodically sampled. From these measurements the total energy of the particle can be measured and the longitudinal and transverse shower profile determined.

In electromagnetic calorimeters, electrons and photons produce showers of lower energy electrons and photons via bremsstrahlung and pair production processes. The development of an electromagnetic shower in a particular absorber material is characterised by the radiation length X_0, the mean longitudinal length traversed over which an electron loses the fraction $1/e$ of its energy.

For hadronic calorimeters, energy loss is achieved by inelastic nuclear collision, producing lower energy hadrons which undergo further inelastic interaction. The characteristic length of the development of hadronic showers in a particular material is determined by its nuclear interaction or absorption length λ.

The four component calorimeters of the H1 detector, namely, the Liquid Argon Calorimeter (LAC), the Backward Electromagnetic Calorimeter (BEMC), the

Plug Calorimeter (PLUG) and the Tail Catcher (TC) are shown in figure 3.1. In combination these calorimeter systems provide a high degree of hermeticity, almost 4π, the losses being due to the necessity of the beam pipe.
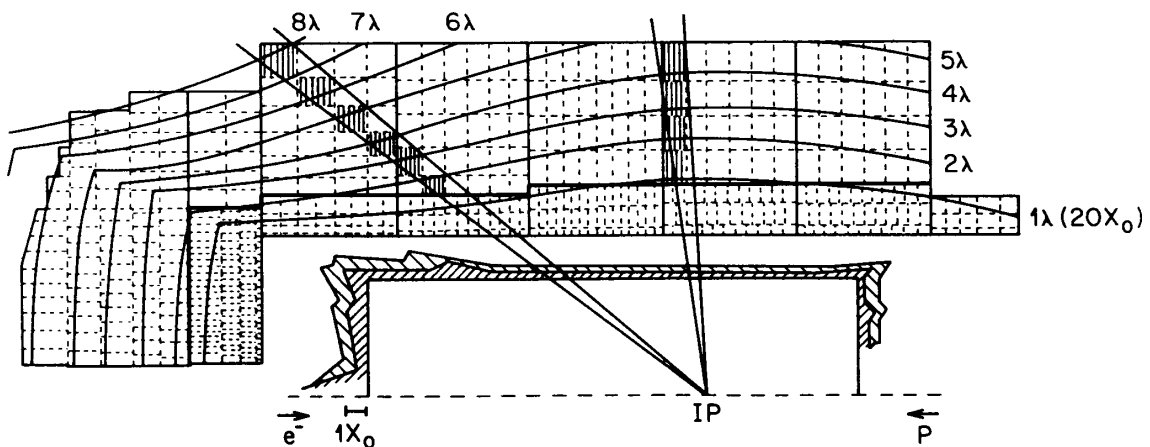
Figure 3.2: The structure of the hadronic and electromagnetic sections of the LAC calorimeter showing contours of iso-λ. Note the pointing geometry of the cells.

3.3.1 The Liquid Argon Calorimeter

The LAC calorimeter [23] is the main calorimeter of H1 and covers the angular range of $0° < \phi < 360°$, $4° < \theta < 153°$ making it the principal calorimeter for the detection of the hadronic final state. The LAC is divided into two parts, the inner electromagnetic section (EMC) and the outer hadronic section (HAC). The EMC is constructed from absorber layers of 2.4 mm lead, to give a radiation depth varying from $20\,X_0$ in the barrel region to $30\,X_0$ in the forward direction. The HAC uses stainless steel absorber layers of thickness 19 mm to give a total depth of between 5 to 8 interaction lengths. The LAC is highly segmented in both sections and has around 45000 cells in total, arranged in a pointing geometry designed to facilitate a calorimetric triggering system (see figure 3.2).

The energy resolution of the LAC has been measured in test beams and was found to be $\frac{\sigma_E}{E} = \frac{12\%}{\sqrt{E}} \oplus 1\%$ for electrons [24] and $\frac{\sigma_E}{E} = \frac{50\%}{\sqrt{E}} \oplus 2\%$ for pions [25]. The hadronic energy scale and resolution have been measured using the transverse momentum balance of the scattered electron and hadronic system in DIS events and are known to a precision of 5% and 10% respectively.

3.3.2   The Backward Electromagnetic Calorimeter

This calorimeter was designed specifically for the precise measurement of the scattered electron from deep inelastic processes. The scattering angles covered are $151° < \theta < 177°$ with full azimuthal acceptance which is matched to the acceptance of the LAC to provide continuous polar coverage. The BEMC is constructed from 88 individual stacks providing a high degree of segmentation. Each stack is constructed from 50 scintillator sampling layers interleaved with 49 layers of $2.5\,\mathrm{mm}$ sheet lead. This gives a radiation length of $X_0 = 22.5$ or interaction length $\lambda = 0.97$. The electromagnetic energy resolution has been measured to be $\frac{\sigma_E}{E} = \frac{10\%}{\sqrt{E}} \oplus 1\%$ [26], and the calorimetric spatial resolution $\sim 3\,\mathrm{cm}$. Hadrons penetrating the BEMC typically deposit 30% of their energy, and approximately 30% of hadrons do not interact at all. In conjunction with the tail catcher, a hadronic energy resolution of $\frac{\sigma_E}{E} = \frac{80\%}{\sqrt{E}}$ [26] has been achieved.

3.3.3   The Plug Calorimeter

This relatively small calorimeter is situated between the beam pipe and the LAC calorimeter in the forward direction and is designed to measure the energy of particles emitted close to the beam pipe, ie the proton remnant. The angular range covered is $0.6° < \theta < 3.0°$ overlapping slightly with the LAC. The PLUG is constructed from 9 layers of copper absorber plates interleaved with 8 large area silicon detectors, giving an interaction length of $\lambda = 4.25$. The energy resolution of the plug has been estimated from Monte Carlo to be $\frac{\sigma_E}{E} = \frac{150\%}{\sqrt{E}}$ [26].

3.3.4 Tail Catcher

This calorimeter system is build into the instrumented iron. Layers of iron are interleaved with limited streamer tubes (LSTs) and any energy which penetrates through the HAC (a condition known as 'punch through') is then detected by the LST system. Test beam results show that the energy response is linear up to 40 GeV with a resolution of $\frac{\sigma_E}{E} = \frac{100\%}{\sqrt{E}}$ [26].

3.4 Tracking Detectors

The H1 tracking detectors are located inside the uniform magnetic field of the superconducting coil and are divided into three separate systems, the Central Tracking Detector (CTD), the Forward Tracking Detector (FTD) and the Backward Multi-wire Proportional Chamber (BPC), covering the angular range $15° < \theta < 165°$, $7° < \theta < 25°$ and $155° < \theta < 174°$ respectively with full azimuthal acceptance. A schematic diagram of the layout of these chambers is shown in figure 3.3.

Two different types of chambers are used, namely drift chambers and multi-wire proportional chambers (MWPCs). Each tracking chamber consists of a sealed gas volume in which one or more sense wires are strung. In addition to the sense wires, field shaping wires or strips are usually also present. The sense wires are kept at a high positive voltage and in conjunction with field shaping cathodes produce a uniform electric field across the chamber, except at very small distances from the sense wires where the field grows rapidly.

Charged particles traversing the chamber cause electrons to be liberated from the gas along their trajectories. These electrons then drift under the influence of the electric field toward the sense wires. When they reach the strongly increasing field close to the sense wires, they start to liberate other electrons via ionising collisions with gas molecules and an avalanche of electrons develops. This produces a tiny signal which is amplified and read out by the chambers electronics. The time

taken for the primary electron to reach the sense wire is usually a simple function of distance travelled. Since the spatial location of the sense wire is accurately known, the transverse distance between the charged particle track and the sense wire can be calculated. From a series of such measurements, the path of the particle can be fully reconstructed.
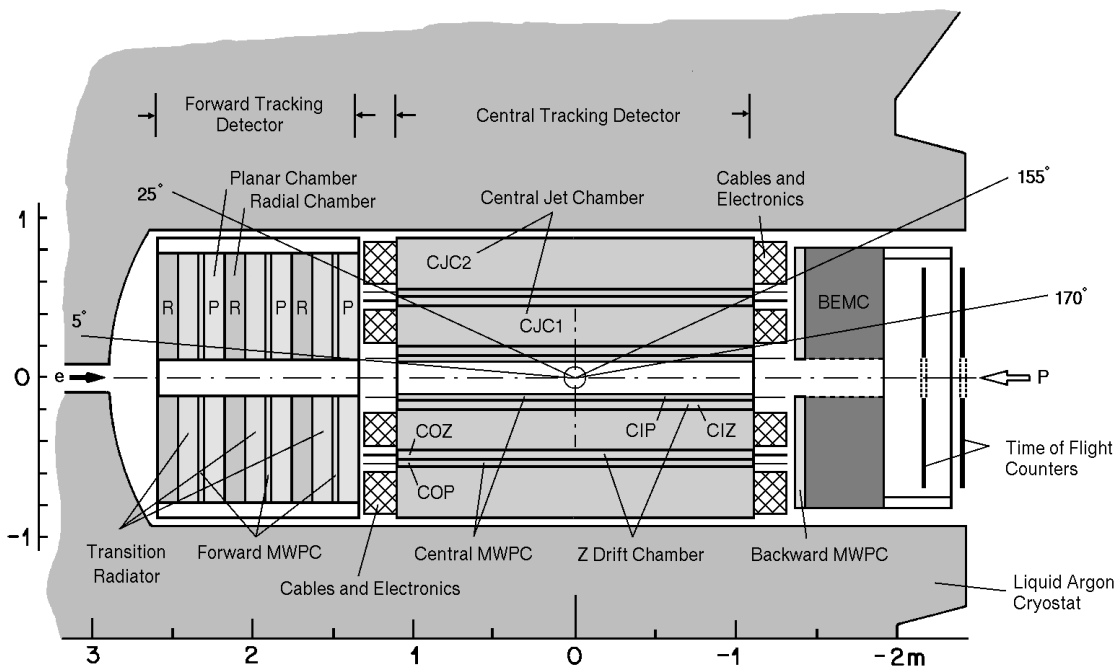
Figure 3.3: The H1 tracking system in $r-z$ projection.

Drift chambers and MWPCs differ because MWPCs do not have a drift volume. Instead their sense wires are placed so that the adjacent wire's avalanche regions overlap. This enables signals from this type of chamber to be read out very quickly and they are generally used for the construction of fast triggering systems.

3.4.1 The Central Tracking Detector

The central tracking detector (CTD) is composed of two jet chambers CJC1 and CJC2, which accurately measure the $r-\phi$ coordinates of tracks, and two thin drift chambers, the Central Inner Z chamber (CIZ) and the Central Outer Z chamber (COZ), which accurately measure the z coordinate. The linking of measurements made by these four chambers allows the accurate reconstruction of tracks.
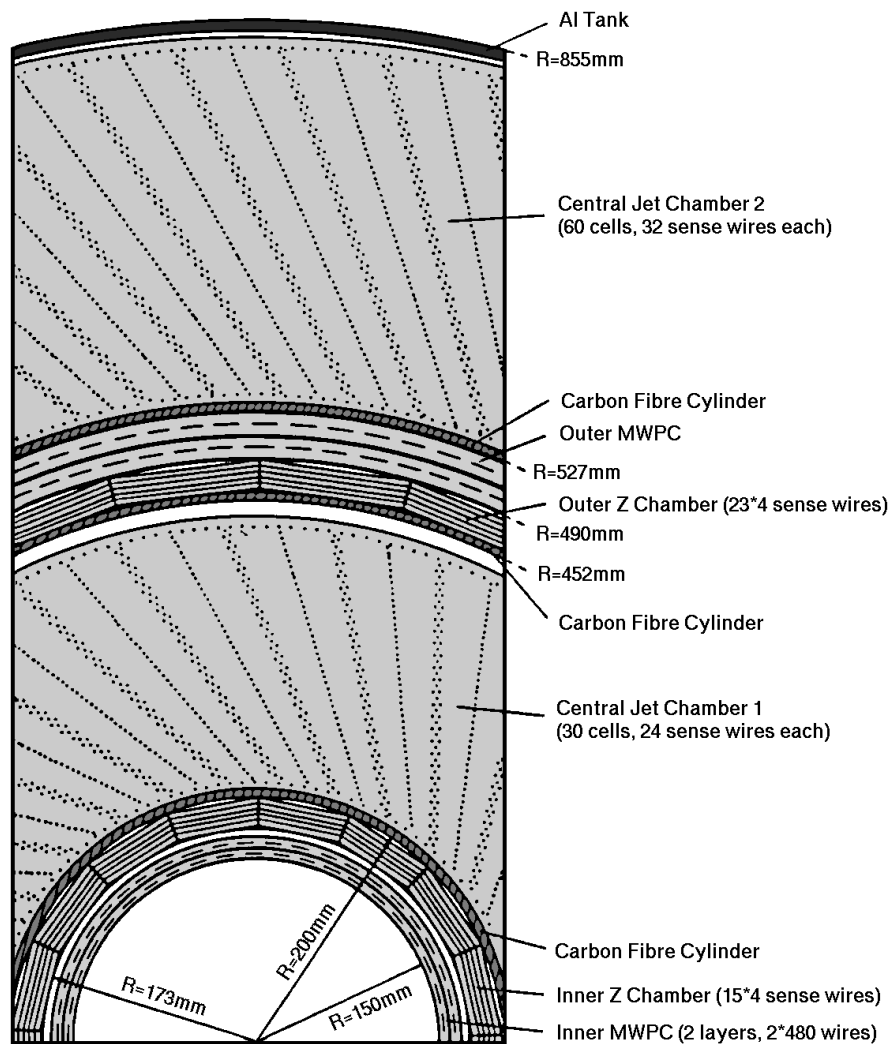
Figure 3.4: The central tracking system in $r-\phi$ projection.

These chambers are all located concentrically around the z axis giving a sensitive cylindrical volume of $-1.125 < z < 1.125\,\text{m}$ and $20.3 < r < 84.4\,\text{cm}$ (see figure 3.4). The inner of the jet chambers (CJC1) is constructed from thirty identical drift cells which each contain 24 staggered sense wires running parellel to the beam axis along with accompanying field forming wires. The outer jet chamber (CJC2) has sixty drift cells each containing 32 sense wires. The wire planes of CJC1 and CJC2 are tilted from the radial direction by approximately 30°. This brings a number of advantages including assisting with the resolution of mirror tracks by connection to adjacent cells, and the elimination of systematic measurement errors at cell edges.

The $r - \phi$ and z coordinates are calculated from drift times and charge division respectively, with resolutions of $\sigma_{r-\phi} \sim 350\,\mu\text{m}$ and $\sigma_z \sim 5\,\text{cm}$ [26]. The Z chambers are constructed from four layers of sense wires oriented in planes transverse to the z axis. For these chambers the z coordinate comes from drift time measurement, with a resolution of $\sigma_z \sim 200 - 500\,\mu\text{m}$ [26]. The combined measurements of the CTD gives a momentum resolution of $\frac{\sigma_p}{p^2} \sim 0.003\,(\text{GeV/c})^{-1}$ and angular resolutions in θ and ϕ of $\sigma_\theta \sim 1.2\,\text{mrad}$ and $\sigma_\phi \sim 0.1\,\text{mrad}$ [26].

Also incorporated into the CTD are two layers of multi-wire proportional chambers, the Central Inner proportional Chambers (CIP) and the Central Outer Proportional Chambers (COP). Signals from these chambers are used for track pointing triggering systems.

3.4.2   The Forward Tracking Detector

The Forward Tracking Detector (FTD) increases the accessible range of track measurement in the forward direction, complementing the acceptance of the central tracking detector. It has an active cylindrical volume of $15 < r < 79\,\text{cm}$ and $134 < z < 254\,\text{cm}$, giving it an acceptance of between 5° and 30° in the laboratory. The FTD is constructed from three identical supermodules (SM). Each

SM is composed of (in order of increasing z) a planar module consisting of a set of drift chambers which measure $r-\phi$ coordinates, a set of MWPC chambers used for triggering purposes, a transition radiator used in particle identification by $\frac{dE}{dx}$ energy loss measurements and a radial module consisting of a set of drift chambers which measure the ϕ coordinate.

Inside each planar module the planar chambers are organised into three identical layers each rotated about the z axis at $0°$, $+60°$ and $-60°$ respectively to the vertical, and are referred to as the X, U and V orientations (see figure 3.5). Each orientation consists of 32 drift cells of width $5.7\,\mathrm{cm}$ and varying lengths forming a sensitive disc of radius $79\,\mathrm{cm}$ perpendicular to the z axis. Each cell contains 4 sense wires, staggered about z by $270\,\mu\mathrm{m}$ and separated in z by $6\,\mathrm{mm}$.
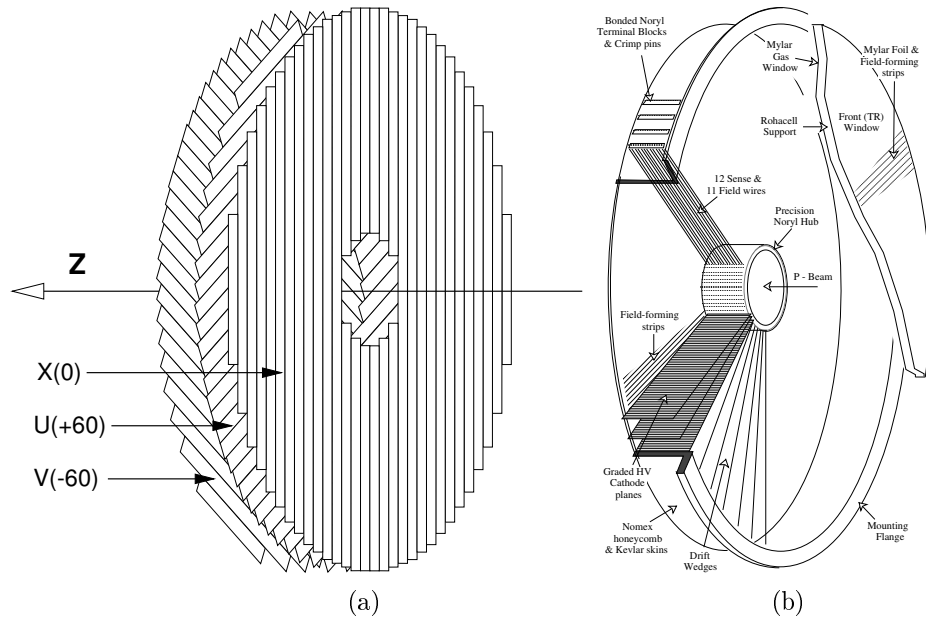
Figure 3.5: (a) A forward tracker planar module showing the chamber orientation of the three XUV layers. (b) Cut away view of a radial module showing internal features.

Each radial module is constructed from 48 wedge shaped drift chamber segments each subtending $7.5°$ in ϕ. Each segment contains twelve sense wires strung

radially from the inner hub to the outer shell, spaced 1 cm in z and staggered by 288 μm to permit resolution of left-right ambiguity. The sense wires are interleaved by eleven field wires. The drift time measurements from the radial chambers provide an accurate measurement of track saggita thus giving a very precise determination of track momentum. In addition to track measurement the radial modules also detect additional charge liberated by X-rays produced by interaction with the transition radiator situated in front of the radial modules. This additional information is used for identification of particles by $\frac{dE}{dx}$ [27] energy loss measurement. The performance of the FTD is considered in detail in chapter 6.

In addition to its tracking capabilities this detector is also equipped with multi-wire proportional chambers (FWPCs) which are situated behind the planar chambers. Each FWPC module contains two layers of proportional chambers which are used for triggering purposes.

3.4.3   The Backwards Multi-wire Proportional Chambers

The Backward Multi-wire Proportional Chambers (BPC) are situated in front of the BEMC calorimeter. The BPC is constructed from four identical planes of sense wires oriented at 45° with respect to each other. The BPC is essentially a triggering system for particles entering into the BEMC calorimeter, however, information from the BPC in the form of space points is used to improve the identification and measurement of electrons in low Q^2 DIS events.

3.5   Muon Detection and Identification

Muons have historically provided signals for new processes, so excellent muon detection is vital at H1. Excellent muon detection is also imperative for the effective removal of cosmic and beam halo backgrounds. To these ends, H1 is equipped with both a general muon detection system built into the iron return yoke

of the solenoid which surrounds the whole detector, and in addition, it also has a muon spectrometer in the forward direction designed for the detection of high energy muons originating from rare or possibly undiscovered processes.

3.5.1 The Forward Muon Detector

The Forward Muon Detector (FMD) is comprised of two sets of drift chambers sandwiching the toroidal bending magnet. Each set of chambers is constructed from three separate layers, two measuring the polar angle θ and one measuring the azimuthal angle ϕ. This detector has an acceptance of $3° < \theta < 17°$ and is can accurately measure muon momenta in the range $5 - 200\,\mathrm{GeV/c}$, the lower limit being determined by the amount of dead material present before the spectrometer.

3.5.2 The Digital Muon System

The outer iron layer of the detector is interleaved with gaps which contain limited streamer tubes (LSTs). The LSTs are constructed from a basic Lurnayl extrusion unit housing eight chambers each of cross section $10 \times 10\,\mathrm{mm}^2$. Running through the centre of each chamber is a sense wire which is grounded. Three sides of the chambers are coated with a low resistivity material which is held at high positive voltage while the fourth side retains its high resistivity and to it are attached either calorimeter pads or strips. The field in the chamber is of such a magnitude that any electrons liberated by a charged track immediately initiate an avalanche (streamer). The z position along the chamber is calculated from the identity of the strip running perpendicular to the wire. In total there are sixteen layers of LSTs interleaved with the iron.

3.6   The Luminosity System

The Luminosity System consists of a photon detector (PD) and a Čerenkov counter (CV) which form the photon arm, and an electron tagger (ET) (see figure 3.6). These are used to provide a fast online measurement of the luminosity by measuring the photon and electron originating from the bremsstrahlung reaction $ep \to ep\gamma$[1] for which the cross section is calculable and accurately known.
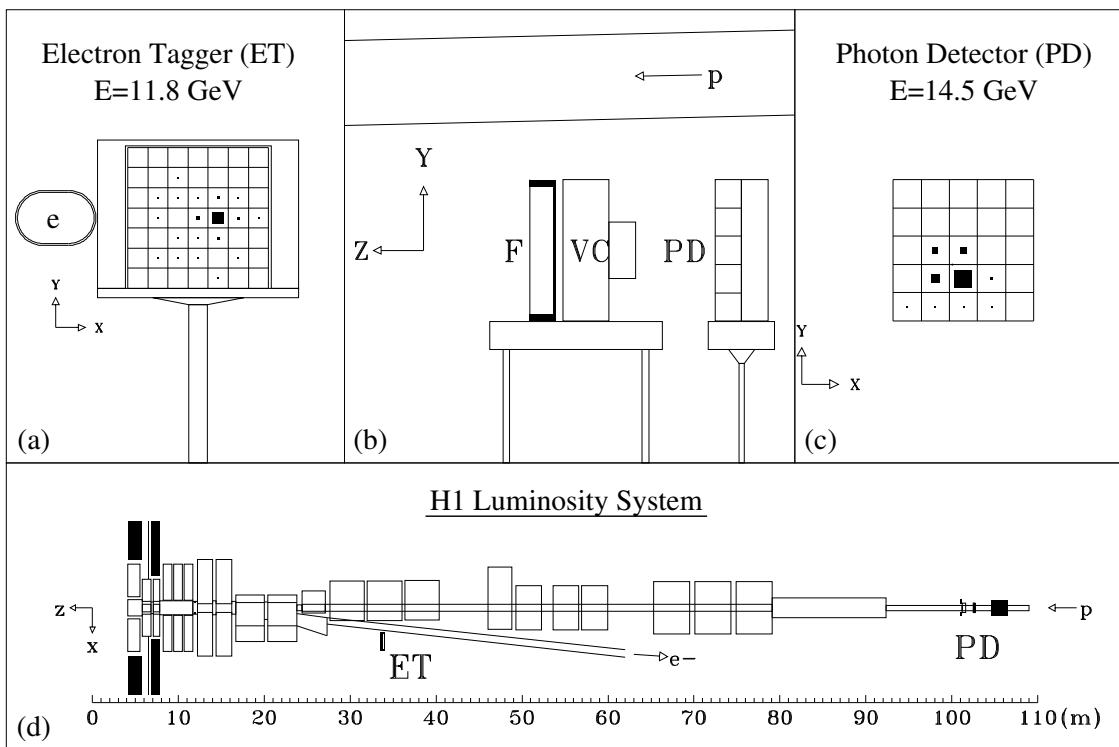
Figure 3.6: A typical bremsstrahlung event as seen by the luminosity system.

Photons from the bremsstrahlung process are emitted collinearly in the incident electron direction and pass out of the beam pipe at an exit window at $z = 92.3\,\mathrm{m}$ where the beam pipe bends upward and enter into the photon detection system. The photons first pass through a $2\,X_0$ lead filter which protects the system

---

[1]Also known as Bethe-Heitler scattering.

from synchrotron radiation. After this the photon then traverses a $1\,X_0$ Čerenkov counter which is primarily used to reject early photon showers, before it hits the photon detector. The photon detector, situated at $z = 102.9\,\mathrm{m}$, is a crystal calorimeter build out of 25 TlCl/TlBr crystals with a total surface area of $100 \times 100\,\mathrm{mm}^2$ and a radiation depth of $22\,X_0$.

The accompanying electron is bent by the HERA beam magnets and passes out of the beam pipe through an exit window at $z = -27.3\,\mathrm{m}$, and then hits the electron tagger at $z = -33.4\,\mathrm{m}$. The electron tagger is constructed from 49 crystals of the same type as the photon detector, and has a total area of $154 \times 154\,\mathrm{mm}^2$. The acceptance of the tagger is strongly dependent on the beam optics and a detailed understanding of these is required for precise calculation of luminosity. The online values of luminosity is checked off-line using methods which are insensitive to beam optics. The electron tagger accepts electrons which are scattered at angles below $\theta' \leq 5\,\mathrm{mrad}$ $(\theta' = \pi - \theta)$. Both the photon and electron taggers have a positional resolution of better than $1\,\mathrm{mm}$ and an energy resolution of $\frac{\sigma_E}{E} = \frac{10\%}{\sqrt{E}} \oplus 1\%$ [26].

3.7   Scintillating Detectors

Several sets of scintillator walls have been installed in the backward region of the H1 detector to veto proton induced beam background (ie beam gas and beam wall interactions). These backgrounds produce both energetic showers of hadrons which range over lengths of 30 m and halo muons. Meticulous detection and removal of these backgrounds is therefore vital.

3.7.1   The Time of Flight System

The time of flight System (ToF) is a dual layered scintillator hodoscope located perpendicular to the beam line at $z \sim 2\,\mathrm{m}$ (see figure 3.3). The inner layer (ToF1) at $z = -1.95\,\mathrm{m}$ is constructed from sixteen $317 \times 317\,\mathrm{mm}^2$ sheets of

3 cm thick scintillator which is sandwiched by $1.1\,X_0$ lead shielding to protect it from synchrotron radiation. The outer layer (ToF0) at $z = -2.25\,\mathrm{m}$ is similar except that only 8 sheets of scintillator of twice the vertical dimension are used. Both ToF0 and ToF1 require high field photomultiplier tubes in order to function inside the $1.2\,\mathrm{T}$ magnetic field. The coincidence timing resolution of the hodoscope is $\sim 2\,\mathrm{ns}$.

The ToF system works on the principle that background particles originating from upstream of H1 will enter the ToF system approximately synchronously with the proton bunch, whereas particles originating from the interaction vertex will enter at $\frac{2\Delta z}{c}$ later, where Δz is the distance from the interaction vertex to the ToF. This amounts of a difference of $13\,\mathrm{ns}$, ignoring smearing from the proton bunch length.

Signals from ToF0 and ToF1 are strobed in three temporal windows of a single bunch crossing. The first of these windows, called the 'interaction' window is positioned around the expected time of arrival of particles from genuine events, and is $13\,\mathrm{ns}$ long. Immediately preceding this is the 'background' window, located to coincide with the arrival of upstream particles from beam induced backgrounds, with a $25\,\mathrm{ns}$ length. The final window, known as the 'global' window encompasses signals from the entire bunch crossing. The most important use of these ToF signals is to construct 'background veto' subtriggers which are used in conjunction with physics triggers to suppress proton induced background interactions, leading to a 99% reduction in overall trigger rates.

3.7.2   The Veto Wall

This system is similar to the ToF system but is located further down stream. The inner veto wall is located at $z = 8.1\,\mathrm{m}$ and consists of two $6\,\mathrm{mm}$ layers of scintillator of dimensions $100 \times 90\,\mathrm{cm}^2$ and covers the area around the beam pipe down to $r = 11\,\mathrm{cm}$. The outer wall is at $z = 6.5$ and is of area $5 \times 4\,\mathrm{m}^2$, constructed of 10 sheets of scintillator each of dimensions of up to $2.1 \times 0.9\,\mathrm{m}^2$.

This wall overlaps with the inner veto wall and extends out to cover nearly all of the liquid argon calorimeter and muon end cap. The two walls are shielded from electromagnetic showers by layers of 4 cm thick lead.

Background is identified by both walls in a manner similar to the time-of-flight system. The coincidence resolution achieved by the inner veto wall is ± 3 ns and for the outer wall ± 8 ns thus enabling a clear separation of proton induced background.

3.8 DAQ and Trigger Systems

The short bunch crossing time of HERA (~ 96 ns) and the large number of electronic channels used by H1 generate data at a rate of ~ 3 MBytes per event. It is not physically possible to read out all detector systems at anything approaching this speed. Therefore a triggering system is used which selects only those events of potential interest to be read out. The time taken for the DAQ system to collect, process and signal the acceptance of an event amounts to a significant number of bunch crossing periods, so a pipelined architecture for the triggering and readout system [28] has been adopted.

3.8.1 Central Trigger

The trigger pipeline [29] stores 22 successive event trigger signals which are processed by the fast central trigger logic. Each of these trigger signals is composed of 128 individual trigger elements which are generated by fast triggering detector subsystems such as FADC energy sums from the calorimeter, veto-wall and time-of-flight systems, reconstructed vertex position from proportional chambers etc. The coincidence of the trigger signal with a predetermined set of trigger elements (so called 'triggers') causes the central trigger logic to send an L1-Keep signal to all detector subsystems.

3.8.2   Detector Readout

During the normal operation of a detector subsystem, data are constantly being read into a pipelined buffer. When a L1-Keep signal from the central trigger is received, this pipeline is frozen and 'dead time' commences, during which the detector is not sensitive. Each detector subsystem then has $800\,\mu s$ before the pipelines are enabled during which it must read out the data from the pipelined buffer and transfer it to the CDAQ system. Provision was made during the design of the trigger for L2 and L3 layers of triggers which will be required when full design luminosity is achieved. These triggers will be topologically based and are currently under development.

3.8.3   L4 Filter Farm

This system provides the final online event selection algorithms. For this purpose a specially optimised version of H1REC [30] reconstructs the event until a definite accept or reject decision can be made. A small subsample of events which are rejected by the filter farm are kept for further analysis to monitor physics event losses.

3.9   H1 Software

The Monte Carlo simulation of generator data is provided by H1SIM [31] which is based on the framework of GEANT [32]. Generated particles are tracked through the detector and their energy losses calculated in various materials traversed. Detector responses to the energy deposition are then calculated so that the simulated data can then be processes through the same software chain as real data.

Data and simulated Monte Carlo are both reconstructed by H1REC [30] software module, which in conjunction with the relevant calibration constants held

by the H1 database H1DB [33], perform track and cluster reconstruction on the raw data signals.

Chapter 4

Event Selection

4.1   Introduction

During the 1993 running period H1 collected approximately $0.6\,\mathrm{pb}^{-1}$ of data from a total $1\,\mathrm{pb}^{-1}$ of luminosity delivered by HERA. After an initial selection of runs for which the detector was working efficiently and all major components were fully operational, a total of $290\,\mathrm{nb}^{-1}$ of data remained. This chapter describes the selection process used to obtain a sample of hard photoproduction events which are analysed in following chapters.

4.2   1993 Run Preselection

The starting point for analysis is 1993 data which passes the ELAN93 [34] run selection cuts. These selection cuts are designed to give the most homogeneous detector data taking conditions while rejecting as little data as possible. The main criteria used by this run selection are as follows:

- Excluded Run Periods - Runs with non standard data taking conditions (eg shifted vertex, no magnetic field, etc) are rejected.

- Subdetector Status - All major subdetectors are in the readout and working correctly. (ie LAR, CJC, LUMI, ETAG and BEMC)

- Noisy Runs - Runs which contained excessive coherent noise in the calorimeter are rejected.

- Number of DIS Events per nb^{-1} - Runs which contain an anomalous number of DIS events per nb^{-1} are rejected.

4.3 Event Selection

The selection of photoproduction events is based on the ST83 physics trigger. This physics trigger is composed of three logical conditions; a tagged electron (eTAG), a vertex pointing track in the central tracker ($DCr\phi$) and a general background veto. The eTAG trigger signal comes from the luminosity system, and is generated by the coincidence of over $4\,\mathrm{GeV}$ of energy deposited in the electron tagger and no energy deposited in the photon detector. The $DCr\phi$ signal is generated by a dedicated hardware subtrigger system [35] which uses information from the CJC1 and CJC2 chambers in the CTD. This subtrigger searches for tracks in $x-y$ plane, which appear as circles. Such circles can be parameterise by their curvature κ, azimuthal angle ϕ and distance of closest approach to the vertex DCA. Since good tracks originating from the vertex have $DCA \sim 0$, bad tracks may be rejected by a masking technique in $\kappa - \phi$ parameter space. The design of the trigger is such that only tracks with transverse momentum of greater than $400\,\mathrm{MeV/c}$ cause a positive trigger signal. In common with most physics triggers, the $DCr\phi$ trigger uses a general background veto trigger which makes use of the ToF and veto wall systems. This greatly reduces out of time back ground events.

In addition to being triggered by the ST83 trigger, events must pass a number of other technical checks. These are listed below.

- The forward tracker high voltage is switched on and has subdetector status 'good'. This condition was not included in the ELAN93 run selection.

- No cosmic muons are found in the event. The standard L5 topological muon finder is used.

- Beam gas veto bit not set.

Events surviving the above technical cuts are then subjected to the following physics cuts which further reduce background levels:

- $-35 < z_{vtx} < 25\,\mathrm{cm}$ - The z coordinate of the vertex must lie within these distances of the nominal interaction point consistent with the spread in the vertex due to the proton bunch length. This reduces background from beam-gas and satellite bunches.

- $8 < E_{tag} < 20\,\mathrm{GeV}$ - Cut placed on reconstructed scattered electron energy E_{tag} ($0.25 < y < 0.7$) to ensure good acceptance for electrons in the electron tagger. (For the case of Monte Carlo, events outside this range were not simulated.)

4.4   Final Event Sample

Events passing all previously defined selection criteria are then subjected to the jet finding algorithm QJCONE [36] (see chapter 5 for full details). This algorithm is run using the parameters $E_t^{jet} > 6\,\mathrm{GeV}$ and $R = 1.0$. Events are selected if they pass the following cuts which are designed to minimise the contamination of jets from the photon remnant:

- ≥ 2 jets found with $-0.5 < \eta^{jet} < 2.5$

- $\Delta\eta^{jet} < 1.2$ or difference in η of the two jets leading in E_t, in the case of more that two jets.

After all selection procedures a total of 1372 events remained. The contamination of the event sample was estimated to be $\sim 1\%$, and is henceforth neglected.

4.5 Event Kinematics

A comparison of the the kinematic variable E_{tag} is shown in figure 4.1(a). Reasonable agreement is seen between data and PYTHIA Monte Carlo, both with and without multiple interactions. The z_{vtx} distributions shown in figure (b) are of a similar width, but data is offset compared to Monte Carlo. This is because the exact interaction point for the 1993 run period was unknown at the time the Monte Carlo was generated. Table 4.5 contains a summary of the z_{vtx} parameters for data and Monte Carlo. The mean μ and width σ are given from a Gaussian fit performed over the accepted range in z, accounting for the relative offsets of Monte Carlo.

	Data	PHOJET	PYTHIA MI	PYTHIA SI
μ cm	-4.43	-5.66	-3.34	-3.11
σ cm	9.57	9.36	9.84	9.73
χ^2/ndf	1.10	1.30	1.16	1.23

Table 4.1: Summary of the distribution of the position in z of the event vertex. Parameters are given from a Gaussian fit to the acceptance region in z.
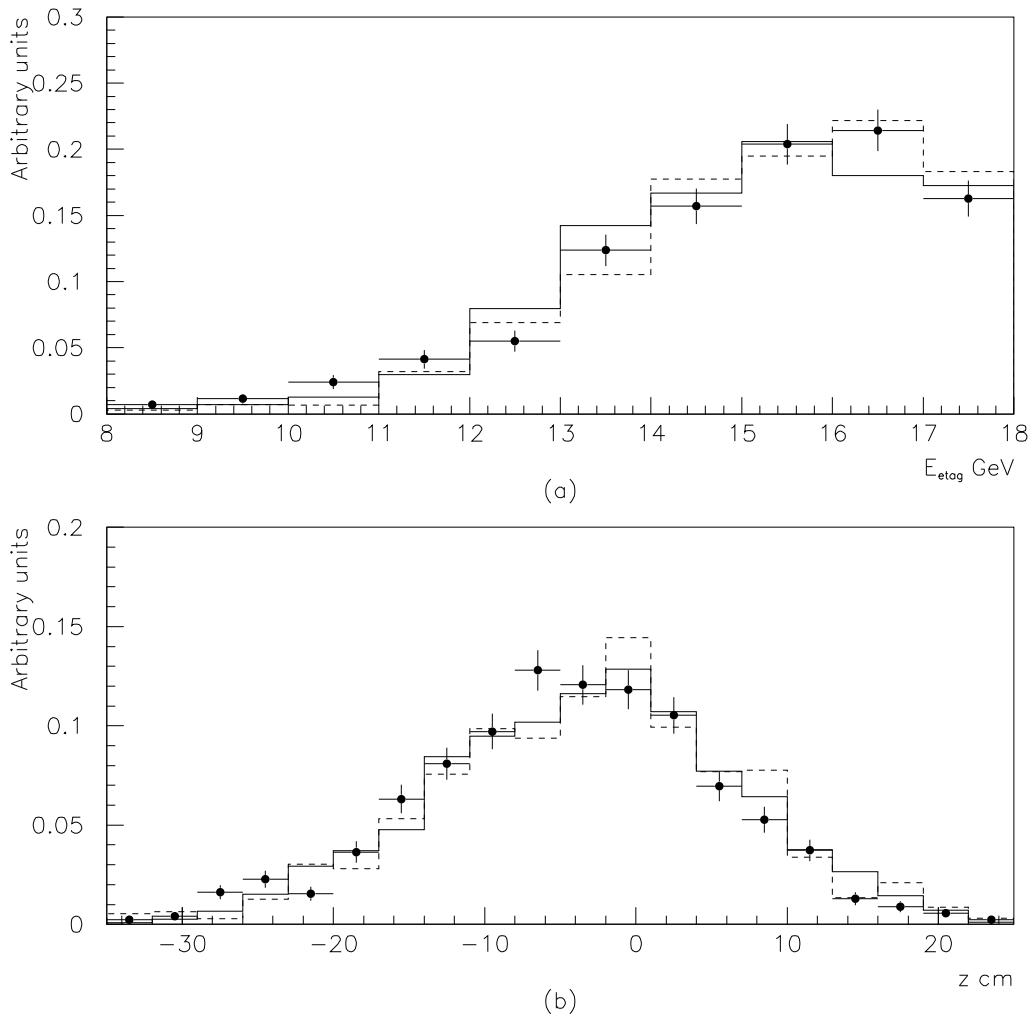
Figure 4.1: (a) The E_{tag} spectrum of the final selected events. (b) The distribution of the reconstructed z_{vtx} vertex position. (Data points, PYTHIA MI solid histogram, PYTHIA SI dashed)

4.6 Triggering

To check for any differences in triggering performance between data and Monte Carlo simulation, the DC$r\phi$ subtrigger efficiency is calculated relative to the eTAG subtrigger. The eTAG subtrigger is known to be well simulated from studies of the luminosity system. For Monte Carlo simulation, the eTAG trigger is simulated to be 100% efficient for electrons within the permitted range of acceptance. The actual efficiency of the electron tagger known from measurements made by the luminosity system to high accuracy and this is used to provide a correction which is then applied to Monte Carlo as a function of y, the fractional energy loss of the scattered electron. Since the efficiency of the electron tagger is always derived from data it is only necessary to examine the relative performance of the DC$r\phi$ subtrigger.

The efficiency of the DC$r\phi$ trigger is dependent on the topology of charged final state particles in an event. Its efficiency is examined as a function of two variables which are dependent on event topology. In this instance x_γ and the pseudorapidity of the jet trailing in η are chosen. Figure 4.2 shows these distributions and it is seen that data agrees reasonably well with Monte Carlo, indicating that the DC$r\phi$ trigger hardware is particularly well simulated.
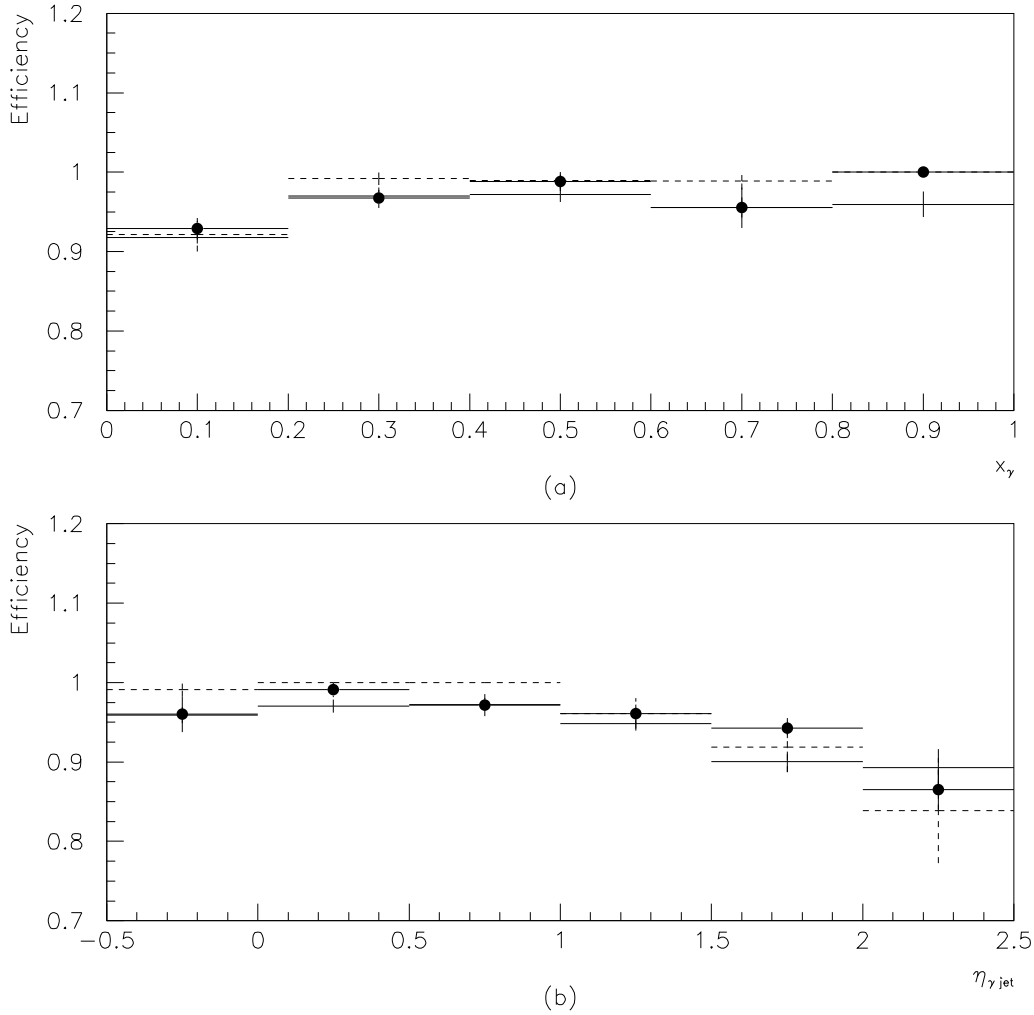
Figure 4.2: Comparison of DCrϕ subtrigger efficiency relative to eTag subtrigger. (a) The efficiency as function of x_γ^{rec}. (b) The efficiency as a function of angle of the jet trailing in η (γ hemisphere jet). (Data points, PYTHIA MI solid histogram, PYTHIA SI dashed)

Chapter 5

Jet and x_γ Reconstruction

Jet reconstruction gives kinematic information about the partons involved in the hard scattering process which in turn enables x_γ, the fraction of the photons momentum carried by its interacting parton, for the event to be reconstructed (see section 2.1). In this chapter the quality of reconstruction of jet parameters and x_γ reconstruction is considered. The jet algorithm used in this analysis is QJCONE [36] as implemented in the H1PHAN [37] analysis package. The QJCONE algorithm is a cone algorithm based on the Snowmass [38] jet definition.

5.1   The QJCONE Jet Algorithm

For this analysis jet finding is performed using solely calorimetric energy measurements, using a grid of $N_\eta^{cell} \times N_\phi^{cell}$ cells in $\eta - \phi$ space. A jet is defined as a cone of radius R containing at least $E_{t\ min}^{jet}$ transverse energy, such that

$$\sum_{cell} E_t^{cell}(\eta^{cell}, \phi^{cell}) > E_{t\ min}^{jet}, \tag{5.1}$$

where

$$\sqrt{(\eta^{cell} - \eta^{jet})^2 + (\phi^{cell} - \phi^{jet})^2} < R \tag{5.2}$$

Jets are sought by considering in turn each cell with energy greater than $E_{t\ ini}^{jet}$ (the jet initiator energy) and calculating the transverse energy of all cells contained within radius R of their centre. If the transverse energy exceeds $E_{t\ min}^{jet}$ the initiator cell is stored in a list of candidate jets, along with its transverse energy. In this way the set of all possible candidate jets is found. The list of candidate jets is now sorted in order of decreasing transverse energy. The candidate jet with the highest transverse energy has its final jet parameters calculated, and all cells belonging to this jet are 'locked' to indicate they have been used. For each remaining candidate jet, taking highest transverse energy first, the transverse energy is recalculated taking account of 'locked' cells. If its transverse energy still exceeds $E_{t\ min}^{jet}$, the parameters η^{jet}, ϕ^{jet} and E_t^{jet} are calculated, stored and cells locked as before, otherwise it is rejected.

5.2   Jet Reconstruction

For this analysis the QJCONE algorithm was used with the following parameters which are based on those used in [11, 39]:

- $E_{t\ min}^{jet}$=6.0 GeV

- $E_{t\ ini}^{jet}$=0.2 GeV

- $-3.0 < \eta < 3.0 \ (0 < \phi \leq 2\pi)$

- N_ϕ^{cell}=30 and N_η^{cell}=30

5.3   Correlation of Jet and Parton Kinematics

In the case of leading order scattering processes, only two jets per event are produced. For Monte Carlo events it is therefore trivial to associate each jet with its

corresponding parton. The situation is no longer so clear cut when initial and final state radiation are added to the picture, together with the possibility of multiple hard scatters in one event. With these effects it is possible to have more than two jets found in a single event giving rise to ambiguity when trying to associate jets to partons.

To overcome this, if more than two jets are found in an event, only the two jets leading in E_t are taken, and are considered to be the jets resulting from the primary partonic scattering. The remaining jets are attributed to either QCD radiation or jets from additional scattering processes.

The two leading jets are associated with their parent partons by selecting the pairing in which the sum of the distances between the parton-jet pairs in $\eta - \phi$ space is smallest (see figure 5.1):

$$d_{1A} + d_{2B} < d_{1B} + d_{2A} \Rightarrow Parton\ A \rightarrow Jet\ 1,\ Parton\ B \rightarrow Jet\ 2 \qquad (5.3)$$

$$d_{1A} + d_{2B} > d_{1B} + d_{2A} \Rightarrow Parton\ A \rightarrow Jet\ 2,\ Parton\ B \rightarrow Jet\ 1 \qquad (5.4)$$

Figure 5.2 shows distributions of the resolutions of the scattered parton variables as reconstructed from jets for PYTHIA SI and PYTHIA MI. In events with multiple interactions present the resolutions achieved for the jet parameters are degraded slightly and the mean of the reconstructed parton energy is increased by $\sim 1.5\,\mathrm{GeV}$. Since both PYTHIA SI and PYTHIA MI include initial and final state radiation, this energy difference is attributed to the extra energy from multiple interactions. The $\Delta\eta$ and $\Delta\phi$ distributions have large tails which are caused by the incorrect association of a jet with a parton. This can be caused when a parton scatters forward, outside of the η range considered by the jet finding algorithm, and a jet caused by QCD radiation is found instead, or in the case of MI a secondary hard scattering can take place and produce jets which are subsequently used in error.
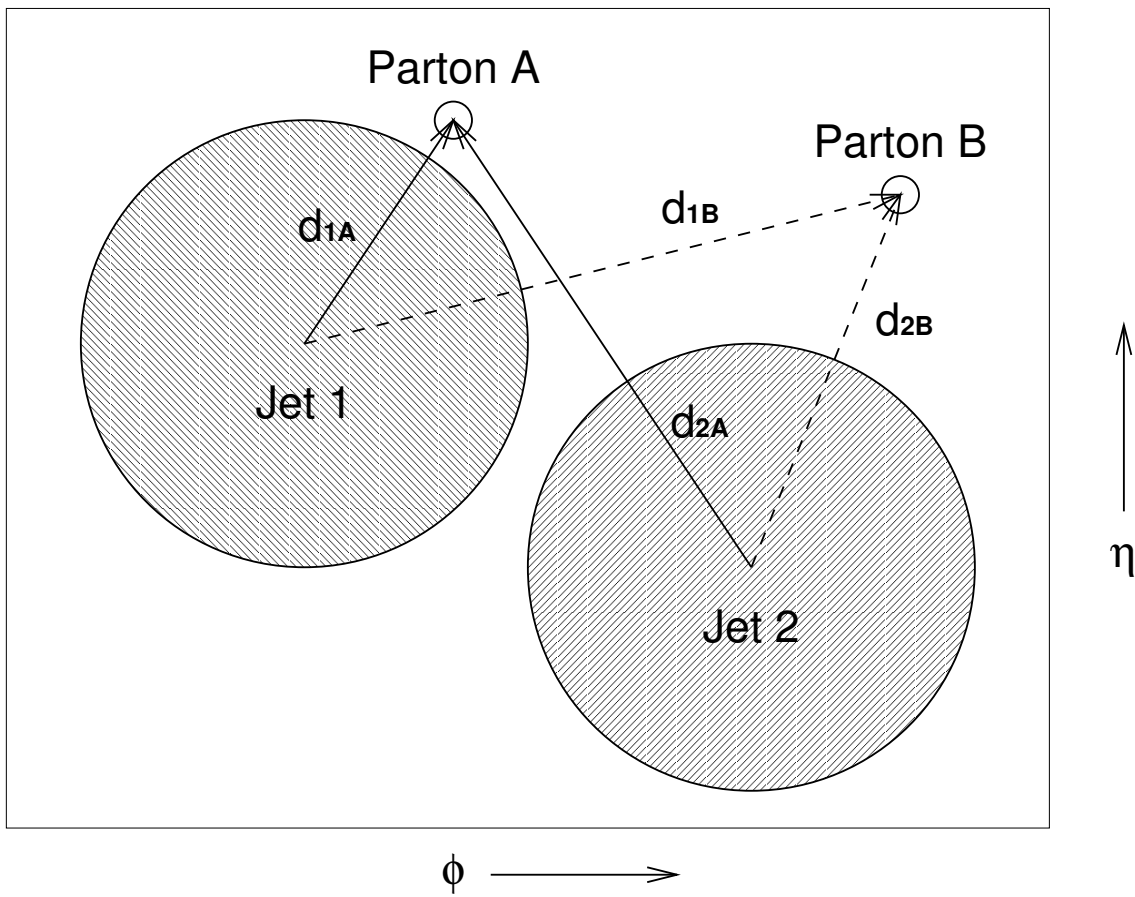
Figure 5.1: Matching of jets to partons by minimisation of distance in $\eta-\phi$ space.
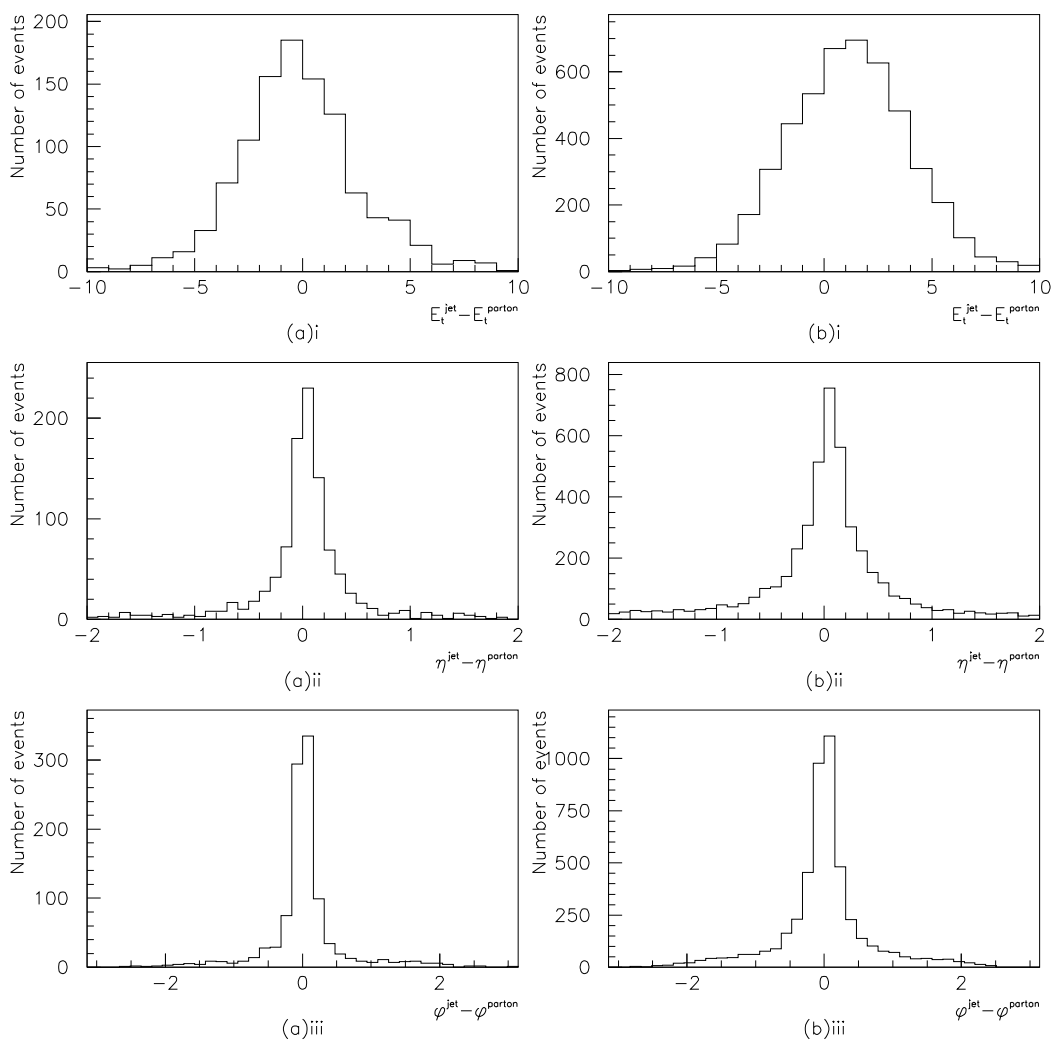
Figure 5.2: Resolutions of (i) E_t, (ii) η and (iii) ϕ of partons reconstructed from jets. Column (a) shows PYTHIA SI and column (b) PYTHIA MI.

5.4   Reconstruction of $\boldsymbol{x_\gamma}$

With the reconstructed jet parameters x_γ^{rec} can be calculated using equations 2.3 or 2.4, where the jet parameters are used as an estimate of the underlying parton dynamics. Both were used and their resolutions compared. The former expression was chosen due to its fractionally better resolution. The resolution of x_γ^{rec} was calculated by applying the jet finding algorithm to the stable generator level (GTR) particles, and calculating x_γ^{sim} in exactly the same way as x_γ^{rec}. The resolution of x_γ^{rec} for various ranges of x_γ^{sim} is shown in figure 5.4. The resolution varies from 10% to 30% with increasing x_γ^{rec}.

To give some idea of the discriminating power of x_γ^{rec} figure 5.3 shows the x_γ^{rec} distributions of a sample of direct events and resolved events. It can be seen that direct events are not generally reconstructed with $x_\gamma = 1.0$ but rather at ~ 0.8.
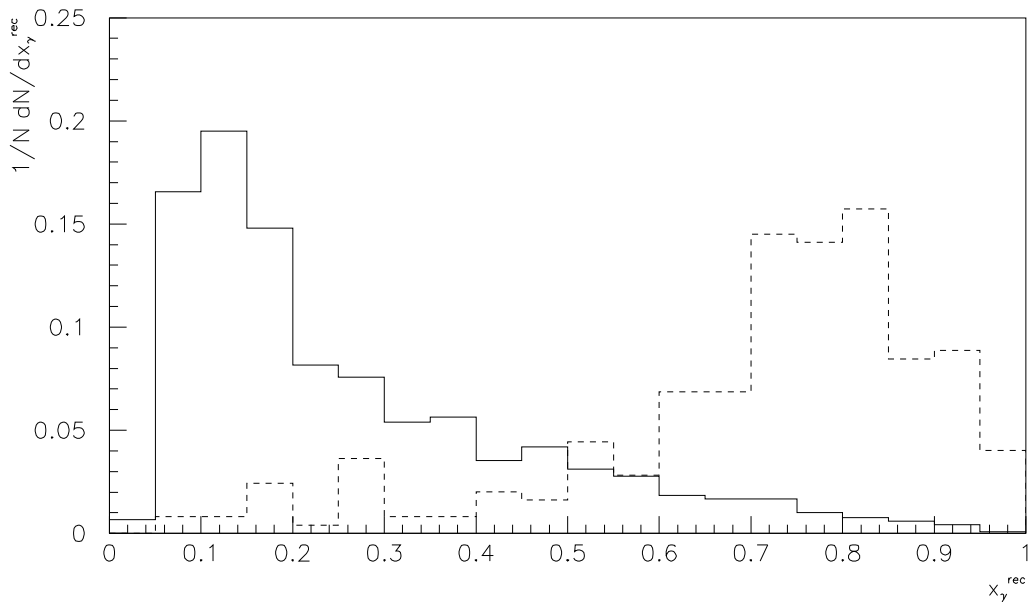
Figure 5.3: Distribution of x_γ^{rec} for resolved (solid) and direct (dashed) events.
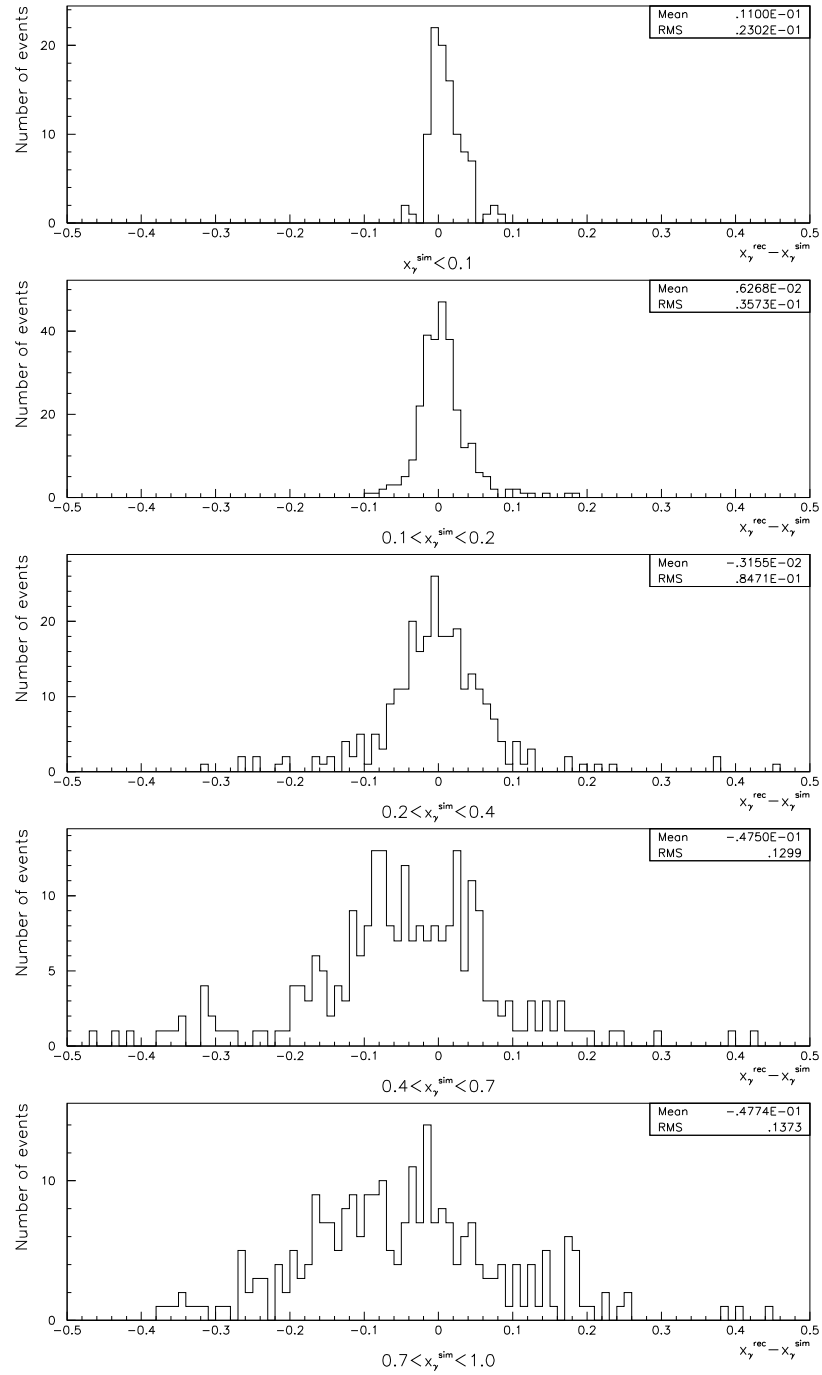
Figure 5.4: The resolutions of x_γ^{rec} for ranges of x_γ^{sim}.

Chapter 6

Forward Tracker Simulation and Reconstruction

The Forward Tracking Detector (FTD) provides an important tool for analysing energy flow in photoproduction because its acceptance of between $5°$ and $25°$ ($1.5 < \eta < 3.0$) in the laboratory corresponds to approximately $-0.5 < \eta^* < 1.0$ in the γp centre of mass frame, the γp rest frame being boosted by approximately two units in pseudo-rapidity in the forward direction. This is the region in which additional beam remnant interaction is expected to contribute to the energy flow of the event and is where an excess of energy in data has been observed in calorimetric measurements [11, 40, 41].

The environment in which the FTD operates is considerably harsher than that of the CTD for several reasons. Firstly, there is a substantial amount of dead material in between the CTD and the FTD in which secondary interactions and multiple scattering may take place. A similar problem exists due to interactions of low angle particles with the beam pipe. Conditions are further complicated by a collimator (C3) which lies around the beam pipe, underneath the rear supermodule which causes particles from secondary interactions to be scattered outwards into the tracking chambers (see figure 6.1). When operating in such conditions, it is

estimated that only approximately 40% [42] of tracks reconstructed in the FTD originate directly from the interaction point.

In this chapter, an overview of forward track reconstruction is given, followed by a detailed analysis of tracks with the aim of providing a set of criteria for selecting tracks originating from the primary vertex which is used in the energy flow analysis presented in chapter 7.

6.1 Forward Tracker Reconstruction

Track reconstruction is divided into two distinct stages; track segment reconstruction in individual planar and radial modules; and track segment linking between modules to produce complete final tracks. The initial stage of track reconstruction is performed separately for radial and planar chambers because the different chamber geometries demand the use of totally independent reconstruction techniques. (The geometrical design of the FTD is described in section 3.4.2). Here follows a brief description of the reconstruction methods employed for forward tracks. For a detailed description see [42].

6.1.1 Radial Chamber Reconstruction

Digitisations from the chambers are first subjected to a Qt algorithm which performs a 'hit search' on the data from which a charge (Q) and drift time (t) are calculated for each hit found. This is somewhat complicated by the fact that wires in each drift cell are connected to another wedge separated by 105° in ϕ, giving a double ended readout for each connected wire-pair. A mean drift time is calculated from a charge weighted mean of the two measured drift times. An approximate radial coordinate (z along the sense wire) can be calculated by charge division. From the drift time the perpendicular distance between the sense wire and track (d) can be calculated from knowledge of the drift velocity in the wedge.
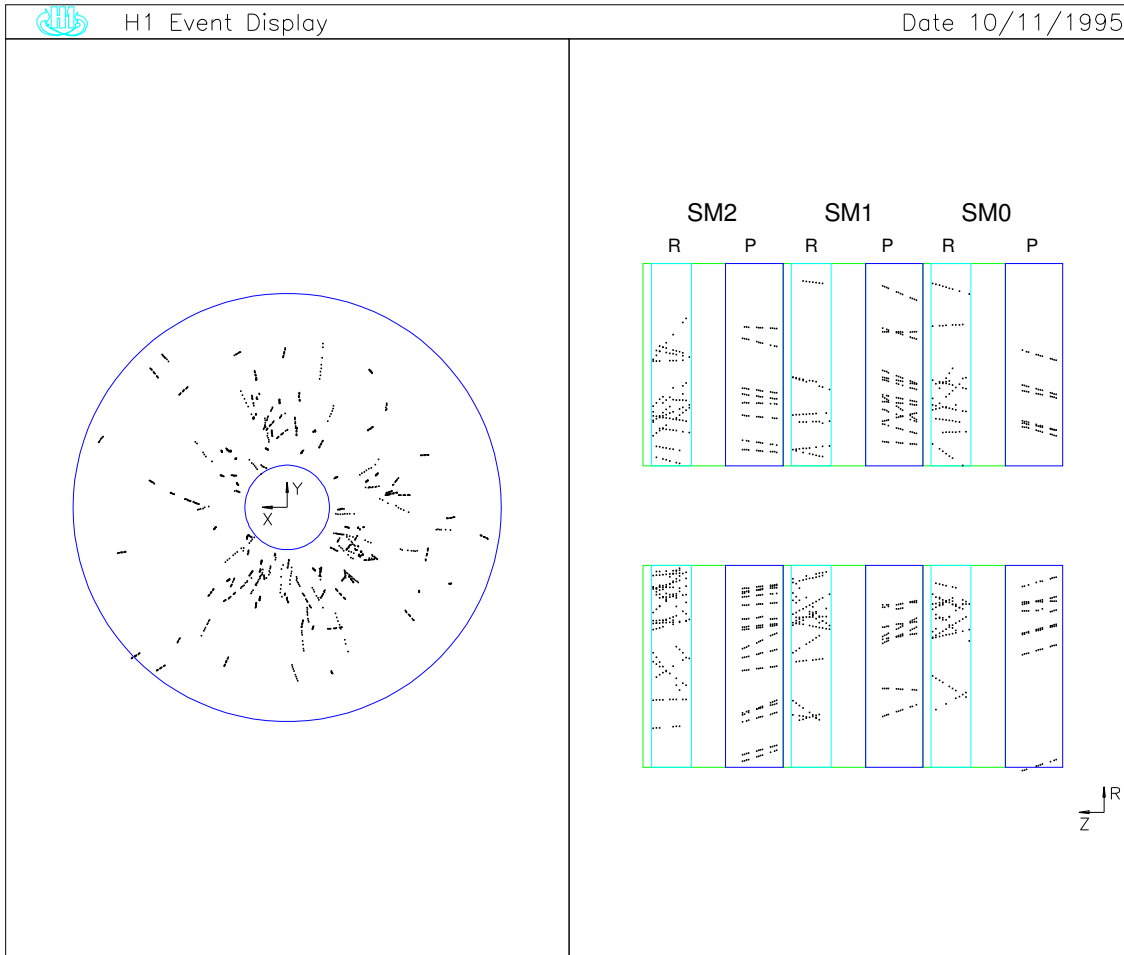
Figure 6.1: A typical high multiplicity event as seen by the FTD. The event has over 100 reconstructed tracks, demonstrating the hostile environment in which the FTD must successfully operate. Note the large number of high angle tracks, particularly in the radial chamber of the left supermodule (SM2).

Reconstruction within a wedge then proceeds as follows. Hits from three consecutive wires are used to form a hit 'triplet' such that

$$\left| \frac{1}{2}(d_1 + d_3) - d_2 \right| < P \tag{6.1}$$

where d_n is the signed drift time of the three hits, and P is approximately $1\,\text{mm}$. This mostly resolves the left-right ambiguity of the triplet. All triplets which share common hits with the same drift sign are joined if the start and end hits of the resultant group satisfies a straight line fit constraint. Triplets are also grouped if they are separated by a single hit and they satisfy this straight line criterion. All associated triplets are now fitted to a straight line and the parameters are used to project in $\phi - z$ to try to associate any odd single hits left over.

The set of all possible potential line segments should have now been constructed, but each hit is not necessarily uniquely used in one particular line segment. This unique mapping is performed by an iterative procedure which selects the 'best' line segment by virtue of total number of hits. If two potential line segments have the same number of hits, arbitration if performed using a χ^2 fit to a straight line in $\phi - z$. When the best line segment has been selected its hits are tagged as used and the remaining hits left in the wedge are then re-examined. Of course in practise tracks are not constrained to lie in a single wedge so partial line segments are projected in $r - \phi$ into adjacent wedges to pickup hits or hit groups.

6.1.2 Planar Chamber Reconstruction

The sense wires are read out and digitised and a Qt algorithm applied in exactly the same way as for the radial chambers, except the planar chambers sense wires are only read out from a single end. This means that no z information about hits is available.

The reconstruction process is divided into two stages, the first being the assembly of hits in each individual XUV layer into clusters[1], followed by the combining of clusters into potential planar segments. Each cluster defines a plane running parallel to the sense wires of its orientation. A planar segment is then defined by the intersection of three such planes within measurement resolutions.

The search for clusters proceeds as follows. Each XUV layer should give four drift distances (hits) from its four sense wires. Every combination of hits from the two outer wires, which define a line whose angle is approximately consistent with originating from the vertex, is sought. Instances where hits on the inner two wires fit this line defined by the outer wires hits within some tolerance are kept. These clusters form the set of all potential clusters, which will contain some percentage of false clusters due to left-right ambiguity (known as reflections) and random alignments. Hits at this stage do not necessarily belong to a single cluster. Unwanted false clusters are removed using an iterative process which rejects the cluster which shares hits with the largest number of other clusters until each cluster remaining shares hits with a maximum of two other clusters. The remaining clusters must either do not share hits, or share hits with one or two other clusters. To remove these last ambiguities, each cluster fitted to a straight line and the worst fitting removed, until all remaining clusters do not share hits. This pattern recognition technique only requires a few fits to be performed thus greatly reducing the computation involved.

All hits left over from this process are subjected to the same process but with less stringent tolerances and relaxed vertex pointing requirement. Due to chamber inefficiencies, true clusters may not have four hits (chamber inefficiencies etc), so finally clusters with only three hits are searched for using tighter cuts than before, due to the greater chance of random alignment.

The next stage concerns the linking of clusters from separate XUV orientations to form potential planar segments. This is achieved by calculating the intersections of all combinations of XUV clusters, and any intersection which is

---

[1]A cluster is defined to be a group of 3 or 4 hits in a single XUV plane.

within a specified tolerance is accepted as a potential planar segment. Because of the large number of combinations of possible XUV clusters and the lack of z information, a method to remove falsely associated clusters is required. The actual method employed is similar to that described above for cluster finding. For each combination of XUV clusters the χ^2 probability for the fit to a straight line is calculated using all hits. Then each node is given a weight which is the sum of the χ^2 fit values from each potential planar segment which shares clusters. The same iterative technique as described above is then used to reject potential planar segments which share clusters with the largest number of other potential planar segments. Arbitration here is performed with the summed χ^2 weight.

6.1.3   Segment Linking Procedure

After all track segments have been reconstructed in each individual radial or planar module they must then be linked across the three supermodules to form complete tracks. Planar segments are first linked together to form potential tracks. Next, radial segments are linked to the planar only tracks. Lastly, a set of tracks is constructed by linking radial segments together and then linking these to planar segments. These two sets of tracks are then combined and the the best tracks selected. This is necessary because neither order of linking finds all tracks which should be linked due to the limited resolution of the detectors.

The linking of planar segments is performed in an order dictated by the hierarchy of track measurement resolution, to prevent wrongly linked tracks:

- Three planar segment tracks

- Adjacent module two planar segment tracks

- Non-adjacent two module planar segment tracks

Each pair of planar segments is projected to the midpoint between them and the radial distance (D) transverse to the z axis is calculated using

$$D = \sqrt{(x_1^{mid} - x_2^{mid})^2 + (y_1^{mid} - y_2^{mid})^2} < D_{max} \qquad (6.2)$$

If D is less than D_{max} ($\sim 7\,\text{mm}$) then a χ^2 fit to an appropriate track model is performed to reject bad tracks and resolve ambiguities (see [42] for details of track models).

A similar approach is used to link together radial segments, using a different track model to allow to for the low resolution of their radial coordinate. There now exists two sets of independently linked tracks from which unique set of tracks is chosen based on a χ^2 fit. Single planar and radial segments which are left from the linking process are used to try to produce linked planar-radial pairs. The remaining single planar segments are kept. For 1993 data, single radial segments were considered to be too unreliable to use in analysis due to the poor definition in $r-z$, which makes them difficult to associate with the vertex.

In the final stage of the reconstruction the linked tracks are passed through a Kalman filter which determines the optimum track parameters. This process takes into account effects of multiple coulomb scattering.

6.2   Comparison of Monte Carlo with Data

6.2.1   Dead and Inefficient Cells

Due to the nature of the construction of the planar chambers the geometrical areas occupied by dead and inefficient cells do not map easily from the detector geometry (XUV orientations) into track $\theta - \phi$ space. For this reason dead and inefficient cells of both planar and radial modules have been identified by inspection of data hit maps (see figures 6.2 and 6.3). Some of the dead cells found in data have not been included in the Monte Carlo simulation, so tracks are excluded from analysis

SM0	Planar	X25, X26, U21
	Radial	7, 21
SM1	Planar	V3, V10, V16
	Radial	6, 7, 10, 11, 20, 21, 24, 25, 28, 29, 30, 31
SM2	Planar	
	Radial	11, 25, 36

Table 6.1: Dead and inefficient planar and radial cells of the FTD in 1993.

if they extrapolate through deficient planar cells. A list of dead and inefficient cells is shown in table 6.1.

6.2.2 Planar & Radial Chamber Performance

To compare the relative performance of the FTD for data and Monte Carlo, a method was devised which uses the intrinsic redundancy within the FTD. The FTD is constructed from six independent layers through which a track may pass. To calculate the efficiency of of any particular layer it is necessary to look for a track before and after it has passed through the layer of interest by looking for reconstructed tracks which have a segment in both these sandwiching layers, in effect 'pinning down' where the track should be. The efficiency is then given by the ratio of the number of tracks which have all three segments present divided by the total number of tracks which have the two 'pinning' segments present. This calculated efficiency is a combination of segment reconstruction efficiency and segment linking efficiency, which is expected to vary according to the number of tracks passing through the FTD due to the increasing complex reconstruction task. Obviously this approach does not work for planar module 0 (P0) or radial module 2 (R2), but it was found that imposing a radial constraint in conjunction with two linked segments either before the module in question (in the case of radial module 2) or after the module (planar module 0) was a sufficient constraint. This radial constraint is
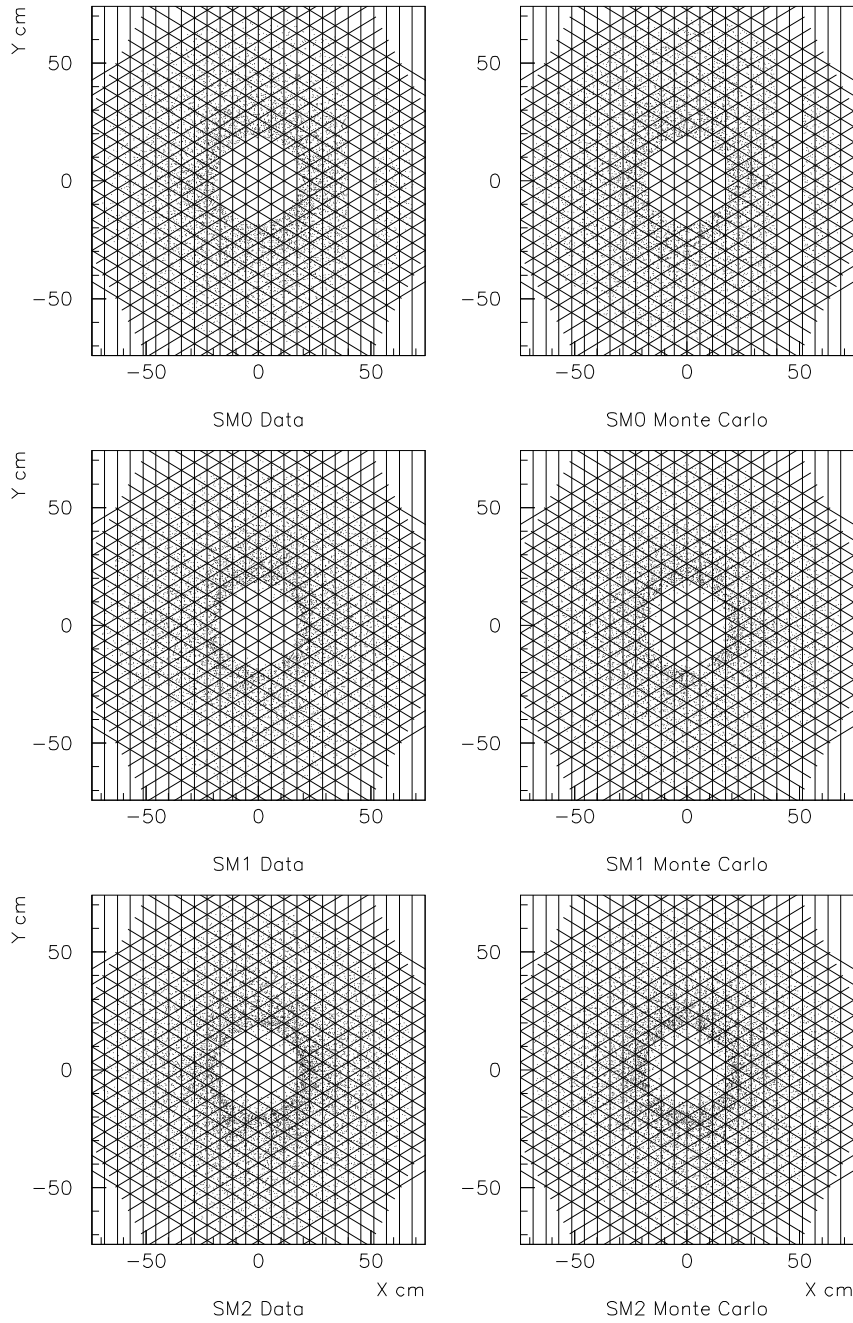
Figure 6.2: Dead and inefficient areas of the planar chambers in 1993.
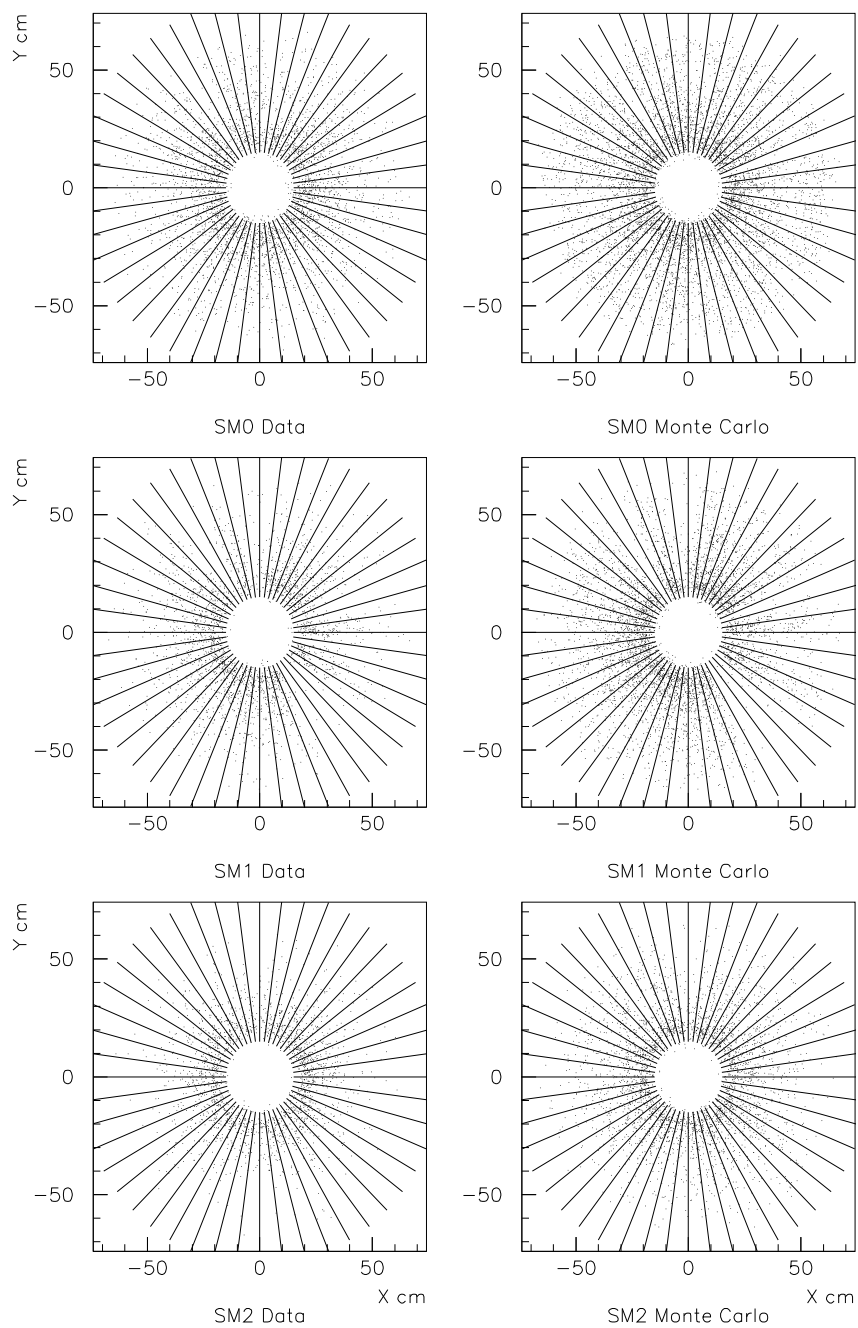
Figure 6.3: Dead and inefficient areas of the radial chambers in 1993.

SM0	Planar	R0+P1	$20 < r < 45\,\mathrm{cm}$
	Radial	P0+P1	
SM1	Planar	P0+R1	$25 < r < 55\,\mathrm{cm}$
	Radial	P1+P2	
SM2	Planar	P1+R2	$30 < r < 60\,\mathrm{cm}$
	Radial	P1+P2	

Table 6.2: Constraints used to 'pin' tracks in different modules.

required because the modules acceptances for tracks originating from the interaction point varies with z. A list of the constraints used is shown in table 6.2.2.

This method of comparison was applied to the final 2-jet event selection described in chapter 4. A momentum cut of $1\,\mathrm{GeV}$ was applied to reconstructed tracks to help remove multiple scattering effects. The Monte Carlo used was PYTHIA MI.

Figure 6.4 shows average module efficiency as a function of N_{rec}, the total number of tracks reconstructed in the FTD, for each module. Clearly there is a strong dependence on N_{rec} which is understood in terms of the decrease in the quality of the reconstructed segments as the the number of tracks traversing the FTD increases. As N_{rec} increases, the linking efficiency decreases due to either segments failing to be reconstructed or segments being incorrectly reconstructed and failing to link due to incorrect or poor directional information.

The radial modules efficiency is well described by the Monte Carlo, however the planar module efficiency is systematically above that of Monte Carlo for SM0. This discrepancy is thought to be an artifact of the Monte Carlo tuning procedure [43].
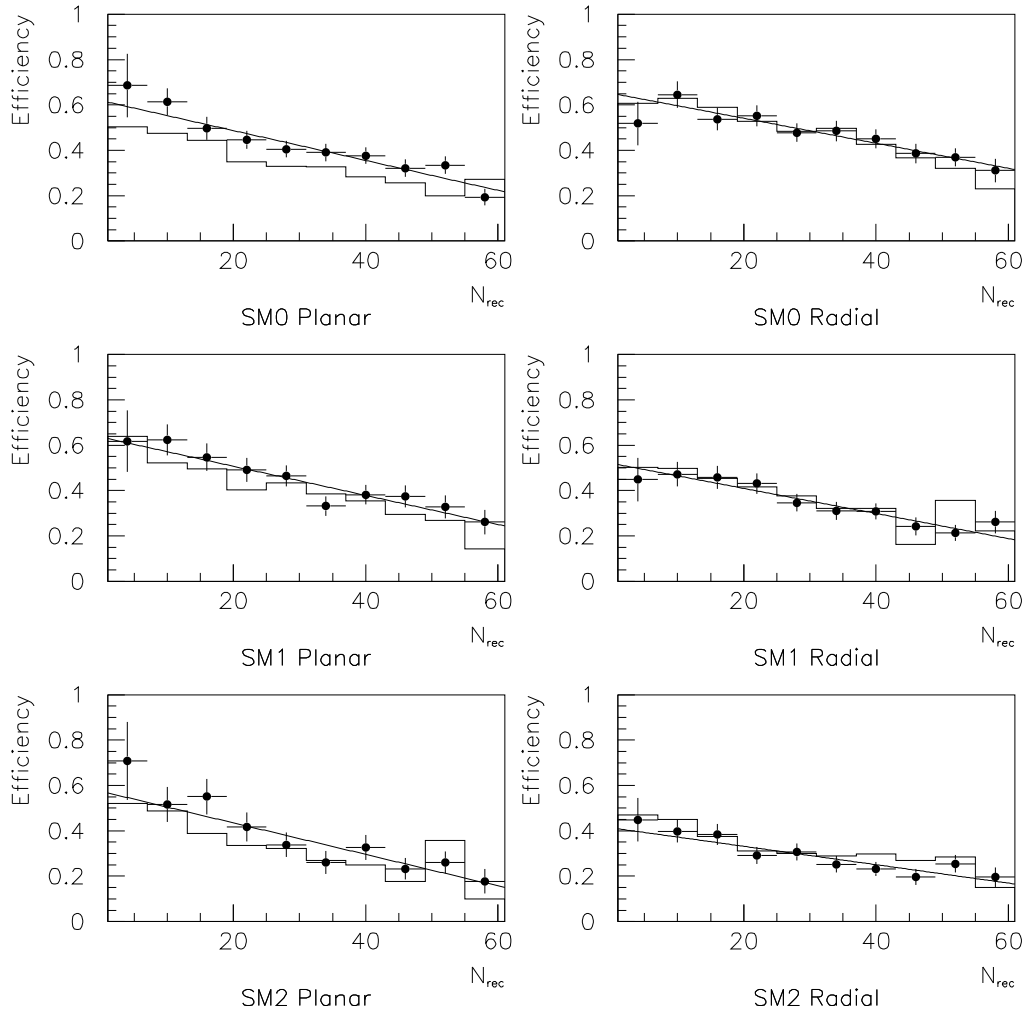
Figure 6.4: Comparison of planar segment reconstruction and linking efficiency. Data (Monte Carlo) circles (histogram). Data points fitted to straight lines.

6.3   Monte Carlo Track Matching

In order to calculate the efficiency of reconstructing a track in the tracker, is necessary to be able to associate a reconstructed track with its parent Monte Carlo track. To do this, detailed knowledge of the origin of the hits used to build a reconstructed track is required. This information is available at the Monte Carlo simulated level, and this enables the way in which hits are being used to form tracks to be studied in detail.

At the simulated Monte Carlo level (STR level) a single hit can be associated with the simulated track which caused it. With this information the reconstructed tracks can be related back to the simulated tracks. Since the relationship between simulated tracks and reconstructed tracks is not necessarily 1:1 (for instance, a simulated track may be reconstructed as two track segments because linking has failed) some method of finding the 'best' reconstructed track which can be associated back to the simulated track is required.

Track matching is performed using the two variables defined by 6.3 and 6.4 to decide which reconstructed track best matches a simulated track. These two variables only make use of hits, and no spatial constraints are used.

$$R_1 = \frac{Number\ of\ common\ planar\ hits}{Total\ number\ of\ simulated\ planar\ hits} \qquad (6.3)$$

$$R_2 = \frac{Number\ of\ common\ planar\ hits}{Total\ number\ of\ reconstructed\ planar\ hits} \qquad (6.4)$$

The variable R_1 is a measure of fraction of the total number of hits caused by a simulated track, which have been used to make a reconstructed track. Variable R_2 is a measure of the purity of the hits with respect to a particular simulated track, used to make a reconstructed track. Starting with two sets of tracks, one of simulated tracks and the other of reconstructed tracks, matching is performed by iteratively searching for the simulated and reconstructed track pair which has the highest values of R_1 and R_2. This pair of tracks is then marked as 'matched' and removed from

the sets of candidate tracks. This process is repeated exhaustively until none of the remaining simulated and reconstructed tracks are related. It is possible for both simulated tracks and reconstructed tracks to remain unmatched. Unmatched simulated tracks are referred to as 'ghost tracks'. Unmatched reconstructed tracks are a result of a simulated track being reconstructed as two separate track segments. If a simulated track is related to two reconstructed track segments this procedure should reject the 'worst' reconstructed track segment, matching the simulated track with the 'better' remaining track segment. It is hoped that the 'worst' piece of track will be rejected by track selection cuts and the problem of double counting split tracks avoided.

6.3.1   Track Selection Criteria

The objective is to select tracks which are well reconstructed and originate from the primary vertex (ie primary tracks) by tuning cuts based on the available track parameters to obtain the highest efficiency for primary tracks and the lowest contamination from tracks which have originated from secondary interactions. The selection process can be divided into two stages. The first stage is to identify regions of good acceptance and to select well reconstructed tracks. The second is to select tracks originating from the primary vertex. For the purposes of this selection process, tracks are subdivided into three classes as follows

- All reconstructed tracks, ie with one, two and three planar segments

- Reconstructed tracks with only one planar segment

- Reconstructed tracks with at least two planar segments

This division of tracks based upon the number of planar segments is made because it is known that tracks with only one planar segment can be poorly constrained in momentum due to insufficiently accurate measurement of their curvature.

This being the case, any other variables which involve the extrapolation of a track will thus also be affected. Keeping all tracks together would obscure these different track properties.

In the following sections, efficiency is defined as 'the distribution of a variable calculated from selected simulated tracks with matched reconstructed tracks passing selection cuts, divided by the same type of distribution calculated from selected simulated tracks only'. Purity is defined as 'the distribution of a variable calculated from selected reconstructed tracks matched to selected simulated tracks, divided by the same type of distribution calculated from reconstructed selected tracks only'. Contamination is defined as one minus purity.

6.3.2   Track Acceptance and Quality

The first cut imposed on tracks is an acceptance cut in pseudo-rapidity η. The reconstruction efficiency of primary tracks as a function of η is shown in figure 6.5(a). No other cuts are applied to the reconstructed tracks. Below $\eta = 1.75$ the efficiency falls rapidly due to falling detector acceptance. Above $\eta = 2.75$ the efficiency again starts to fall off, albeit more slowly. Between these two limits an average efficiency of approximately 80% is achieved for all tracks, two thirds from one planar segment tracks and one third from two or more planar segment tracks. The acceptance of two or more planar segment tracks is slightly reduced compared to that for tracks with only one planar segment. Figures 6.5(b) and (c) show the number of 'ghost' tracks and the fraction of unmatched reconstructed tracks respectively. The number of ghost tracks increases at both low η and high η due to detector inefficiencies and acceptance edge effects as tracks begin to graze the edges of the active detector volume. The number of unmatched reconstructed tracks follows a less pronounced but similar trend, suggesting that the quality of tracks is poorer at the edge of the detectors acceptance affecting their subsequent linking. The slight rise in the number of unmatched reconstructed tracks in the region of central η is

probably due to a systematic decrease in linking efficiency with the inclination of the track. From these three distributions a suitable cut in η for reconstructed tracks is chosen to be $1.75 < \eta < 2.75$ as indicated by the shaded areas.

Particles of low momentum (hundreds of MeV) typically undergo some form of interaction with dead material both on route to the FTD and also inside the FTD between supermodules. Therefore a cut in momentum is important because of this source of contamination arising from these secondary interactions. Figure 6.6(a) shows the momentum distributions for the three classes of tracks. The efficiency and contamination of primary tracks as a function of momentum p after applying an η cut of $1.75 < \eta < 2.75$ to reconstructed tracks is shown in figure 6.6(b) and (c) respectively. Both one planar segment tracks and tracks with two or more planar segments exhibit fairly constant efficiencies above $1\,\text{GeV}$. There is a steep fall off in efficiency below $1\,\text{GeV}$ as expected. The average efficiency for all tracks with momentum greater that $1\,\text{GeV}$ is approximately 70%. This is 10% lower than shown in figure 6.5(a) due to the η constraint imposed on reconstructed tracks. Tracks with at least two planar segments do not show this decrease, suggesting that some single planar segment tracks are reconstructed in the wrong location. The contamination is high for tracks below $1\,\text{GeV}$ as expected and has an average value of approximately 50% above this momentum. A momentum cut of $1\,\text{GeV}$ is chosen above which efficiency and contamination are approximately constant. Only 75% of reconstructed tracks survive this cut.

The 'quality' of the measurement of a track depends on many things, such as the hits' pulse size or number of hits nearby. To estimate how well a track has been measured, a χ^2 probability of a fit to an appropriate track model is calculated and this provides a method to discriminate between well measured tracks and tracks containing enough badly measured hits to make their measured parameters unreliable.

From the track matching process the hit purity R_2 of each matched reconstructed track is available. By studying R_2 and efficiency as a function of χ^2_{trk}/ndf

Figure 6.5: (a) Reconstruction efficiency. Solid histogram all tracks, dashed histogram tracks with one planar segment only and dotted histogram tracks with at least two planar segments. (b) Simulated ghost tracks. (c) The fraction of reconstructed unmatched tracks.

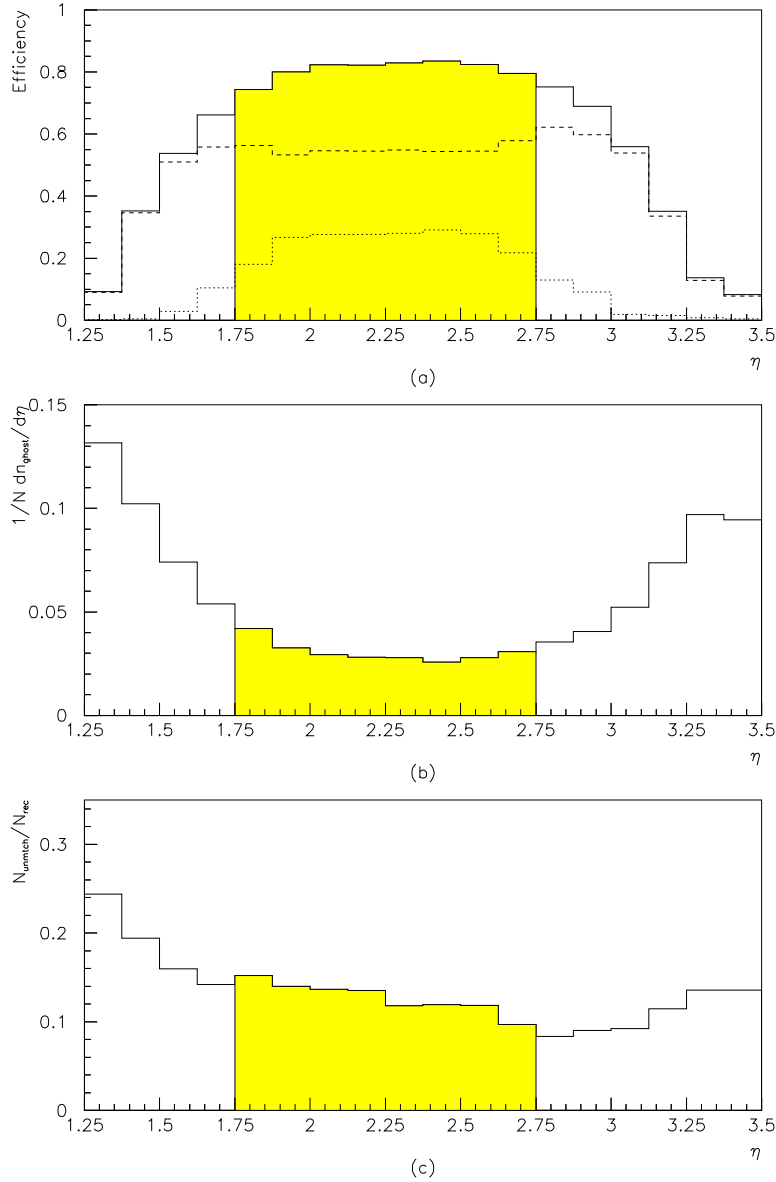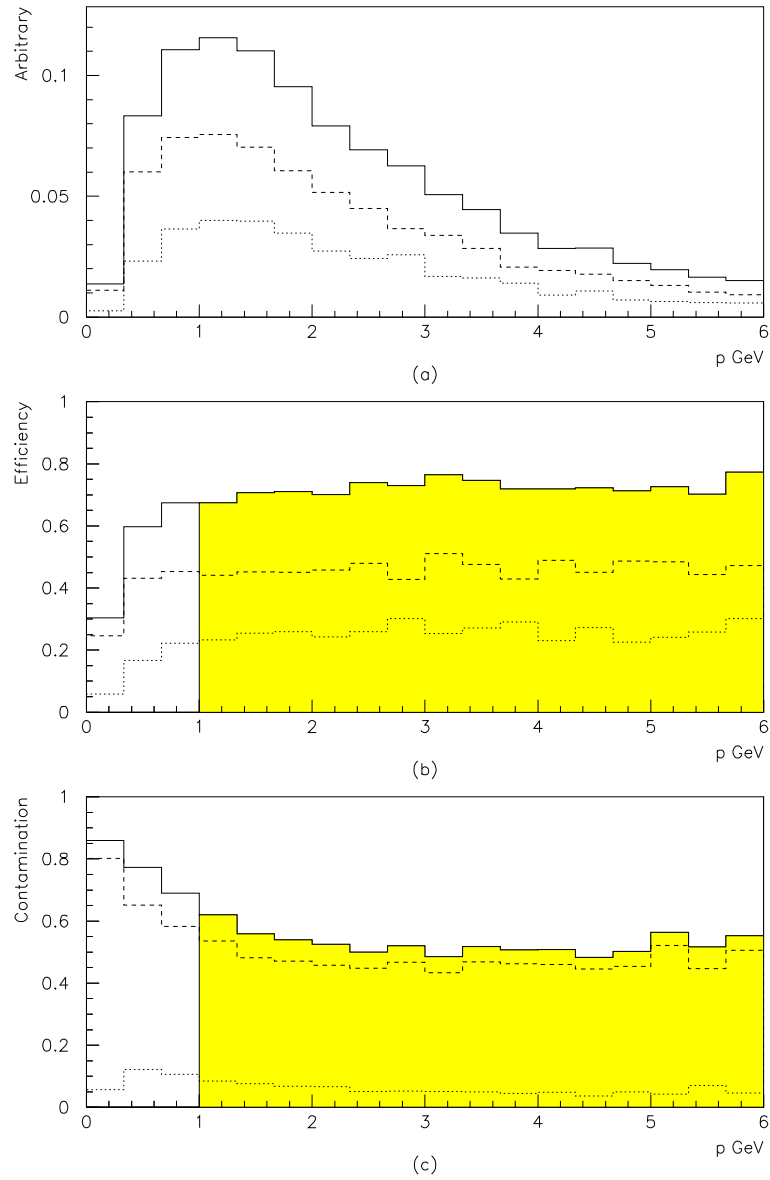Figure 6.6: (a) Distribution of reconstructed track momentum. (b) Reconstruction efficiency and (c) contamination of reconstructed tracks as a function of momentum p. Solid histogram all tracks, dashed histogram tracks with one planar segment only and dotted histogram tracks with at least two planar segments.

it is possible to assess the effect of a cut in χ^2_{trk}/ndf has on the hits used to build reconstructed tracks. Figure 6.7(b) and (c) show efficiency and mean R_2 as a function of χ^2_{trk}/ndf. The efficiency for (b) was calculated by calculating the efficiency for primary tracks as a function of momentum, using the previously defined η and p cuts, along with the appropriate χ^2_{trk}/ndf cut and taking the mean efficiency of this distribution.

It is interesting to note that tracks with two or more planar segment have a hit purity exceeding 80% compared to tracks with only one planar segment which have an average value of around 66%, and this decreases as χ^2_{trk}/ndf tends to small values as opposed to tracks with two or more planar segments. There is no obvious advantage in making a strong cut in χ^2_{trk}/ndf, so a very conservative cut of χ^2_{trk}/ndf <30 has been chosen just to remove tracks from the extreme tail of the χ^2_{trk}/ndf distribution. Tracks with two or more planar segments exhibit a fatter tail in χ^2_{trk}/ndf than tracks with only one planar segment. This is probably due to multiple scattering effects between supermodules and wrongly linked tracks.

The final track quality cut required for any track selection which is to be used for measurement of energy flow is a cut in the ratio of the error in momentum of the track and its momentum (dp/p). This is required to ensure that the tracks used in analysis are of well defined momentum. From examination of the distribution of dp/p for tracks with all cuts so far defined, a cut of $dp/p < 0.3$ is chosen. This cut rejects a further 2% of tracks.

6.3.3   Selection of Primary Tracks

As mentioned before, the FTD experiences a large number of secondaries from various processes such as decays, secondary interactions, pair production and delta rays. Since the sources of these secondary particles originate from particles travelling outward from the interaction point at a low angle, it is difficult to differentiate between these secondaries and primary tracks due to the relatively poor
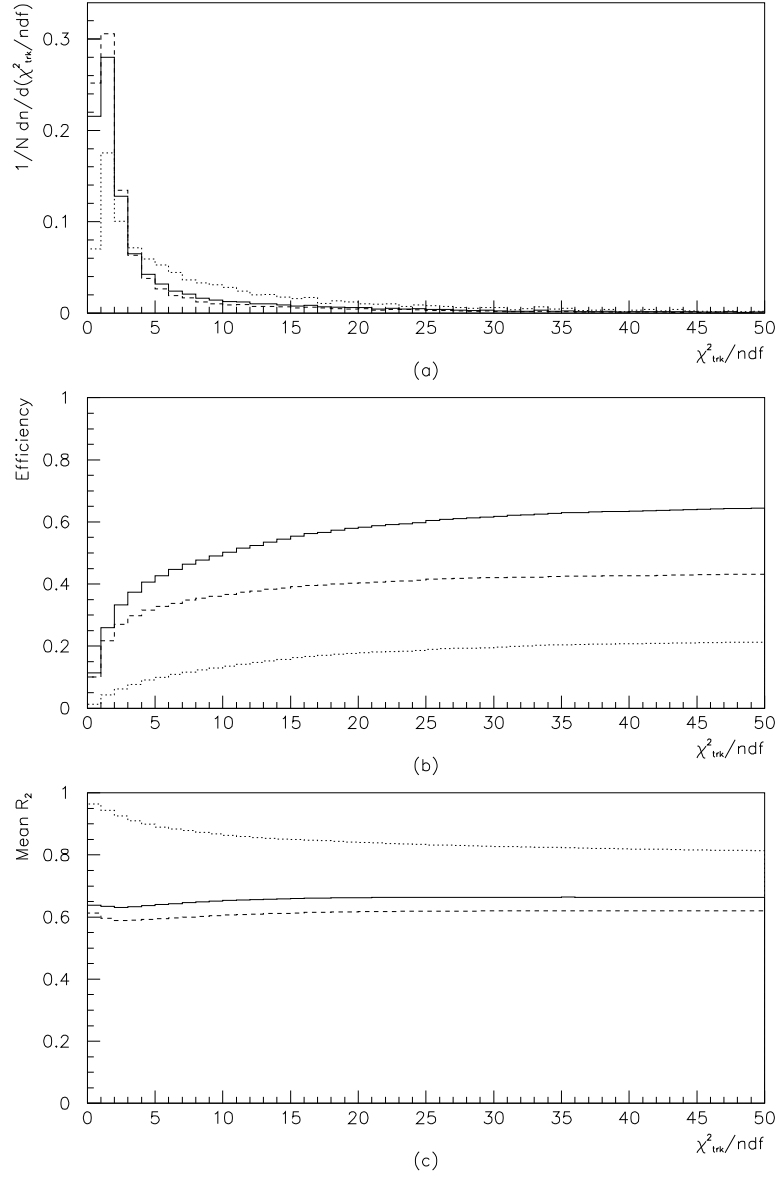
Figure 6.7: (a) Distribution of χ^2_{trk}/ndf. (b) Reconstruction efficiency and (c) mean value of hit purity R_2 as function of χ^2_{trk}/ndf cut. Solid histogram all tracks, dashed histogram tracks with one planar segment only and dotted histogram tracks with at least two planar segments.

measurement of track parameters, which reduce the accuracy of extrapolation. For example, one planar segment tracks consist of 10 to 12 space points measured over approximately 2 cm in z, at over 1.4 m away from the nominal interaction point. A one planar segment track therefore has a relatively poor resolution in theta, which strongly affects the precision of extrapolation over such large distances. Variables which allow discrimination of tracks originating from the primary vertex from tracks produced in secondary interactions are:

- χ^2_{vtx}/ndf - probability of fit to the event vertex

- R_0 - projected radial distance of track at $z = z_{vtx}$

- $z_0 - z_{vtx}$ - projected z of track at DCA minus z_{vtx}

The most powerful of these variables is χ^2_{vtx}/ndf. This value is calculated in a similar way to χ^2_{trk}/ndf, but the event vertex (which is calculated from tracks measured by the CTD) is added as an extra track space point. Tracks with large values of χ^2_{vtx}/ndf are unlikely to have originated from the event vertex. Figure 6.8(a) shows a χ^2_{vtx}/ndf distribution of all reconstructed tracks, and it exhibits a long tail. Distributions (b) and (c) show the efficiency and purity for selecting primary tracks as a function of χ^2_{vtx}/ndf respectively. Even using very severe cuts in χ^2_{vtx}/ndf a purity of only approximately 80% is achieved at the expense of a very large drop in efficiency. This indicates that a fraction of secondary tracks are indistinguishable from primary tracks as measured by the FTD. To preserve a reasonable efficiency a cut of $\chi^2_{vtx}/ndf < 15$ is chosen, giving an efficiency of 40% and a purity of 60%. Applying this vertex constraint cut reduces the efficiency by almost a factor of two, thus almost half of the detected primary tracks are poorly reconstructed and fail to point accurately back to the vertex. The sensitivity to this χ^2_{vtx}/ndf cut is estimated to be small at around this value, which is far away from the steeply falling region of efficiency.

To check if any additional discrimination is available from the remaining variables $abs(z_0 - z_{vtx})$ and R_0 is possible, the efficiency and purity as a function

of cuts on these variables were also calculated. These distributions are shown in figures 6.9 and 6.10 respectively. They indicate that no worth while improvements can be made from placing cuts on these track parameters. As a further cross check, an alternative primary track selection was developed without using the vertex constraining χ^2_{vtx}/ndf cut. This showed that it was possible to achieve similar values of efficiency and purity, but at the expense of placing cuts on steeply falling edges of distributions. Since the level of agreement of the resolution of track parameters between data and Monte Carlo is unknown, the original primary track selection based solely on χ^2_{vtx}/ndf was chosen for the final track selection.

6.3.4 Track Density Effects

As previously stated in section 6.2.2 the planar segment efficiency and particularly the linking efficiency is dependent on the number of tracks penetrating the FTD. This is, however, an over simplification of the actual situation, because these efficiencies are in fact closely related to the track topology and planar chamber geometry in a nontrivial way. This may be envisaged by considering an event in which jet passes through the FTD. The geometric area of the FTD through which the jet passes has a high track density compared to that of the rest of the FTD (which may be assumed to be relatively sparsely populated). However, due to the nature of the geometry of the FTD, areas of high track density are connected via planar chambers which extent out of this region, into areas of low track density. Thus a solitary track, geometrically well separated from the jet region can be affected at the hit level by tracks in the jet region, if it shares a common planar chamber.

For the energy flow analysis presented in chapter 7, only tracks outside of jets[2] are of interest (see chapter 7 for definition and explanation of topological areas). The efficiency and contamination as a function of χ^2_{vtx}/ndf for this subset of tracks is calculated using the final track selection. These distributions are shown in

---

[2]Outside of jets implies that a track is separated in $\eta-\phi$ space from the jet axis by a distance of more than 1.5 units.

Figure 6.8: (a) Distribution of χ^2_{vtx}/ndf. (b) Reconstruction efficiency and (c) purity of reconstructed track selection as a function of χ^2_{vtx}/ndf cut. Solid histogram all tracks, dashed histogram tracks with one planar segment only and dotted histogram tracks with at least two planar segments.
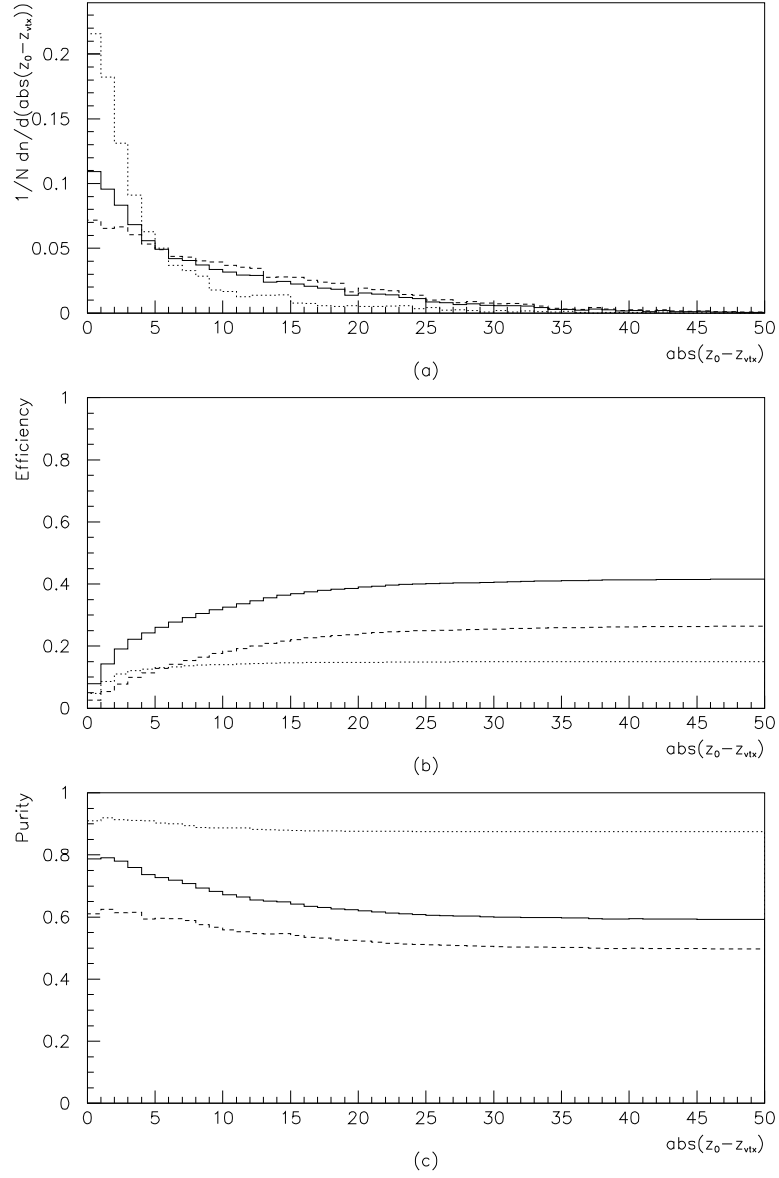
Figure 6.9: (a) Distribution of $abs(z_0 - z_{vtx})$. (b) Reconstruction efficiency and (c) purity of reconstructed track selection as a function of $abs(z_0 - z_{vtx})$ cut. Solid histogram all tracks, dashed histogram tracks with one planar segment only and dotted histogram tracks with at least two planar segments.
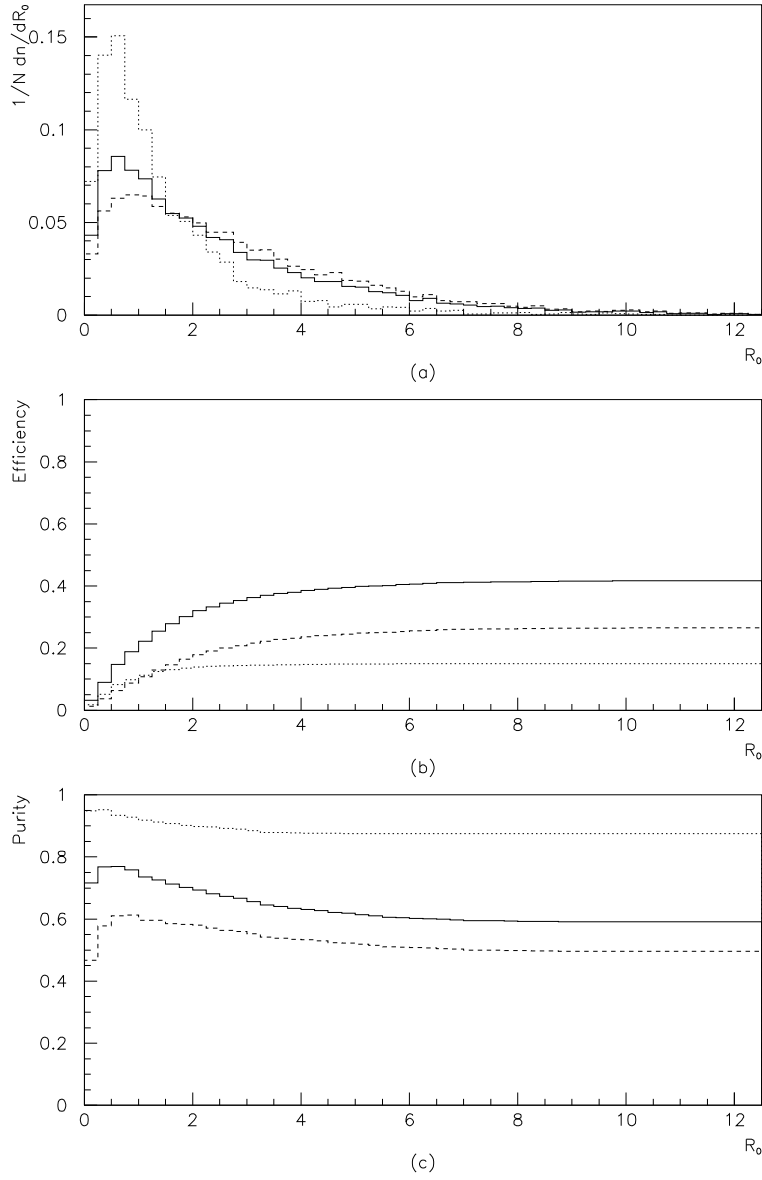
Figure 6.10: (a) Distributions of R_0. (b) Reconstruction efficiency and (c) purity of reconstructed track selection as a function of R_0 cut. Solid histogram all tracks, dashed histogram tracks with one planar segment only and dotted histogram tracks with at least two planar segments.

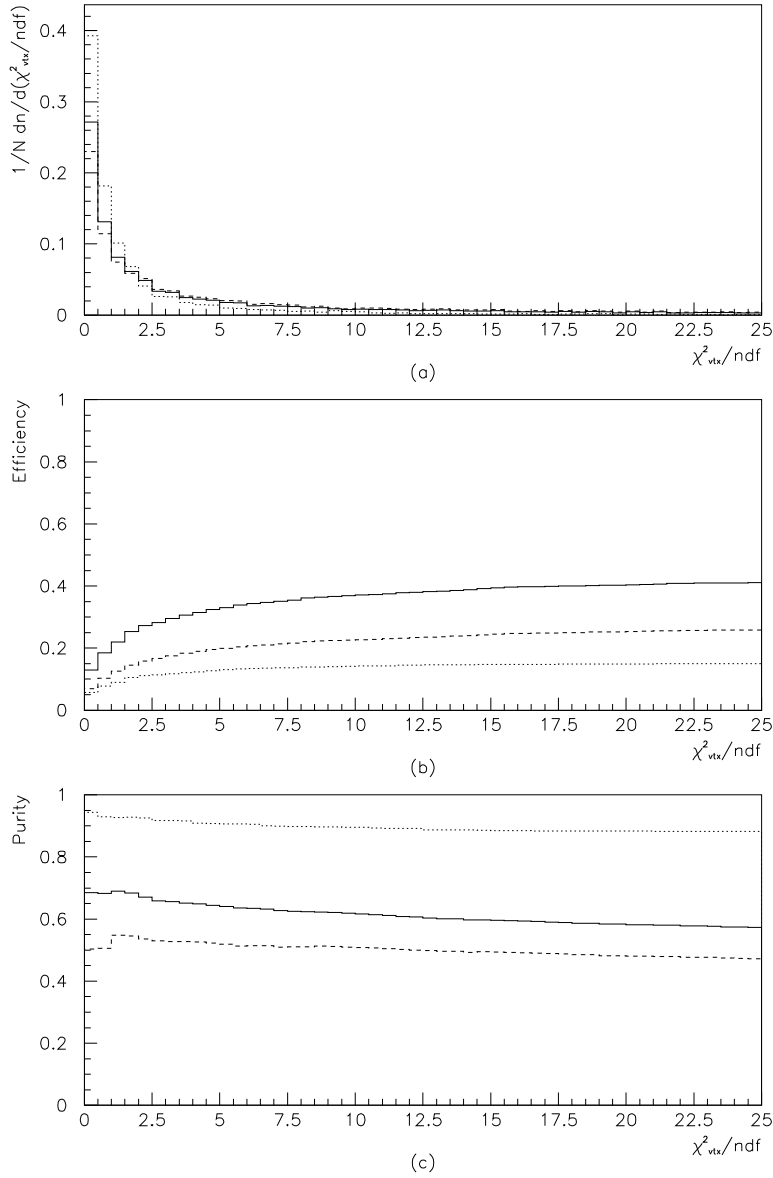Figure 6.11: The subset of tracks outside of jets ($R > 1.5$): (a) Distribution of χ^2_{vtx}/ndf. (b) Reconstruction efficiency and (c) purity of reconstructed tracks as a function of χ^2_{vtx}/ndf cut. Solid histogram all tracks, dashed histogram tracks with one planar segment only and dotted histogram with at least two planar segments.
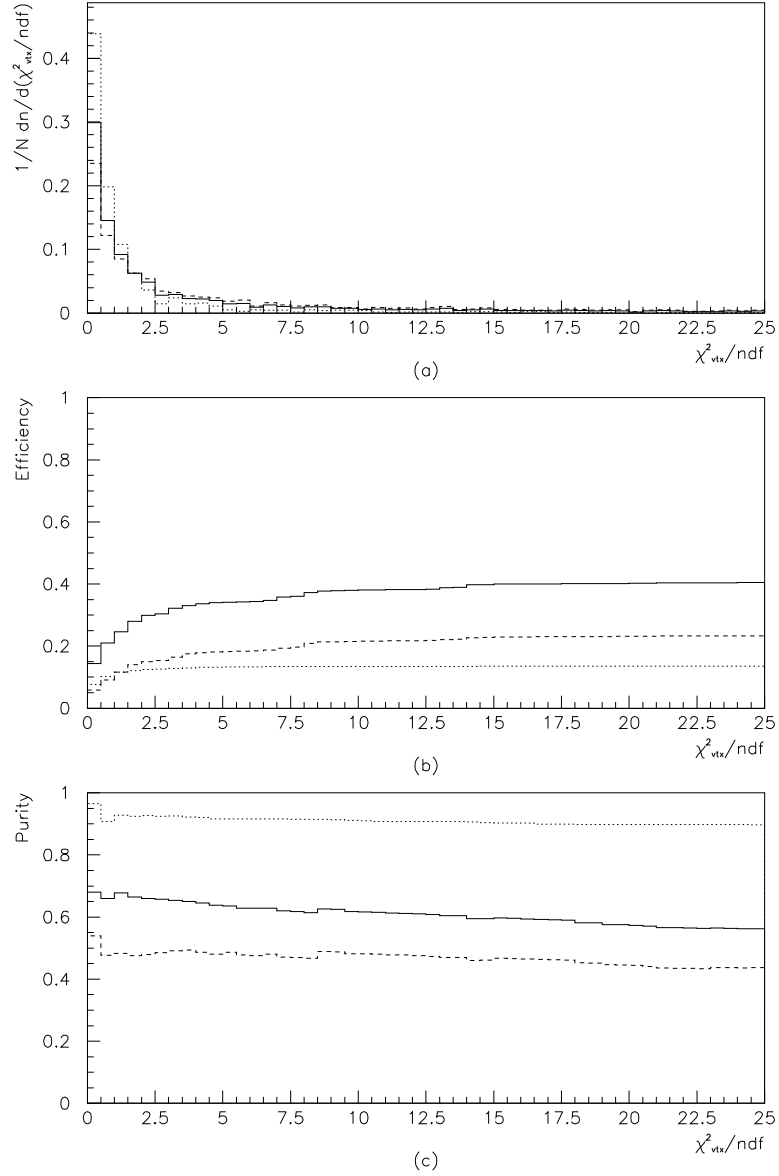
figure 6.11, and may be compared to those previously calculated for all tracks (see figure 6.8). For the final track selection the track subset has an efficiency of 41% and a purity of 60%. As expected for these high multiplicity events, little evidence is seen for differing performance of the FTD between these two sets of tracks, although the χ^2_{vtx}/ndf distributions are slightly narrower, also one planar segment track efficiency shows very slightly less dependence on χ^2_{vtx}/ndf.

6.4   Reconstruction Problems

As noted previously in section 6.3.2, one planar segment tracks sometimes appear to be incorrectly reconstructed at the wrong spatial position. This effect is shown in figure 6.7(b) where a drop in reconstruction efficiency is seen when a constraint in pseudo-rapidity is applied to reconstructed tracks. Also the purity of hits used in reconstructed one planar segments is 20% lower than that of two or more planar segment tracks (see figure 6.7(c)). This evidence suggests that for a significant proportion of one planar segment tracks, errors are made during the reconstruction process.

In order to test this hypothesis the geometric position of simulated tracks in the FTD was compared to that of their matched reconstructed tracks. This was performed by selecting primary simulated tracks within the range $1.75 < \eta < 2.75$ and performing the track matching algorithm on a track by track basis, but only using planar hits from SM1. For each track pair the track parameters are extrapolated to the same z coordinate which was chosen to be $z = 210$ cm, the front face of SM1. The difference Δx and Δy between the positions of the simulated and reconstructed track pair in the $x - y$ plane was calculated, along with the radial distance $\Delta r = \sqrt{\Delta x^2 + \Delta y^2}$ between them. Figures 6.12 shows scatter plots of $(\Delta x, \Delta y)$ and distributions of Δr for simulated tracks matched to one planar segment tracks only (a)(c), and tracks with two or more planar segments (b)(d).
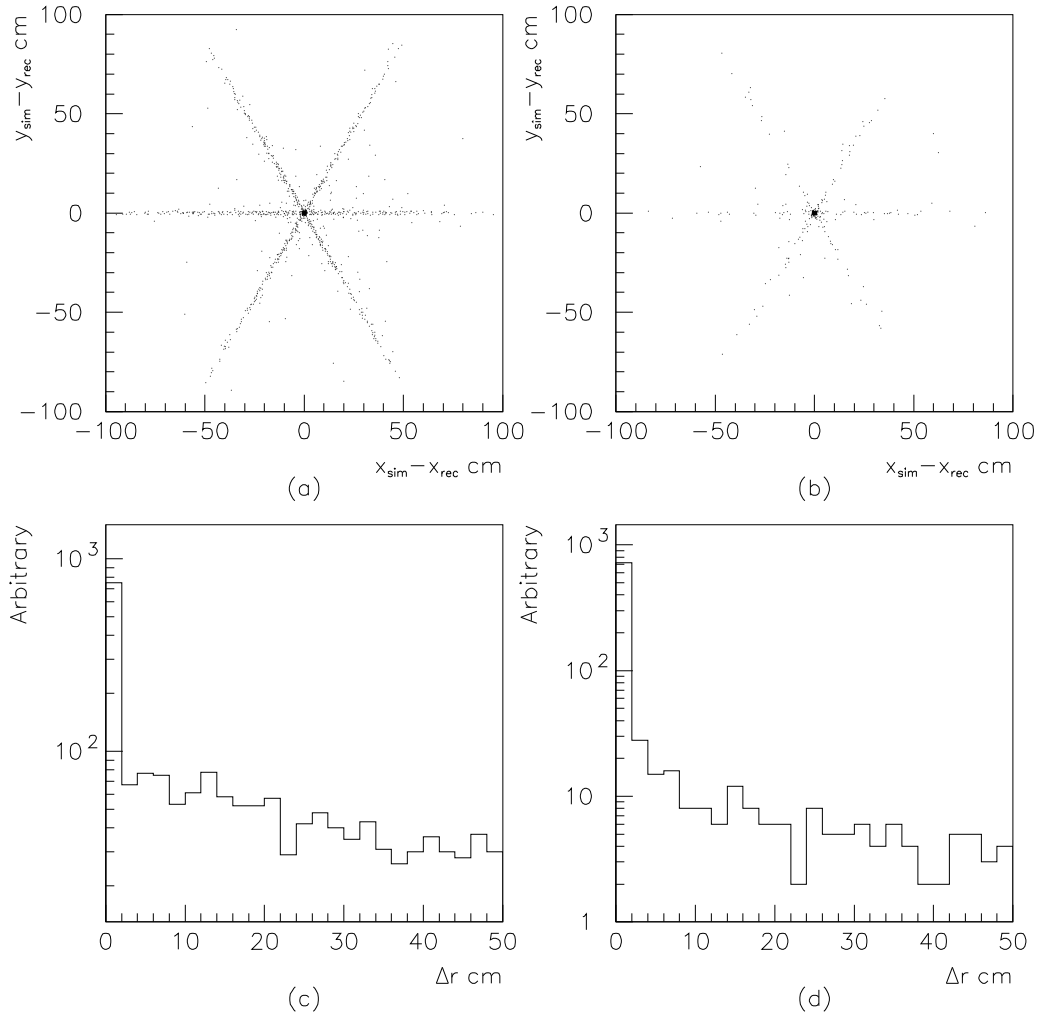
Figure 6.12: Difference between simulated and reconstructed track position for primary tracks and distribution of radial distance Δr in the $x-y$ plane. Figures (a) and (c) only one planar segment tracks, (b) and (d) two or more planar segment tracks.

Figures 6.12(a) and (b) have a very obvious 'star' shape structure which is closely linked to the geometry of the planar layers of FTD. Each of the three lines that the star is constructed from is related to the wire orientation of an XUV chamber. The star shape is caused when a cluster in an XUV orientations is wrongly associated with two others to form incorrect planar segments. The wrongly reconstructed planar segment is positioned at the intersection of the three planes defined by one XUV orientation from each of the tracks. This explains why R_2, the purity of tracks is low (66%) in figure 6.7(c).

To confirm that this is the case, the sample of simulated tracks matched to one planar segment tracks is divided into two groups according to radial distance Δr. Figure 6.13(a) shows distributions of the hit purity R_2 for $\Delta r < 2\,\mathrm{cm}$ and $\Delta r > 2\,\mathrm{cm}$. Tracks which are reconstructed within $2\,\mathrm{cm}$ of their matched simulated track are almost exclusively have a hit purity of $R_2 = 1.0$. Two very small peaks can be seen at $R_2 = 0.33$ and $R_2 = 0.66$ which probably arise from tracks which are closer together than the two track resolution. Tracks with $\Delta r > 2\,\mathrm{cm}$ on the other hand, have their R_2 distribution peaked at around $R_2 = 0.33$, implying that only one cluster of the planar segment actually belongs to the simulated track. Somehow the reconstruction procedure has combined the clusters from three different tracks to form the planar segment. These wrongly reconstructed tracks cannot be distinguished from correctly reconstructed tracks by either a χ^2_{trk} cut or a χ^2_{vtx} cut. It is interesting to note that these wrongly reconstructed tracks still contain valid directional information because they are vertex constrained, albeit poorly.

Points which do not lie on the 'arms' of the star are in fact an artifact of the simulation process. They arise because secondary tracks which are below a certain momentum threshold have their hits flagged as belonging to the parent track. These secondary tracks are sometimes matched, instead of the parent track, thus causing a random offset from the star shape.
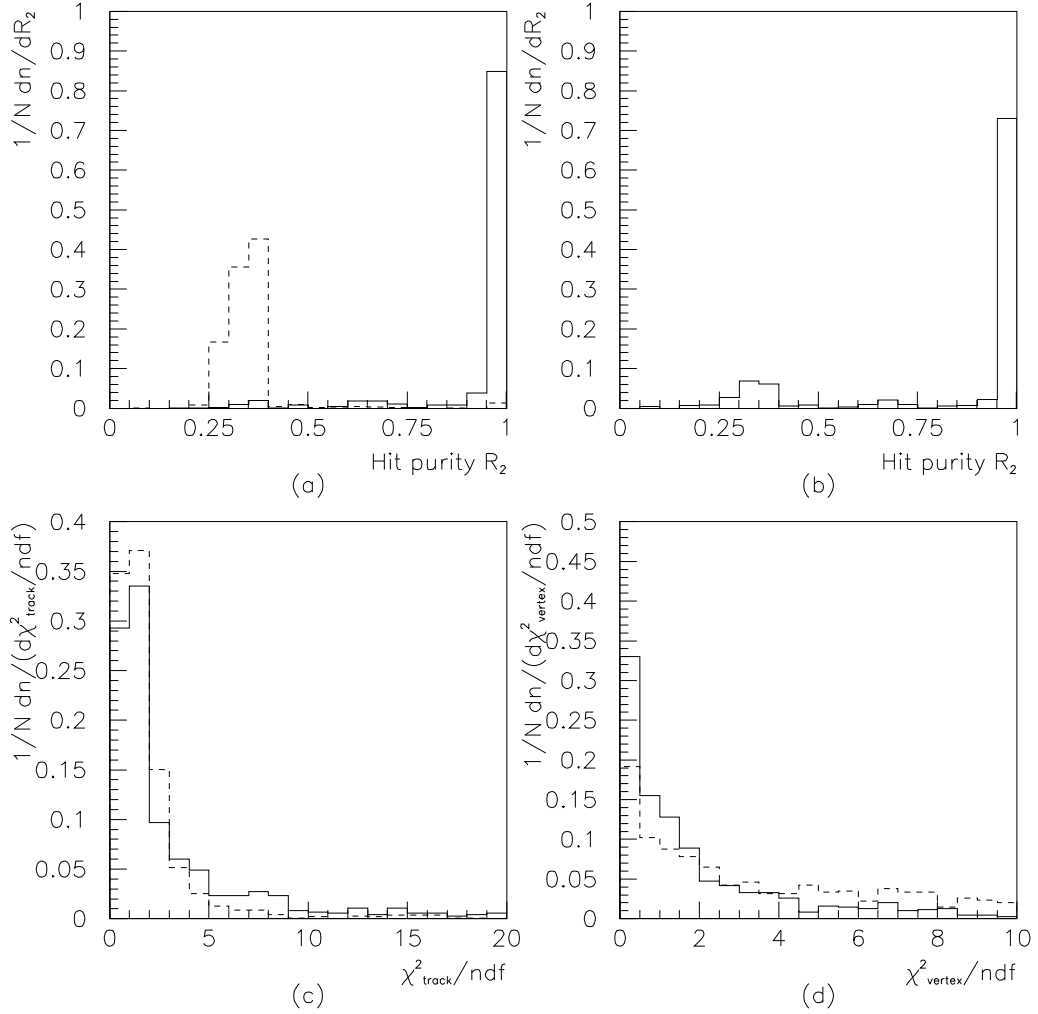
Figure 6.13: Track purity R_2 for (a) one planar segment tracks; solid (dashed) histogram $\Delta r < 2\,\mathrm{cm}$ ($\Delta r > 2\,\mathrm{cm}$) and (b) all two planar segment tracks. (c) χ^2_{trk} distributions for one planar segment tracks. (d) χ^2_{vtx} distributions for one planar segment tracks.

6.5   Summary

The performance of the FTD has been studied in detail for events with high forward multiplicity, and a comparison made between Monte Carlo and data. The simulation of the performance of the FTD is well matched to its performance in data. The linking of track segments shows a strong dependence on the multiplicity of tracks penetrating the FTD, due to the increasing complexity and worsening measurement resolution.

A set of track selection criteria has been developed to select primary tracks and reject secondaries. The track selection gives an efficiency of 41% and purity of 60%. The resolution of selected tracks is shown in figure 6.14, which compare favourably to previous measurements [44] made for lower multiplicity events. For all selected tracks a resolution of $\frac{\sigma_p}{p^2} = 0.060\,(\mathrm{GeV/c})^{-1}$ is achieved. The track selection criteria are listed below:

- At least one planar segment

- $1.75 < \eta < 2.75$

- $\chi^2_{trk}/ndf < 30$

- $\chi^2_{vtx}/ndf < 15$

- $dp/p < 0.3$

The dependence of the FTD's performance with track density has also been studied. The track selection was applied to the subset of tracks located outside of jets (high track density regions) and the efficiency and contamination were calculated to be 41% and 60% respectively. This is consistent with the idea of non-localised track density effects, dependent on the planar chamber geometry.

Evidence showing that a significant number of one planar segment tracks are wrongly reconstructed was shown. These segments are the result of the incorrect
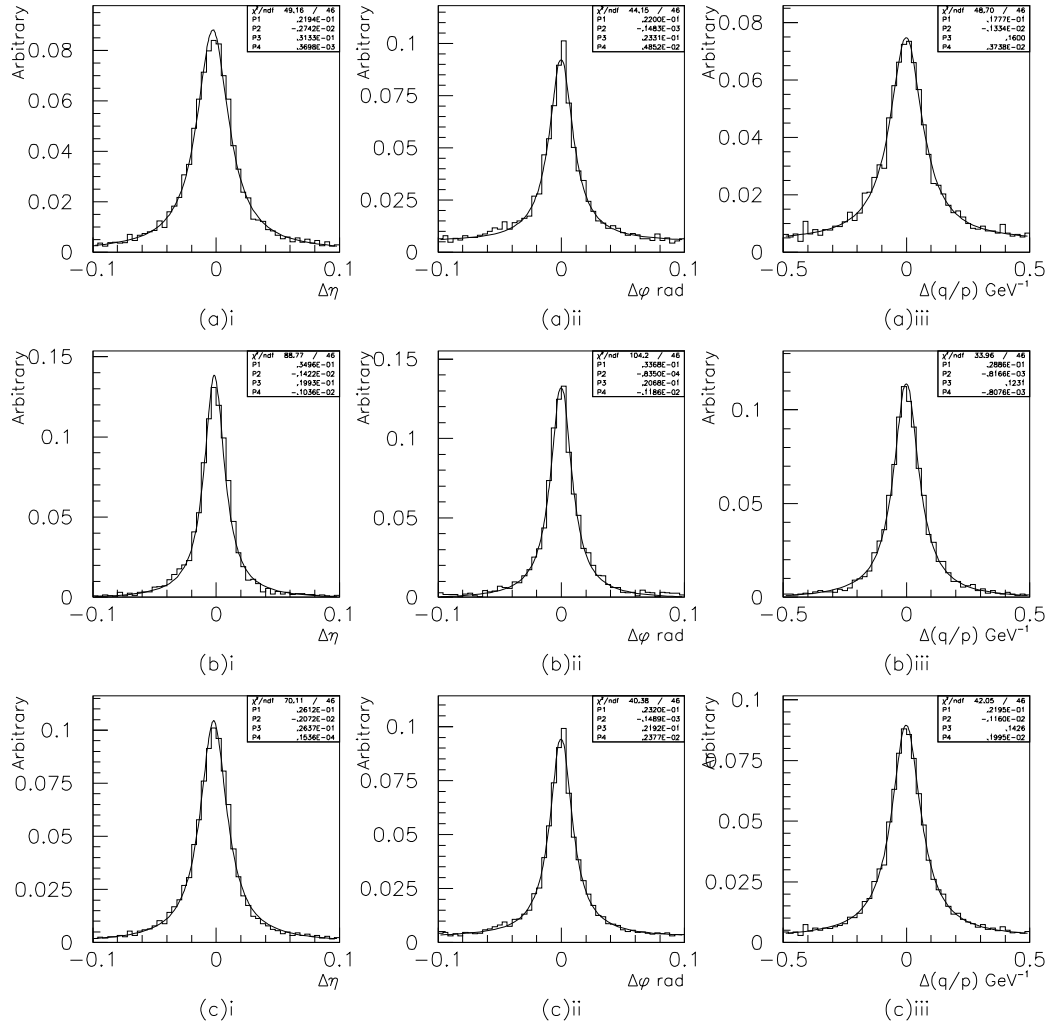
Figure 6.14: The resolution of reconstructed track parameters η, ϕ and q/p of selected tracks. (a) One planar segment tracks only. (b) Tracks with at least two planar segments. (c) All selected tracks. The fit applied is the sum of a Breit-Wigner and a constant with μ=P2 and $\sigma_{FWHM} = 0.425 \times$P3.

association of three clusters from three different tracks, and are mostly indistinguish-
able from correctly reconstructed segments using track parameters.

Chapter 7

Energy Flow

Within hard photoproduction processes, there are four mechanisms which may contribute to transverse energy flow outside of jets, as follows:

I. Initial state radiation. Correlated with hard scattering process.

II. Final state radiation. Correlated with hard scattering process.

III. Energy from the interaction of the spectator partons. This energy is essentially uncorrelated with the hard scattering process.

IV. Energy from the non-interacting spectator partons. This energy is also uncorrelated with the hard scattering process.

With these four mechanisms, fragmentation effects must also be taken into consideration. At HERA, where both resolved and direct photoproduction processes are present, the individual contribution of each of the four processes may to some extent be disentangled. Direct processes only have contributions from (II) final state radiation and (IV) non-interacting spectator partons. Resolved processes on the other hand, may additionally have contributions from the two sources present in direct processes and additional contributions from (I) initial state radiation and

(III) beam remnant interactions. By using generator models both with and without beam remnant interactions (ie PYTHIA MI and PYTHIA SI), it is possible to effectively eliminate the effects of initial state radiation, so that only spectator parton interaction effects remain.

As previously stated, for models incorporating multiple interactions the number of additional beam remnant interactions is expected to be approximately proportional to $(1 - x_\gamma)$, and these additional interactions are expected to translate into additional energy which can be measured in the event. It is therefore logical to choose x_γ as the variable in which to study energy flow. At high values of x_γ, direct events dominate, so it is expected that the energy flow in these events should be reasonably well described by all Monte Carlo models. However, at low values of x_γ resolved processes are dominant, and it is in this region that inadequacies in the Monte Carlo description these processes should be revealed.

To facilitate the study of energy flow in events, each event is divided into four topological regions in $\eta - \phi$ space, in the γp centre of mass frame. These regions are shown in figure 7.1, and are referred to as the central region, the jet cone region, the jet ring region and the photon remnant region. It should be noted that the regions of overlap of jet rings and jet cones are excluded from these regions because the energy deposited in such regions cannot be unambiguously attributed to either region. These regions are chosen to help separate and enhance the measurement of the various components which contribute to energy flow outside of jets. The central region and the jet ring region are particularly sensitive to additional energy flow which is uncorrelated with the primary hard interaction.

7.1 Measurement of LAC Energy Flow

In order to compare measurements in the energy flow in these topological regions it is necessary to take into account their varying areas. Therefore the energy
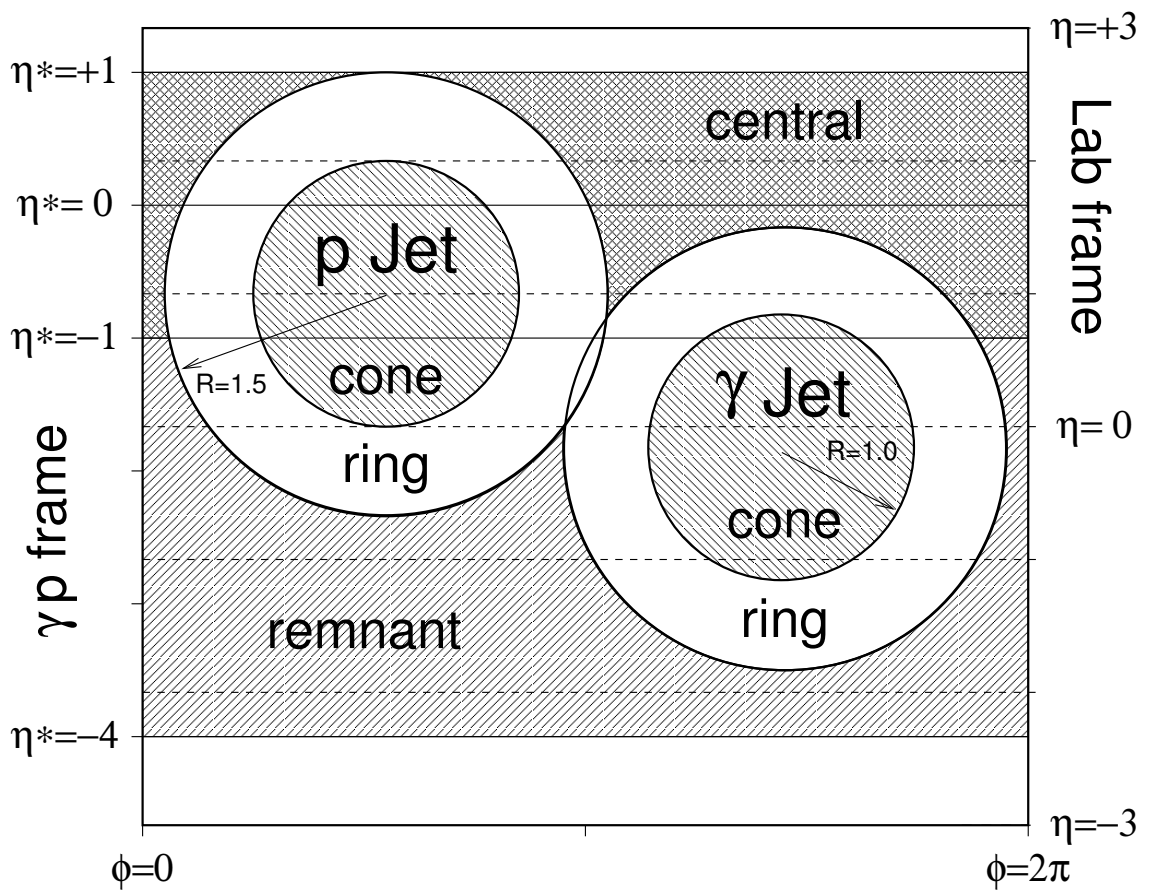
Figure 7.1: Definition of the four topological regions: jet cone, jet ring, central and photon remnant region. Note that the last two are defined in the η^* frame.

measured in each region is normalised to the regions area in $\eta - \phi$ space, to give an energy density. Since the η^* frame is boosted forward by approximately 2.0 units of rapidity from the laboratory frame, in some events it is possible for the central region to extend past $\eta = 3.0$, the limit of acceptance of the LAC. In these cases, the central region is truncated to prevent this happening, and its area recalculated.

7.1.1   LAC Energy Correction

To eliminate detector effects from the measured calorimetric transverse energy, the measured energy is corrected back to the generator (GTR) level. The energy measured in the calorimeter is increased by rescattered particles from the beam pipe and collimators, and varies as a function of η. Although this effect is relatively small, it cannot be ignored when trying to measure the small energies which are detected outside the jet cones. It is known from studies that the calorimeter response to low energy hadrons is well modelled by the LAC simulation [45]. The effect of rescattered particles can be seen in figure 7.2, which shows the ratio of reconstructed to generated transverse energy, for each of the three[1] distinct topological regions as a function of η. The ratio E_t^{rec}/E_t^{gen} for jet cones is almost independent of η because the rescattering effects have been washed out by the large energy densities present in the jet cone region. The other two regions on the other hand show a marked dependence of E_t^{rec}/E_t^{gen} on η, with the general trend being that E_t^{rec}/E_t^{gen} grows with η. This is consistent with the idea that particles at low angle interact with the beam pipe and scatter upwards into the LAC calorimeter.

The correction factors are calculated from all three Monte Carlos, and are found to be in good agreement, indicating that the model dependence of this correction is quite small. A correction function $C(\eta)$ is defined for each of the three

---

[1]The central and photon remnant regions, are only separated by an arbitrary division in η, and for the purposes of calculating the correction factor, may be considered as a single region.
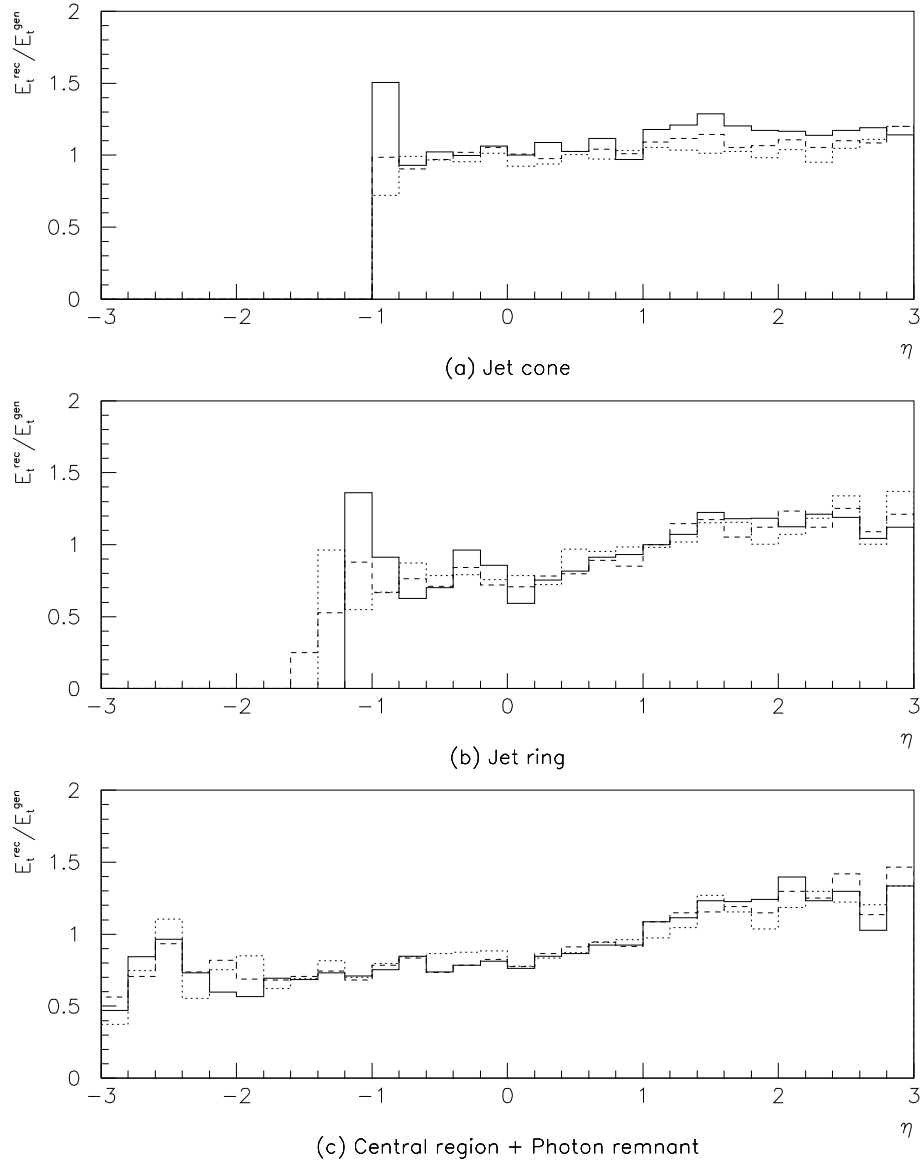
Figure 7.2: The ratio of E_t^{rec}/E_t^{gen} for the three topological regions, for the three Monte Carlos. Solid histogram PHOJET, dashed PYTHIA MI and dotted PYTHIA SI.

regions, based on the ratio E_t^{rec}/E_t^{gen} as

$$C(\eta) = \frac{\sum E_t^{gen}(\eta)}{\sum E_t^{rec}(\eta)} \tag{7.1}$$

which is used to correct the transverse energy of each reconstructed cluster.

7.1.2   Topological Region Area Calculation

Since it is not known for each event whether jets cones and rings will overlap or not, a brute force method of calculating the areas of topological regions is chosen in preference to an algebraic one. For each event, $\eta^* - \phi$ space was divided up into a grid of N_η by N_ϕ, its extent in η^* being determined by LAC acceptance, as previously stated. The non-overlapping areas of the regions are then calculated by counting the number of points N_r that lie in each topological region, and dividing by the total number of points $N_\eta \times N_\phi$ in the grid to give the fraction of the grids total $\eta^* - \phi$ space occupied. Experiment demonstrated that a grid size of spacing $\pi/50$ provided the required level of accuracy, giving less that 1% error on the measurement of jet cone areas.

7.1.3   Sources of Error

The main sources of error for the calculation of LAC energy densities arise from systematics sources, as follows:

- 9% from the model dependence of the correction factor applied to E_t. This is estimated by correcting the data using the correction functions from different Monte Carlos.

- 15% due to migration effects in x_γ^{rec}. Again this is estimated from different Monte Carlos.

- 5% uncertainty in the the knowledge of the hadronic energy scale of LAC calorimeter.

Other systematic effects are negligible in comparison to those listed above. This gives an overall systematic error of $\sim 18\%$.

7.2 FTD Energy Flow

The acceptance of the forward tracker restricts any measurements that can be made to the central topological region. This also imposes the limitation that measurements cannot be made in the η^* frame, causing measurements to be smeared in η. Having accepted these limitations, the charged particle energy flow is measured in the topological region outside of jets in the band $1.75 < \eta < 2.75$, and this measurement is compared to an identical measurement of the inclusive energy flow made in the LAC calorimeter.

7.2.1 Efficiency Correction

Because of the low efficiency for selecting primary tracks (41%) obtained from final track selection (see section 6.5), the measured transverse track momentum is in general not well correlated with the generated charged transverse momentum on an event by event basis. In order to estimate the model dependence of the track selection, the transverse momentum of generated particles is compared to the reconstructed transverse momentum of selected tracks. By averaging the reconstructed transverse track momentum over a number of events, the effects of poor correlation may be removed. Figures 7.3 shows these correlations for the three Monte Carlos, the points having been fitted to a straight line.
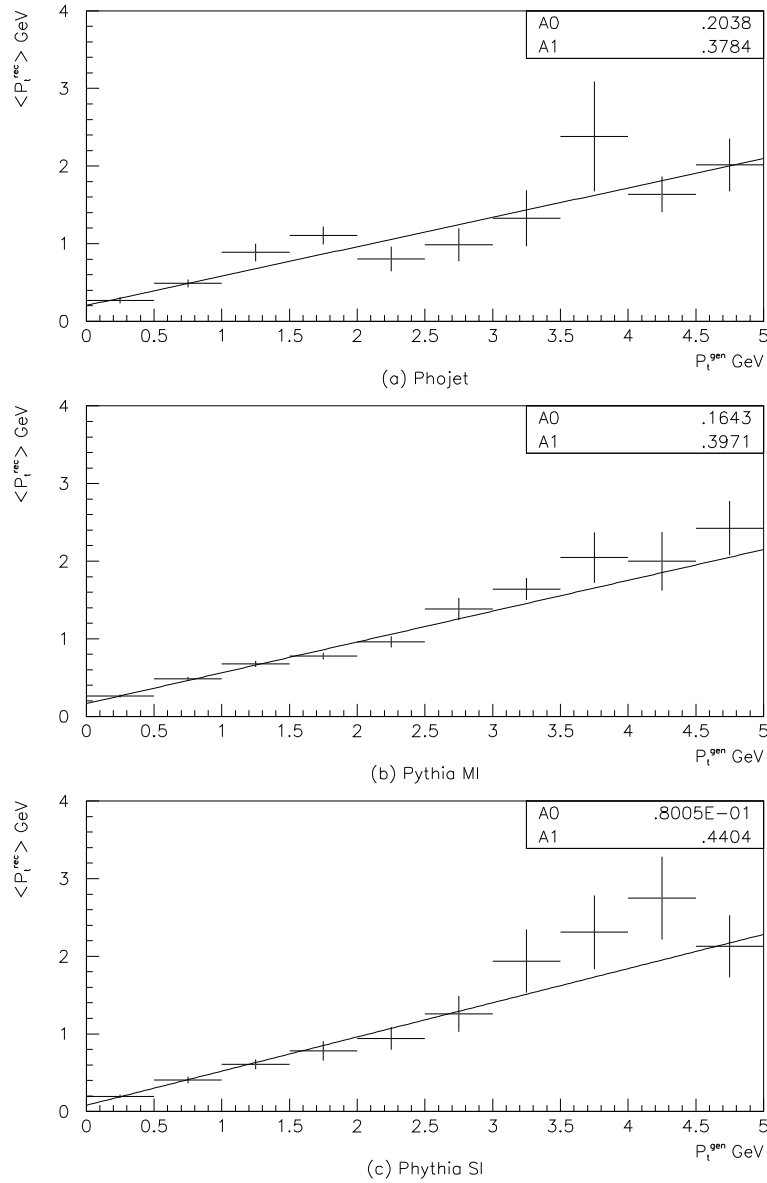
Figure 7.3: The correlation for Monte Carlo between mean p_t^{rec} of selected forward tracks and p_t^{gen} of charged GTR level particles, for the central region between $1.75 < \eta < 2.75$.

The Monte Carlos PHOJET, PYTHIA MI and PYTHIA SI have gradients corresponding to efficiencies of 38%, 40% and 44% respectively, showing only a slight model dependence. These values are also in excellent agreement with the efficiency of the track selection previously calculated from simulated tracks. The y-intercept of the fit gives an estimate of the contamination, and the difference between the three Monte Carlo models is used to estimate the associated systematic error.

As stated in section 6.2.2, the simulated efficiency of supermodule 0 is approximately 10% lower that that observed for data. As a simple correction to the Monte Carlo, all selected tracks containing a SM0 planar segment were weighted by an additional 10%.

7.2.2   FTD Sources of Error

The dominant sources of error for the calculation of the FTD charged particle energy density arise from systematics, as follows:

- 10% from the model dependence of the contamination of selected tracks. Estimated from the from the difference in contamination levels for the three Monte Carlos.

- 15% due to migration effects in x_γ^{rec}. Again this was estimated from different Monte Carlos.

Other systematic effects are negligible in comparison to those listed above. This gives an overall systematic error of $\sim 18\%$.

7.3   Results and Discussion

Presented in figure 7.4 are the corrected mean energy densities as a functions of x_γ^{rec} for the four topological regions. Figure (a) most clearly displays the

differences between the three Monte Carlos and data. At high values of x_γ^{rec} where direct processes dominate, the measured $< E_t >$ for all Monte Carlo models and data agree reasonably well as expected. Moving from high to low x_γ^{rec}, PHOJET and PYTHIA MI exhibit a strong rise in $< E_t >$ from around $0.35\,\mathrm{GeV\,rad^{-1}}$ to $1.0\,\mathrm{GeV\,rad^{-1}}$ and $0.8\,\mathrm{GeV\,rad^{-1}}$ respectively. This rise is also seen in the data, which rises to approximately $0.95\,\mathrm{GeV\,rad^{-1}}$. However, PYTHIA SI only shows a modest rise of $0.2\,\mathrm{GeV\,rad^{-1}}$. The observed rise of energy density for data cannot be explained in terms of increasing QCD radiation. This may be understood by considering the PYTHIA SI model. As previously stated, this model includes both initial and final state radiation effects, but only a $0.2\,\mathrm{GeV\,rad^{-1}}$ rise in energy density is seen, which cannot account for the $0.5\,\mathrm{GeV\,rad^{-1}}$ seen in data. This indicates that an additional component beyond that of QCD radiation is required for a complete description of resolved processes, and the logical choice for the source of this additional energy is beam remnant interactions (multiple interaction).

As previously stated, the signature of models incorporating multiple interaction is the approximate $(1 - x_\gamma)$ dependence of this additional energy. That is to say, the probability of additional interactions is proportional to the energy of the photon remnant. This is exactly what is seen for PHOJET and PYTHIA MI, the two Monte Carlo models incorporating beam remnant interactions. This behaviour is consistent with that observed of the data.

Figures (b), (c) and (d) show the energy densities for the other three regions. As expected figure (c) shows that the energy densities in the jet cone region are compatible, because of the common jet selection criteria. The decrease in energy density with x_γ^{rec} is an artifact of the fact that the momentum of the parton from the photon is proportional to x_γ^{rec}, which is in turn related to the scattered partons momentum. It is interesting to note that in figure (b) all results appear to be compatible with the data.

It is important for any model attempting to describe multiple interactions to not only describe correctly the mean number of interactions, but to describe the
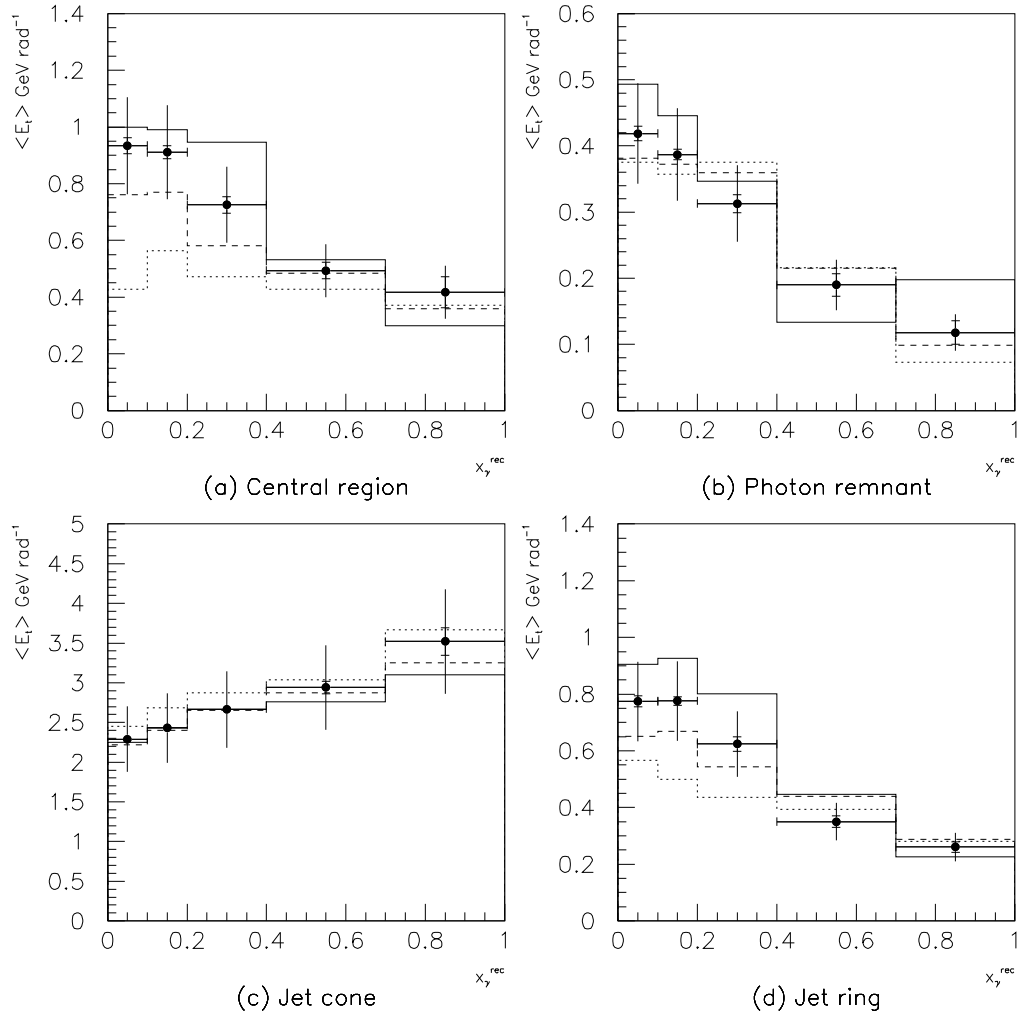
Figure 7.4: Corrected LAC energy density as a function of x_γ^{rec}. Solid histogram PHOJET, dashed PYTHIA MI and dotted PYTHIA SI. Inner error bars are statistical, outer are the quadratic sum of statistical and systematic errors.
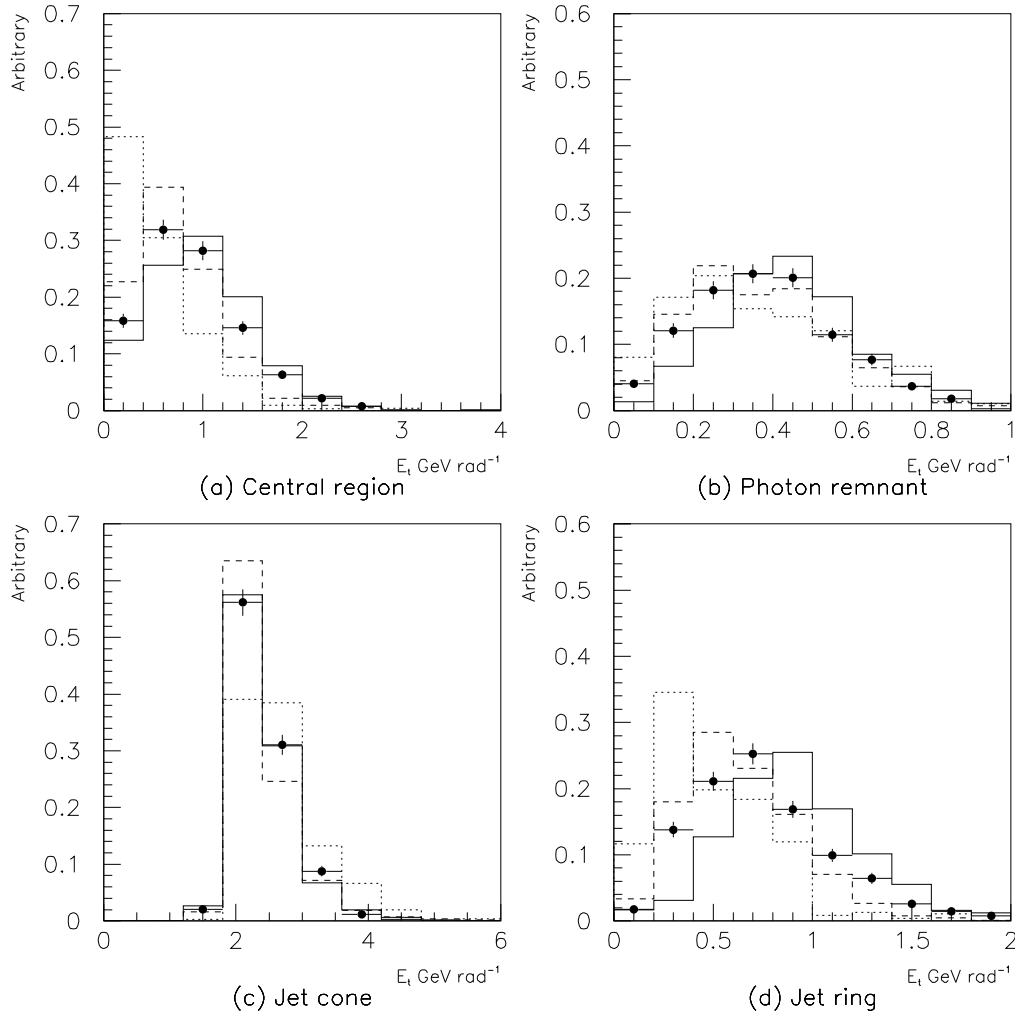
Figure 7.5: Distribution of corrected LAC energy density for $x_\gamma^{rec} < 0.3$. Solid histogram PHOJET, dashed PYTHIA MI and dotted PYTHIA SI. Error bars represent statistical errors only.
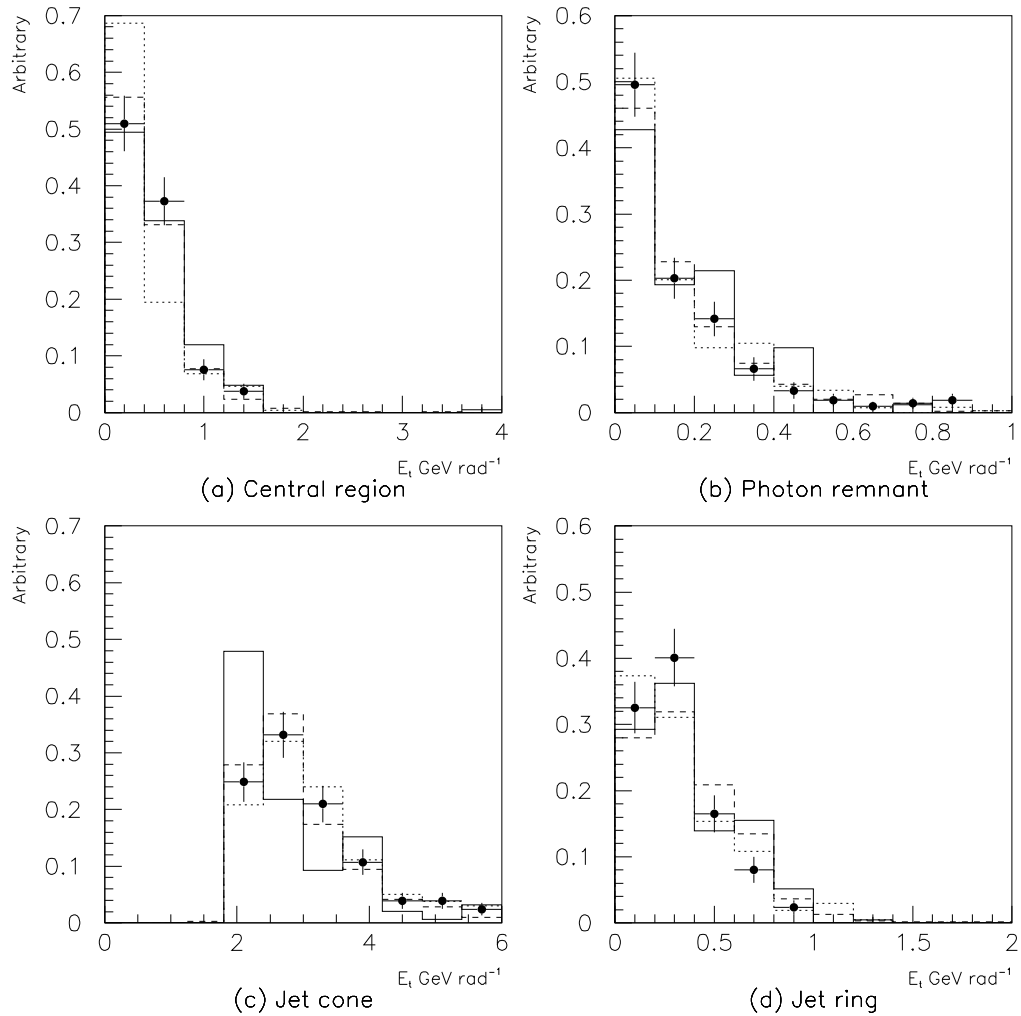
Figure 7.6: Distribution of corrected LAC energy density for $x_\gamma^{rec} > 0.4$. Solid histogram PHOJET, dashed PYTHIA MI and dotted PYTHIA SI. Error bars represent statistical errors only.

event by event fluctuation of the number of multiple interactions. Since the number of multiple interactions cannot be directly measured, the fluctuation of the measured energy densities are examined instead. The event sample is divided into two classes, $x_\gamma^{rec} < 0.3$ and $x_\gamma^{rec} > 0.4$. The former class is dominated by resolved events, while the latter is composed mainly of direct events. Shown in figures 7.5 and 7.6 are the distributions of mean energy densities for these two classes of event. It is expected that the former class of 'resolved' events will show large differences its distributions, and the latter class of 'direct' events, distributions should be compatible. These distributions are shown in figure 7.5 and 7.6. As expected these distributions indicate that for resolved events, PYTHIA SI only poorly describes the data, and that again the data lies somewhere between PHOJET and PYTHIA MI models. For 'direct' events, allowing for low Monte Carlo statistics, reasonable agreement is seen between the three Monte Carlos and the data.

Shown in figure 7.7(a) is the charged particle momentum density as a function of x_γ^{rec}. This may be compared to the energy density measured by the LAC in the same acceptance region which is shown in figure 7.7(b). Good correlation is seen between these two measurements, especially considering the ratio of charged to charged and neutral particles is approximately 0.6. Also shown in figure (c) is the mean track density as a function of x_γ^{rec}. Figures (a) and (c) provide an excellent cross check that the excess of energy that is seen in the LAC measurements does originate from the primary vertex and is not due to rescattered particles or other dirty detector effects.

The event sample is once more divided into 'direct' and 'resolved' classes by virtue of x_γ^{rec}, except this time the mean charged particle momentum density distributions are calculated for each class. These distributions are shown in figure 7.8. Again as expected, the 'direct' sample shows good agreement within errors between Monte Carlo and data. The 'resolved' data sample lies somewhere between PHOJET and PYTHIA MI again.
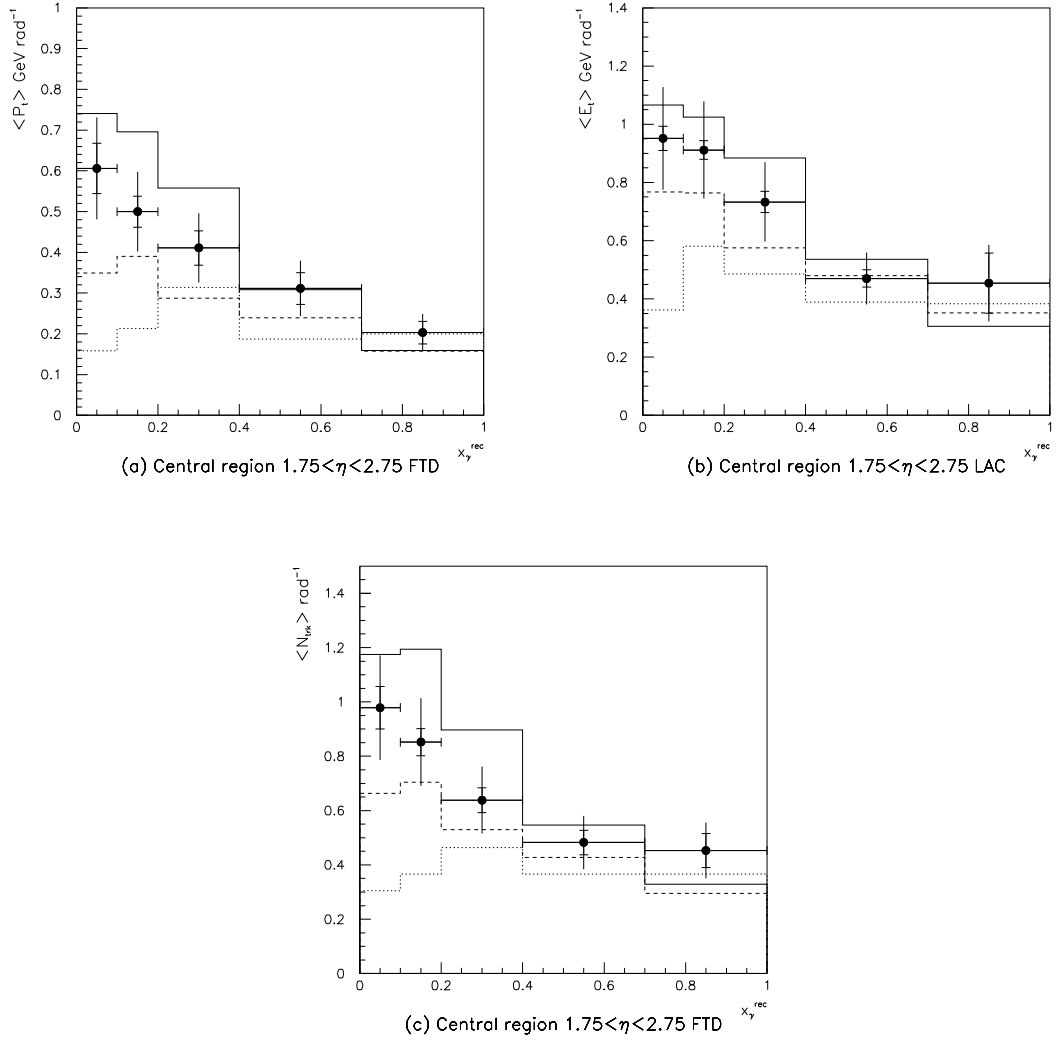
Figure 7.7: (a) Charged particle energy density in the central region for $1.75 < \eta < 2.75$ as measured by the FTD. (b) Calorimetric energy density for corresponding region. Good correlation between the two measurements is seen. (c) Charged track density for same region. Inner error bars are statistical, outer are the quadratic sum of statistical and systematic errors.
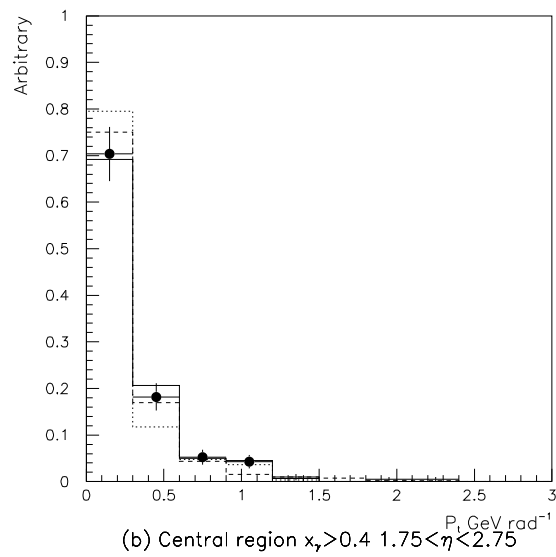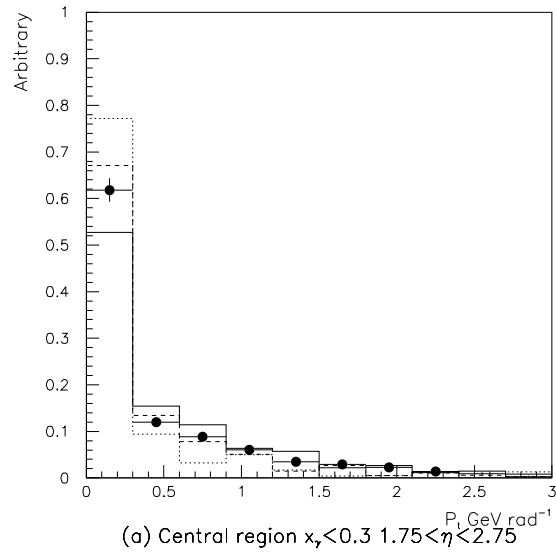
(a) Central region $x_\gamma < 0.3$ $1.75 < \eta < 2.75$

(b) Central region $x_\gamma > 0.4$ $1.75 < \eta < 2.75$

Figure 7.8: The p_t density for (a) $x_\gamma^{rec} < 0.3$ and (b) $x_\gamma^{rec} > 0.4$. Error bars represent statistical errors.

7.4 Monte Carlo Models

In order to understand the effect of the different multiple interaction models and the consequences of their adjustment it is necessary to also consider the other measurable feature of the events, the jet cross sections. The alteration of multiple interaction model parameters is intimately connected with the observed jet rate in a non-trivial way.

Shown in figure 7.9 are the most recent H1 jet cross section measurements, as shown in [39]. Figure (a) shows the inclusive differential jet cross section as a function of reconstructed transverse jet energy, for two different η^{jet} ranges. Figure (b) shows the inclusive differential jet cross section as a function of pseudo-rapidity for different transverse jet energy thresholds.

All of the Monte Carlo models give a reasonable description of the shape of the measured data cross sections. However, the PYTHIA MI model consistently overestimates the cross section for low transverse energy jets. At high transverse jet energies however, PYTHIA MI gives a much better description of the data. As previously stated, PYTHIA MI and PYTHIA SI differ only by additional beam remnant interactions, so a comparison between the calculations of these two generators serves to demonstrate the level of sensitivity to beam remnant interaction. The calculations of the PHOJET generator are in overall best agreement with data. Calculations have shown that NLO models differ from LO by between $10\% - 30\%$ for jet parameters, and $\sim 30\%$ [46, 47] lower cross section, and thus this cannot explain the overestimated cross section of PYTHIA MI.

As previously described, the parameter governing the level of multiple interaction for the PYTHIA MI model is p_t^{cut}, which was set of $1.2\,\mathrm{GeV}$ in this analysis. Since the PYTHIA MI model was found to have too little energy outside of jets, naïvely it might be expected that decreasing this parameter would increase the level of multiple interaction, and so increase the energy flow outside of jets. However, this would have the side effect of further increasing the jet cross sections at low trans-
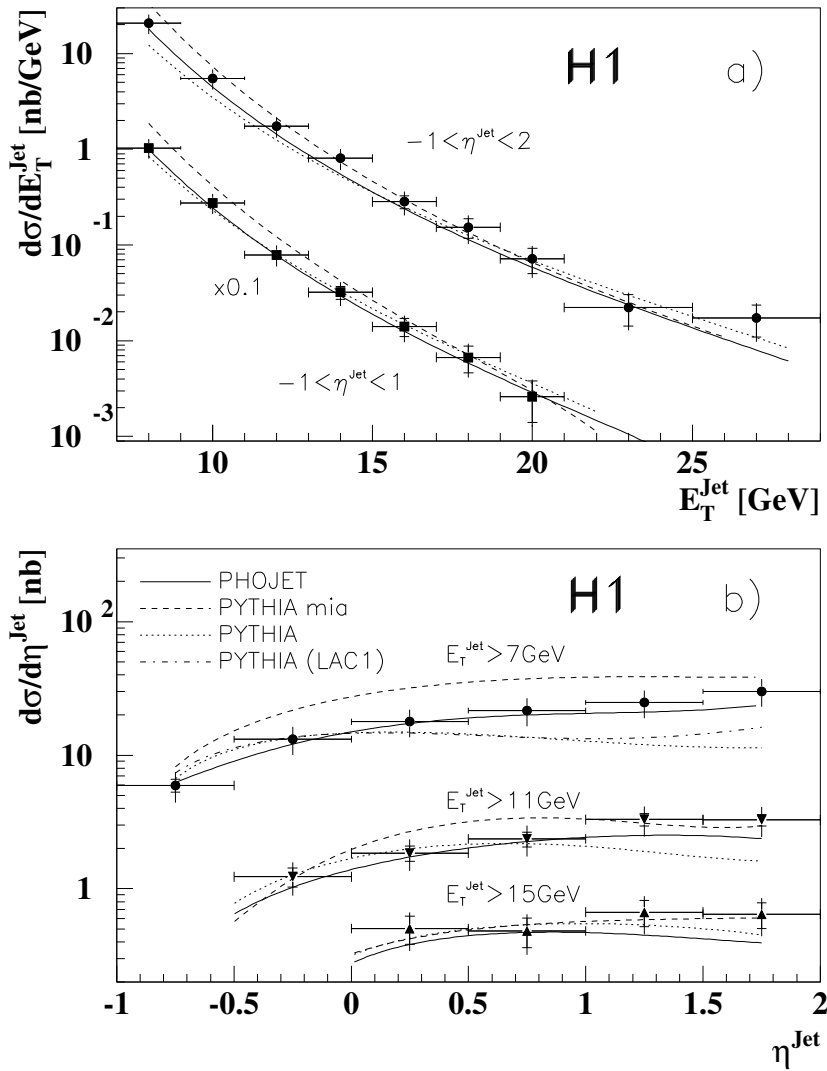
Figure 7.9: Recent H1 jet cross section measurements, also as shown in [39]. (a) Inclusive differential jet cross section for jets with transverse energy above $E_T^{jet} > 7\,\mathrm{GeV}$ summed in a cone of $R = 1$. (b) Differential jet cross section versus pseudorapidity for different thresholds in transverse jet energy.

verse energy. Thus it would appear that this model which uses hard and semi-hard beam remnant interactions cannot easily be adjusted to fit the data.

In contrast, the PHOJET model exhibits an excess of energy outside of jets, but the energy from beam remnant interactions manifests itself in such a way that the jet cross sections are not overestimated. The PHOJET model uses soft and semi-hard interactions to model beam remnant interactions, and thus additional energy is added in a softer, more isotropic fashion. Thus comparison of PHOJET and PYTHIA MI suggests that the beam remnant interactions are better described by soft and semi-hard interactions.

Chapter 8

Conclusion

8.1   The Forward Tracker

The performance of the FTD has been studied in detail for high forward multiplicity hard photoproduction events. The Monte Carlo simulation of the FTD adequately describes the detector's performance, although the Monte Carlo exhibits a slightly reduced efficiency for planar segment reconstruction and linking, which is thought to be an artifact of the Monte Carlo simulation tuning process.

A set of track selection criteria designed to select tracks originating from the primary vertex has been developed. This track selection has an efficiency of 40% and a purity of 60%, and is almost independent of momentum, azimuthal and polar angles. This track selection was subsequently used for the independent measurement of the forward charged particle energy flow.

The track density dependence of the reconstruction performance has been investigated. As expected, in such high multiplicity environments little difference is seen between the efficiency of reconstruction for tracks in areas of high and low track density. This is thought to be due to the non-localising effect of the planar chamber geometry.

The hit composition of one planar segment tracks was analysed, and evidence presented showing that planar segment reconstruction proceeds incorrectly for a significant fraction of these tracks. This is thought in part to be due to the cut used to associate clusters into planar segments. Monte Carlo predicts that a cut of 3 mm should be used, whereas data requires a cut of 7 mm [42]. This difference is due to effects beyond the intrinsic digitisation resolution of the chambers, and it is hoped that with further systematic studies these effects can be reduced and possibly eliminated. It is unfortunate that no z coordinate from charge division is available from the planar chambers, since this could have provided additional information to prevent wrongly reconstructed tracks and improve reconstruction.

During 1993 significant progress was made in understanding the operation and performance of the forward tracker. The reconstruction code for the 1994 run period has been significantly modified and improved. Analysis using 1994 data should yield a more accurate measurement of charged particle energy flow in the forward direction.

8.2 Energy Flow and Multiple Interaction

Detailed measurement of the energy flow of hard photoproduction events has been made using the liquid argon calorimeter, and for the first time independently using the forward tracker. It has been shown that resolved photoproduction events in data exhibit an excess of energy which cannot be explained by QCD calculations made using only LO matrix elements and parton showers (PYTHIA SI). However, Monte Carlo models including beam remnant interactions (PHOJET and PYTHIA MI) have been shown to provide a better, but not perfect, description of the data. This provides strong evidence for the existence of multiple interactions.

The charged particle energy flow outside of jets has been measured using a track selection optimised to select tracks originating from the primary vertex. The

	$< E_t > \mathrm{GeV\,rad^{-1}}$ LAC	$< p_t > \mathrm{GeV\,rad^{-1}}$ FTD
PHOJET	1.02	0.70
Data	0.90	0.52
PYTHIA MI	0.73	0.36
PYTHIA SI	0.51	0.27

Table 8.1: The mean energy density of events with $x_\gamma^{rec} < 0.3$ measured in the central topological region for $1.75 < \eta < 2.75$.

model dependence of this track selections efficiency was found to be small ($\sim 4\%$), whereas the model dependence of contamination ($\sim 10\%$) was found to be the dominant contribution to the systematic uncertainty.

The charged particle energy flow outside of jets in the region $1.75 < \eta < 2.75$ was found to exhibit the same rise which has been seen in LAC calorimetric measurements. This trend was also seen in the observed track density. Table 8.1 summarises the mean energy density measured by both the LAC and the FTD in the central region $1.75 < \eta < 2.75$ and $x_\gamma^{rec} < 0.3$.

When the energy flow outside of jets and the measured jet cross sections of data and the Monte Carlos are examined, the PHOJET generator is found to give the most consistent description of the observed data. The PYTHIA MI model does not seem to be able to describe both the jet cross section and the underlying event energy simultaneously. This suggests that the PHOJET model's beam remnant interaction via soft and semi-hard interaction is favoured in preference to the semi-hard and hard interactions of PYTHIA MI model.

References

[1] C. Weizsäcker, Z. Phys. **88** (1934) 612.

[2] E. Williams, Phys. Rev. **45** (1934) 729.

[3] A. Bawa and W. Stirling, J. Phys. **G15** (1989) 1339.

[4] G. Schuler and T. Sjöstrand, *Towards a Complete Description of High Energy Photoproduction*, Technical Report CERN-TH.6796/93, CERN, Geneva, (1993).

[5] M. Drees and R. Godbole, *Resolved Photon Processes*, MADPH 95-898, University of Wisconsin, USA, (1995).

[6] J. Sakurai, Ann. Phys. **11** (1960) 1.

[7] M. Gell-Mann and F. Zachariasen, Phys. Rev. **124** (1961) 953.

[8] Y. Nambu and J. Sakurai, Phys. Rev. Lett. **8** (1962) 79.

[9] M. Greco, Nucl. Phys. **63B** (1973) 398.

[10] H1 Collaboration, Phys. Lett. **B297** (1992) 205–213.

[11] H1 Collaboration, Nucl. Phys. **B445** (1995) 195–218.

[12] M. Gluck, E. Reya, and A. Vogt, Phys. Rev. **D46** (1992) 1973.

[13] H1 Collaboration, Phys. Lett. **B314** (1993) 436–444.

[14] ZEUS Collaboration, Phys. Lett. **B342** (1995) 417–432.

[15] T. Sjöstrand and M. van Zijl, Phys. Rev. **D36** (1987) 2019.

[16] M. Gluck, E. Reya, and A. Vogt, Z. Phys. **C53** (1992) 127.

[17] T. Sjöstrand, *PYTHIA 5.7 and JETSET 7.4; Physics and Manual*, Technical Report 7112/93, CERN, Geneva, (1993).

[18] I. Abt. *Manual to IJRAY, a Monte Carlo Generator Shell to Produce ep Events for H1.* DESY, Hamburg, 05/93/290 edition, (1993).

[19] R. Engel and A. Rostovtsev, *PHOJET - A Monte Carlo Event Generator for Photoproduction*, H1 Note H1-01/95-420, DESY, Hamburg, (1995).

[20] A. Capella et al., Phys. Rep. **236** (1994) 227.

[21] R. Engel, Z. Phys. **C66** (1995) 203–214.

[22] B. Wiik, *HERA Status*, In W. Buchmüller and G. Ingelman, editors, *Proceedings of the HERA Workshop*, volume 1, page 1, Hamburg, October (1991). H1 Collaboration.

[23] H1 Calorimeter Group, Nucl. Inst. and Meth. **A336** (1993) 460.

[24] H1 Calorimeter Group, Nucl. Inst. and Meth. **A350** (1994) 57.

[25] H1 Calorimeter Group, Nucl. Inst. and Meth. **A336** (1993) 499.

[26] H1 Collaboration, *The H1 Detector at HERA*, DESY Preprint DESY-93-103, DESY, Hamburg, (1993). Submitted to Nucl. Inst. and Meth.

[27] G. Beck et al., $e^{\pm}$ *Identification Using the Drift Chambers and Transition Radiators of the H1 Forward Track Detector*, In *The Vienna Wire Chamber Conference*, (1995).

[28] W. Haynes, *Experiences at HERA with the H1 Data Acquisition System*, H1 Note DESY-92-129, DESY, Hamburg, (1992).

[29] S. Eichenberger et al., *A Fast Pipelined Trigger for the H1 Experiment*, In *Proceedings of the International Conference on Computing in High Energy Physics*, page 214, Geneva, September (1992).

[30] H1 Collaboration, *H1REC - The Official H1 Reconstruction Program*, H1 Internal Software, DESY, Hamburg, (1991).

[31] J. Meyer, *Guide to Simulation Program H1SIM*, H1 Internal Document, DESY, Hamburg, (1991).

[32] S. Giani, *GEANT Detector Description and Simulation Tool*, In *CERN Program Library Long Writeup W5013*, Geneva, March (1994).

[33] L. Criegee, *MDB - The H1 Database Program*, H1 Internal Document, DESY, Hamburg, (1995).

[34] U. Bassler et al., *Run Selection for the H1 1993 F_2 Analysis*, H1 Note H1-02/95-428, DESY, Hamburg, (1995).

[35] J. Riedlberger, *The H1 Trigger with Emphasis on Tracking Triggers*, H1 Note H1-01/95-419, DESY, Hamburg, (1995).

[36] J. Kurtzhöfer, *The QJCONE Jet Algorithm and its Implementation in H1PHAN*, H1 Note H1-09/94-375, DESY, Hamburg, (1994).

[37] H. Albrecht et al., *A Guide to H1PHAN*, H1 Internal Document, DESY, Hamburg, (1995).

[38] J. Huth et al., In *FERMILAB-CONF-90/249-E*, (1990).

[39] H1 Collaboration, *Jets and Energy Flow in γp Collisions at HERA*, DESY Preprint DESY-95-219, DESY, Hamburg, (1995).

[40] A. Rostovtsev, *Test of Multiple Interaction Model in Photoproduction*, H1 Note H1-05/94-358, DESY, Hamburg, (1994).

[41] R. Prosi et al., *Transverse Energy Cross Section in Photoproduction at HERA*, H1 Note H1-05/94-356, DESY, Hamburg, (1994).

[42] S. Burke et al., *Track Finding and Fitting in the H1 Forward Tracking Detector*, H1 Note H1-03/95-434, DESY, Hamburg, (1995).

[43] S. Burke, *Private Communication.*

[44] H. Lohmander, *Selecting Forward Tracks in the H1 Detector*, H1 Note H1-03/94-347, DESY, Hamburg, (1994).

[45] P. Loch, *Response of the H1 Liquid Argon Calorimeter to Low Energy Hadrons*, H1 Note H1-01/95-424, H1, Hamburg, (1995).

[46] L. Gordon and J. Storrow, Phys. Lett. **B291** (1994) 320.

[47] G. Krammer and S. Salesch, Z. Phys. **C61** (1994) 277.

Acknowledgements

Thanks to the following people back home who have helped me escape the rigours of academia: Rob Abernethy, Jason Browne, Robin Compton, Steve Crook, Nick Holton, Jamie Martin, Tom Lowery, Rich 'Parky' Parkins, Rob Sinkinson, Ben Stephenson, Sean Titley and John Watkins (again). Finally a quick mention to Chris and Pattie Browne for providing shelter and alcohol after the pubs shut.

Well, that just about wraps it up for now.

<div style="text-align: right">

Mark

January 1996

</div>